Calculation of Viscous Effects on Transonic Flow for Oscillating Airfoils and Comparisons With Experiment

James T. Howlett
and Samuel R. Bland

NASA

Calculation of Viscous Effects on Transonic Flow for Oscillating Airfoils and Comparisons With Experiment

James T. Howlett
and Samuel R. Bland

Langley Research Center
Hampton, Virginia

Calculation of Viscous Effects on Transonic Flow for Oscillating Airfoils and Comparisons With Experiment

James T. Howlett
and Samuel R. Bland

Langley Research Center
Hampton, Virginia

Summary

A method is described for calculating unsteady transonic flow with viscous interaction by coupling a steady, integral boundary-layer code with an unsteady, transonic, inviscid small-disturbance computer code in a quasi-steady fashion. Explicit coupling of the equations together with viscous-inviscid iterations at each time step yield converged solutions with computer times about double those required to obtain inviscid solutions. The accuracy and range of applicability of the method are investigated by applying it to four AGARD standard airfoils. The first-harmonic components of both the unsteady pressure distributions and the lift and moment coefficients have been calculated. Comparisons with inviscid calculations and experimental data are presented. These comparisons show that the viscous boundary layer can have a large effect on unsteady pressures even though steady-flow effects are small. The results demonstrate that accurate solutions for transonic flows with viscous effects can be obtained for flows involving moderate-strength shock waves.

Introduction

Unsteady transonic flow fields are routinely calculated with computer codes using finite-difference methods. Many of these computer codes are based upon transonic small-disturbance theory (ref. 1) and are quite accurate, within the limits of this theory, if viscous effects are small (ref. 2). For example, Bland and Seidel (ref. 3) present extensive inviscid calculations for several of the unsteady transonic test cases recommended by the AGARD Structures and Materials Panel (ref. 4) and show excellent agreement between inviscid calculations and experiments for subcritical conditions. However, the agreement deteriorates as free-stream Mach number is increased and embedded shocks develop and move aft. For transonic flows with moderate or strong shocks, the inclusion of viscous effects is essential for accurate predictions of aerodynamic loading (ref. 5).

Although Navier-Stokes computer codes are available for viscous calculations (refs. 6 and 7), their cost is prohibitive for routine use. As a result, much effort has been directed toward coupling viscous boundary-layer models with inviscid analyses (ref. 8). As commonly implemented, the inviscid outer flow solution provides the pressure distribution that is needed to solve the boundary-layer equations for the boundary-layer displacement-thickness distribution. This boundary-layer displacement thickness is used to modify the airfoil surface boundary condition for the next outer flow inviscid solution. This iterative process is then repeated until the airfoil surface pressures converge.

For steady transonic flows over airfoils and wings at moderate angles of attack, this iterative solution technique yields solutions that show good agreement with experiments (refs. 5 and 9). For unsteady flow problems, adequate techniques for viscous-inviscid interactive calculations are still under development (refs. 10 and 11).

Quasi-steady coupling between the integral lag-entrainment, steady boundary-layer model of Green (ref. 12) and the LTRAN2 unsteady transonic code (ref. 1) has been reported by Rizzetta (ref. 13). The resulting computer code was applied by Guruswamy and Goorjian (ref. 14) in a study of the effects of viscosity on unsteady transonic airloads. Up to 8 000 time steps per cycle of oscillation were required to obtain reasonably accurate answers. For step sizes even smaller than this the computer code became unstable. In a similar investigation using a different transonic small-disturbance computer code, Houwink (ref. 15) obtained satisfactory solutions with 120 time steps per cycle.

In reference 16, preliminary results from the present study were reported in which Rizzetta's boundary-layer method was incorporated into the unsteady, transonic, small-disturbance computer code XTRAN2L (ref. 17). Several improvements to the procedure of Rizzetta were described, the most important being a change of the viscous-inviscid coupling procedure and the inclusion of viscous-inviscid iterations at each time step in order to obtain converged solutions. In addition, the semiempirical viscous wedge was eliminated and the boundary-layer equations were numerically integrated from a specified transition point to the downstream computational boundary.

In the present paper, all modifications included in the viscous code of reference 16 are described along with the most recent improvements. The accuracy and range of applicability of the code are investigated by applying it to four of the airfoils recommended for transonic test cases by the AGARD Structures and Materials Panel (ref. 4): NACA 64A006, NACA 64A010A, MBB-A3, and NACA 0012. The results include the calculated first-harmonic components of the unsteady pressure distributions and the calculated lift and moment coefficients. Comparisons with the inviscid calculations of Bland and Seidel (ref. 3) and experimental data (ref. 18) are presented. These results extend the comparisons of reference 3 to include viscous effects and demonstrate the improvements obtained in predicting shock location and strength.

1

Symbols

C_E	entrainment coefficient
C_p	pressure coefficient
C_p^*	critical pressure coefficient
$\tilde{C}_p$	normalized unsteady pressure coefficient; first harmonic of C_p divided by oscillation amplitude
$\Delta\tilde{C}_p$	normalized unsteady lifting pressure coefficient
c	airfoil chord, m
c_{h_β}	first-harmonic hinge-moment coefficient due to flap rotation, per radian
c_l	steady lift coefficient
c_{l_α}	first-harmonic lift coefficient due to pitch, per radian
c_{l_h}	first-harmonic lift coefficient due to plunge, per h/c
c_{l_β}	first-harmonic lift coefficient due to flap rotation, per radian
c_m	steady pitching-moment coefficient
c_{m_h}	first-harmonic pitching-moment coefficient due to plunge, per h/c
c_{m_α}	first-harmonic pitching-moment coefficient due to pitch, per radian
c_{m_β}	first-harmonic pitching-moment coefficient due to flap rotation, per radian
F	airfoil surface function
f	oscillation frequency, Hz
$f_1, ..., f_6$	functions in boundary-layer equations defined by equations (A1) to (A3)
$H, \overline{H}$	boundary-layer shape factors
h	plunge displacement in y-direction, m
h_o	dynamic plunge amplitude, m
k	reduced frequency, $\omega c/2U$
M	free-stream Mach number
N_{Pr}	Prandtl number
N_{Re}	Reynolds number, Uc/v
N_{Su}	Sutherland number
t	nondimensional time, $\omega\bar{t}$

$\bar{t}$	time, sec
U	free-stream velocity, m/sec
x	normalized streamwise coordinate relative to leading edge, positive downstream
x_α	pitch-axis location relative to leading edge
x_β	flap-axis location relative to leading edge
y	normalized coordinate normal to free stream, positive up
α	angle of attack, deg
α_m	mean angle of attack, deg
α_o	dynamic pitch angle, deg
β	flap angle, deg
β_m	mean flap angle, deg
β_o	dynamic flap angle, deg
γ	ratio of specific heats
γ^*	$= 2 - (2 - \gamma)M^2$
$\Delta(...)$	indicates jump in ...
δ^*	boundary-layer displacement thickness, m
ε	airfoil thickness ratio
θ	boundary-layer momentum thickness, m
ξ	streamwise physical coordinate
v	kinematic viscosity, m^2/sec
ϕ	inviscid-disturbance velocity potential
ω	angular frequency, $2\pi f$, rad/sec

Subscript:

i	index of grid points in x-direction

Superscript:

n	nth time step

All angles are positive for trailing edge down. Moments are positive for leading edge up. Pitching moments are taken about the quarter-chord in all cases. In all cases, hinge moments are taken about the hinge axis located at the three-quarter chord.

Analysis

The inviscid code used in this study is the XTRAN2L computer code developed at the NASA

Langley Research Center by Whitlow (ref. 17). This code is an extensively modified version of the LTRAN2-NLR code developed by Houwink and Van der Vooren (ref. 19), which is, in turn, an improved version of the LTRAN2 code of Ballhaus and Goorjian (ref. 1). Additional details on the XTRAN2L code may be found in the User's Manual (ref. 20).

Inviscid Analysis

The XTRAN2L code is used to solve the complete two-dimensional transonic small-disturbance (TSD) equation

$$\frac{4k^2M^2}{\varepsilon^{2/3}}\phi_{tt} + \frac{4kM^2}{\varepsilon^{2/3}}\phi_{xt} = [(1-M^2)/\varepsilon^{2/3} - M^2(\gamma^*+1)\phi_x]\,\phi_{xx} + \phi_{yy} \quad (1)$$

The disturbance velocity potential ϕ is normalized by $c\varepsilon^{2/3}$, where c is the airfoil chord and ε is the airfoil thickness ratio. The spatial coordinates x and y and the time t are normalized by c, $c/\varepsilon^{1/3}$, and ω^{-1}, respectively, where ω is the frequency of unsteady motion. The reduced frequency (based on the semichord) is $k = \omega c/2U$, where U is the free-stream velocity. The free-stream Mach number is M and $\gamma^* = 2 - (2-\gamma)M^2$, where γ is the ratio of specific heats.

The boundary conditions on the airfoil and wake are

$$\phi_y^\pm = F_x^\pm + F_t^\pm \qquad (0 \le x \le 1;\ y = 0^\pm)\ (2)$$

$$\Delta\phi_y = 0 \qquad (1 < x;\ y = 0^\pm)\ (3)$$

$$\Delta(\phi_x + \phi_t) = 0 \qquad (1 \le x;\ y = 0^\pm)\ (4)$$

where the superscript $\pm$ refers to the airfoil upper or lower surface, the function $F(x,t)$ denotes the airfoil surface, and $\Delta(...)$ indicates a jump in the bracketed quantity across the wake. In the far field, nonreflecting boundary conditions are used on the outer edges of the computational domain. The nonreflecting boundary condition for the upstream boundary is (see ref. 17 by Whitlow)

$$\frac{1}{2}\left(\frac{A}{B} + \frac{D}{B^{1/2}}\right)\phi_t - \phi_x = 0$$

For the downstream boundary, the condition is

$$\frac{1}{2}\left(\frac{-A}{B} + \frac{D}{B^{1/2}}\right)\phi_t + \phi_x = 0$$

At the top of the computational domain,

$$\frac{BD}{A}\phi_x + \phi_y = 0$$

At the bottom of the computational domain,

$$\frac{BD}{A}\phi_x - \phi_y = 0$$

In these equations, the coefficients are defined by

$$A = 4kM^2/\varepsilon^{2/3}$$
$$B = (1-M^2)\varepsilon^{2/3} - M^2(\gamma^*+1)\phi_x$$
$$C = 4k^2M^2/\varepsilon^{2/3}$$
$$D = \left(4C + \frac{A^2}{B}\right)^{1/2}$$

An alternating-direction implicit (ADI) solution algorithm is used to obtain numerical results. Complete details are given by Whitlow in reference 17. The numerical results are obtained on an 80 × 61 computational grid in x-y space. Details of the grid are presented in reference 21. This grid extends $\pm 20c$ in x, $\pm 25c$ in y, and has 51 grid points on the airfoil. Converged steady inviscid solutions are obtained and used as starting solutions for steady viscous analyses. The unsteady solutions are initiated from the respective inviscid or viscous steady solutions.

Viscous Analysis

The effect of a viscous boundary layer for attached turbulent flow is modeled in a quasi-steady manner by means of Green's lag-entrainment equations (ref. 12) as implemented by Rizzetta (ref. 13). This integral method evaluates the boundary-layer parameters by the following equations (see appendix A for details):

$$\left(\frac{\theta}{c}\right)_x = f_1 + f_2\phi_{xx}$$

$$\frac{\theta}{c}\,\overline{H}_x = f_3 + f_4\phi_{xx}$$

$$\frac{\theta}{c}\,(C_E)_x = f_5 + f_6\phi_{xx}$$

The coefficients f_1 to f_6 are functions of θ, $\overline{H}$, C_E, and other parameters given in detail in appendix A. The function ϕ_{xx} is calculated from the inviscid-disturbance velocity potential ϕ as explained in the following section. The boundary-layer displacement thickness δ^* is computed by

$$\delta^* = \theta \cdot H(\overline{H})$$

3

The equation relating the two shape factors H and $\overline{H}$ is given in appendix A.

Downstream of the trailing edge, the same equations are applied to each side of the wake surface independently with the skin friction set to zero and the dissipation length scale doubled as in reference 12 to account for the observed far field behavior of wakes.

Coupling between the boundary layer and inviscid analyses is through the boundary conditions on the airfoil and wake. The boundary conditions given by equations (2) and (3) are modified, respectively, as follows (see ref. 11 by Houwink and Veldman and ref. 13 by Rizzetta):

$$\phi_y^\pm = F_x^\pm + F_t^\pm + \left(\frac{\delta^*}{\varepsilon c}\right)_x^\pm \qquad (0 \le x \le 1;\ y = 0^\pm) \quad (5)$$

$$\Delta \phi_y = \Delta \left(\frac{\delta^*}{\varepsilon c}\right)_x \qquad (1 < x;\ y = 0^\pm) \quad (6)$$

Equation (5) is a direct extension of the airfoil boundary condition as given by Rizzetta (ref. 13) to include the term $F_t^\pm$ that has been added to account for the time dependence of the airfoil motion in the boundary conditions.

Viscous-Inviscid Coupling

A key feature of any viscous-inviscid interaction method is the precise manner in which the boundary-layer calculations are coupled with the inviscid code. Several significant modifications to the procedures used by Rizzetta (ref. 13) have been incorporated into the present method, and these modifications are described in the following paragraphs.

1. In the analysis of Rizzetta (ref. 13), the coupling between the inviscid code and the boundary-layer calculations is done in an implicit manner. In the present code, this coupling, for calculations on the airfoil, is made explicit in a form similar to that of Houwink (ref. 15). Implicit coupling is retained along the wake. The explicit coupling between boundary layer and inviscid solution on the airfoil is implemented by the direct use of equation (5) in the expression for the airfoil downwash. That is, at time level $t = t^{n+1}$, the last term on the right side of equation (5) is evaluated by using values at the previous time step $t = t^n$ as follows:

$$\left(\frac{\delta_i^{*n+1}}{\varepsilon c}\right)_x \approx \frac{1}{\varepsilon c} \frac{\delta_{i+1}^{*n} - \delta_{i-1}^{*n}}{x_{i+1} - x_{i-1}} \qquad (x_i \le 1) \quad (7)$$

Although this procedure does involve a lag of the boundary-layer displacement thickness by one time step, it has been shown in reference 16 to be of comparable accuracy to the implicit procedure and,

in addition, it allows a substantial increase in the size of the time step used in the numerical integration of the flow equations.

2. The calculation of ϕ_{xx} for input to the boundary-layer equations has been modified. In the original method of Rizzetta, type-dependent differencing was used to calculate ϕ_{xx}. This differencing was included in the code described in reference 16. Type-dependent differencing is normally used in modern computational fluid dynamics to account properly for the domain of dependence in solving partial differential equations by the finite-difference method and not for calculating the derivatives of known functions as is required in the present application.

In reference 16, use of type-dependent differencing resulted, for some applications, in spurious amplitude effects due to a jump in the lift and moment time histories when the shock moved across a grid point. To remove this jump, the calculation of ϕ_{xx} has been modified. In the present method, ϕ_x is calculated using central differences. A linear least-squares fit to five successive values of ϕ_x is calculated and the slope of this line is taken as the value of ϕ_{xx} at the center point. To calculate ϕ_{xx} at the two grid points nearest the airfoil trailing edge, the last five points on the airfoil are used. Calculations that show the effect of this modification upon the calculated unsteady loads are presented in appendix B.

3. An option was added to allow for iterating the viscous-inviscid solutions at each time step. Note that iterations were not required when moderate-strength shocks were located near midchord and the reduced frequency was greater than 0.1. For low values of reduced frequency ($k < 0.1$) or for cases with strong shocks located well back on the airfoil, iterating between the inviscid and viscous solutions at each time step can significantly improve the accuracy of the calculated results. No case has been found that required more than two iterations. For computational efficiency, these iterations are done only over the y-sweep of the alternating-direction implicit (ADI) solution of equation (1). (See ref. 16.)

4. In the original method (ref. 13), the viscous equations were integrated using a second-order Runge-Kutta algorithm with the values of ϕ_x and ϕ_{xx} specified at each inviscid-solution grid point on the airfoil and wake. For the computational grid used in this study, the integration spatial step size was found to be too coarse because of the rapid stretching of the grid in the near wake, and thus a finer step size was used for integration of the boundary-layer equations. Ten boundary-layer grid points were used between

4

each pair of inviscid-solution grid points. The required values of ϕ_x and ϕ_{xx} at the refined viscous grid points were determined by interpolation.

5. The boundary layer is calculated from the airfoil leading edge to a user-specified point on the airfoil (default value for this point is 10 percent chord) using the theory for turbulent flow over a flat plate. From this point to the downstream boundary, Green's lag-entrainment equations are numerically integrated with a second-order Runge-Kutta algorithm. No special provision is made for numerically integrating through the shock. This allows a consistent description of the boundary layer from the specified point to the downstream boundary. In contrast, Rizzetta (ref. 13) inserts a semiempirical viscous wedge at the base of the shock and integrates the boundary-layer equations from that point on.

The computer time for the viscous code with the above modifications is approximately 1.8 times the computer time for an inviscid calculation.

Results and Discussion

Test Cases

The accuracy of the present method is evaluated by selecting several test cases recommended by AGARD (ref. 4) and comparing the computed viscous loads with measured data and computed inviscid loads from reference 3. All the AGARD cases for the NACA 64A006 and NACA 64A010A airfoils are included as well as calculations for six of the MBB-A3 airfoil cases and four of the NACA 0012 cases. The calculated results presented herein correspond to the AGARD cases and have not been corrected for wind-tunnel test conditions. It should be noted that the NACA 64A010A airfoil has the coordinates of the section tested at the NASA Ames Research Center (given in ref. 4), has a small amount of camber, and is thicker than the symmetric design section. Profiles of the airfoil sections are presented in figure 1. Tables I to IV give the test conditions for analysis of each of these cases. The reduced frequency k is based on the semichord.

The modes of motion are described by the following equations:

For pitch,
$$\alpha(\bar{t}) = \alpha_m + \alpha_o \sin \omega \bar{t}$$

For plunge,
$$h(\bar{t}) = h_o \sin \omega \bar{t}$$

For control surface rotation,
$$\beta(\bar{t}) = \beta_m + \beta_o \sin \omega \bar{t}$$

In these equations, α_m is the mean angle of attack, β_m is the mean angle of rotation of the control surface, and $\omega = 2kU/c$. In all cases, three cycles of unsteady motion are calculated in order to allow transients to decay. Typically, 360 time steps per cycle of oscillation are used for the unsteady solutions. Pressure calculations for the analytical results use the linearized transonic small-disturbance approximation (ref. 20)

$$C_p = -2(\phi_x + \phi_t)$$

For each airfoil, the steady-flow pressure distributions are first shown for each Mach number to be analyzed. The unsteady results for each of the AGARD computational test cases are then given with four plots grouped together on one page for each case. The plots on these figures show the following: (a) the mean pressure distribution over the airfoil chord during the last cycle of harmonic motion, (b) the lifting pressure (lower minus upper surface pressure), (c) the upper surface pressure, and (d) the lower surface pressure. The unsteady pressures are presented as real (in phase) and imaginary (in quadrature) parts of the first-harmonic component of the pressure computed from the last cycle of the imposed simple harmonic motion using a fast Fourier transform analysis. These first-harmonic components are normalized by the nondimensional amplitude of motion, i.e., angle of attack and flap rotation (in radians) or plunge displacement (in chords), as appropriate. Although the harmonic pressures plotted on each figure are shown to the same scale, there is some variation in the scales between the figures. In addition to the plotted pressure distributions, the first-harmonic components of the force coefficients are given in tables V to VIII.

NACA 64A006 Airfoil

The test cases for the NACA 64A006 airfoil were chosen to match the experimental conditions of reference 22. All cases involve oscillation of a flap with a hinge axis located at the three-quarter chord, and the mean flap angle is zero. The cases include five Mach numbers, two frequencies, and two oscillation amplitudes (table I). All analytical cases used a Reynolds number of 2.30×10^6.

The steady-flow pressure distributions for the viscous and inviscid calculations are shown in figure 2 and are compared with the measured pressures. The figure shows that for steady flow, the inviscid results are quite good for subcritical Mach numbers, although the viscous calculations are closer to the experimental values near the trailing edge. As the Mach number is increased to 0.850, a shock wave

develops and the agreement of inviscid pressures with experiment begins to deteriorate (fig. 2(c)). The location and strength of the shock wave are predicted better by the viscous theory, and the viscous pressures show better agreement downstream of the shock. As the shock becomes stronger and moves aft on the airfoil, agreement of the viscous calculations with the experiment begins to deteriorate, although the viscous pressures are still closer to the experiment than the inviscid calculations (fig. 2(d)). For a Mach number of 0.960 (fig. 2(e)), both the inviscid and viscous calculations place the shock at the trailing edge, whereas the experimental value is about $x/c = 0.88$.

In this connection, it should be noted that potential theory is known to predict nonunique results in certain cases with strong shocks (ref. 23). For conditions near the regions of nonuniqueness, potential theory can also be seriously in error (ref. 24). Entropy corrections to the TSD theory have been developed by Fuglsang and Williams in reference 25 and offer promise of more accurate solutions for flows with strong shock waves.

The calculated boundary-layer displacement thicknesses that correspond to the steady cases of figure 2 are shown in figure 3. For all the cases, the flow is attached with no evidence of even mild separation. As the figure shows, for subcritical Mach numbers the effect of increasing Mach number is a slight increase in the displacement thickness on the aft part of the airfoil. As the shock wave develops near midchord ($M = 0.850$), the displacement thickness increases noticeably across the shock. For the strong shock case ($M = 0.875$), the boundary-layer displacement thickness doubles in value across the shock wave. As the Mach number is increased to 0.960, the shock wave moves downstream to the trailing edge, and the decreasing pressure gradient upstream of the shock results in reduced values of displacement thickness on the aft part of the airfoil.

Results for the unsteady pressure distributions are given in figures 4 to 15, and results for the unsteady lift, pitching-moment, and hinge-moment coefficients are given in table V. The mean pressures from the unsteady pressure calculations (part (a) of figs. 4 to 15) are very similar to the steady pressures. The first harmonics of the unsteady pressure distributions are shown in parts (b) to (d) of figures 4 to 15. Figures 4 to 8 show close agreement between viscous and inviscid calculations for subcritical cases, with the viscous results being slightly closer to the experimental values except near the flap hinge line where the viscous theory underpredicts the pressure singularity. As illustrated in figures 4 and 5, better agreement between theory and experiment occurs at the higher frequency. For $M = 0.825$ (figs. 6 to 8),

the calculated unsteady pressures indicate the onset of a shock wave near 40 percent chord, although the effects of viscosity relieve this significantly and it is not seen in the experiment. The boundary layer has a large effect on the unsteady pressures even when the steady flow effects are small. Both the calculated and experimental mean pressures for these cases indicate that the flow is subcritical in agreement with the steady results (fig. 2(b)). The calculated effect of increasing the amplitude of the flap motion from $1°$ to $2°$ is to displace the shock position aft about 5 percent chord (figs. 6 and 7). A comparison of figures 6 and 8 provides another example that better agreement between theory and experiment occurs at the higher frequency.

At Mach numbers of 0.850 and 0.875 (figs. 9 to 13), a shock has developed and the viscous calculations correct about one-half of the discrepancy between the experiment and the inviscid shock pulse for both the real and imaginary components. For $M = 0.850$ the shock pulse is well upstream of the flap hinge line and the predicted pressures on the flap are in excellent agreement with the experiment for both frequencies. As the Mach number is increased to 0.875, the experimental shock peak (near $x/c = 0.55$) and hinge peak ($x/c = 0.75$) are easily distinguished, whereas in the calculated results the two peaks are merged into one. The viscous calculations do show an indication of two peaks. Once the calculated shock pulse reaches the flap hinge line, the flap pressures predicted by the viscous theory begin to deviate from the experiment. At $M = 0.875$, the effect of increasing the flap oscillation amplitude from $1°$ to $2°$ at the lower frequency ($k = 0.059$) may be seen by comparing figures 11 and 12. The shock oscillates over a larger distance at the larger amplitude with the center of the shock pulse being displaced aft about 5 percent chord.

The calculated unsteady pressure results at $M = 0.960$ (figs. 14 and 15) are qualitatively different from the experimental data. The potential flow code has placed the shock wave at the trailing edge in contrast to the experimental value of $x/c \approx 0.88$. (See fig. 2(e).) Both theory and experiment show very small unsteady pressures ahead of the flap.

Forces and moments from the unsteady calculations are given in table V along with experimental values and linear theory. Summary plots are presented in figures 16 and 17. As shown in figure 16 for the low frequency cases ($k = 0.06$), the viscous results correct up to 30 percent of the difference between the inviscid results and the experiment for the lower Mach numbers. However, the calculated results still tend to diverge from the experimental values for the strong shock cases as shown by the imaginary

component of c_{m_β} in figure 16(b). Figure 17 shows that the inviscid results agree better with the experiment for the moderate frequency case ($k = 0.24$) than for the low frequency case, and the inclusion of viscous effects generally improves the agreement. For both frequencies the viscous corrections to c_{l_β} are very good at the higher Mach numbers. The linear theory results are competitive with the computational fluid dynamics (CFD) results for predicting the integrated forces and moments for most of the cases investigated for this airfoil.

NACA 64A010A Airfoil

The AGARD cases for the NACA 64A010A airfoil are listed in table II and detailed plots are presented in figures 18 to 30. The cases are for the model tested at the NASA Ames Research Center (ref. 26) and include essentially two Mach numbers ($M = 0.5$ and 0.8), two Reynolds numbers, and several frequencies and amplitudes of pitch oscillation about the quarter-chord. The airfoil has a very small amount of camber and surface waviness, as is evident in the steady pressure distributions shown in figure 18. For the low Mach number cases (figs. 18(a) and (b)), the agreement between theory and experiment is excellent with virtually no viscous effects. Figures 18(c) to (e) present the high Mach number results with part (e) giving the low Reynolds number case. For the high Mach number cases, small viscous effects are evident with the viscous shock being slightly forward and weaker. In general, the agreement between the experiment and both the viscous and inviscid calculations is quite good.

The effect of Reynolds number on calculated boundary-layer displacement thicknesses for the steady computations is shown in figure 19. The low Mach number results (fig. 19(a)) show a definite reduction in the boundary-layer displacement thickness for the higher Reynolds number case even though the calculated pressures (figs. 18(a) and (b)) indicate no significant viscous effects. The high Mach number results (fig. 19(b)) show a similar reduction in boundary-layer displacement thickness with increasing Reynolds number with a noticeably larger reduction downstream of the shock.

The first harmonics of the unsteady pressure distributions are shown in figures 20 to 29. At $M \approx 0.5$ (figs. 20 and 21) the viscous and inviscid results are virtually indistinguishable as was previously indicated for the steady-flow calculations. The agreement between theory and experiment is excellent with perhaps better agreement at the higher Reynolds number (fig. 21). The remaining results are for $M \approx 0.8$. Cases 3 to 7 (figs. 22 to 26, respectively) illustrate frequency effects, with k

ranging from about 0.025 to 0.3. For each of these cases, the viscous calculations correct more than 50 percent of the discrepancy in the shock pulse location shown by the inviscid calculations. The systematic decrease in calculated shock pulse width with increasing frequency is evident, with agreement of theory and experiment perhaps being somewhat better at the intermediate frequencies. Note particularly that the viscous calculations of the real and imaginary peak pressures are brought into very good agreement with the experimental values. The effect of the boundary layer on the unsteady pressures is large even though the steady-flow effects are small. Ahead of the shock the calculated unsteady pressures show a systematic trend in which the pressures are overpredicted at low frequencies and underpredicted at higher frequencies. This trend is true for both the real and imaginary components of the pressure and is affected very little by viscosity. Behind the shock the viscous calculations alleviate the post-shock reexpansion seen in the inviscid calculations at approximately 65 percent chord, leading to generally better agreement with experiment.

Cases 6 and 10 (figs. 25 and 29) were chosen to illustrate the effect of Reynolds number, although the slight differences in Mach number, amplitude, and frequency may obscure the comparison. At the higher Reynolds number (fig. 25), the viscous calculation appears to agree better with the experiment than at the lower Reynolds number (fig. 29). The minimal effect of Reynolds number shown in the experimental results is correctly predicted by the viscous calculations, and the viscous results agree better with the experiment than the inviscid results at both Reynolds numbers.

The effect of oscillation amplitude is illustrated by comparing figures 24, 27, and 28 for $\alpha_o = 1.02°$, 0.51°, and 2.00°, respectively, and at $k = 0.101$. For smaller amplitudes, the shock pulse is narrower (because of less shock motion) and higher (because of amplitude normalization). (Note the different scale in fig. 27.) Away from the shock, the plotted normalized pressures (i.e., divided by oscillation amplitude) for both theories and experiments are essentially the same for all three cases. Although not shown herein, higher harmonic content was evident in the pressure time histories and provided some evidence of the nonlinear effect of increased oscillation amplitudes.

A summary of the calculated unsteady lift and pitching-moment coefficients is presented in table VI together with the experimental values and linear theory. Summary plots are shown in figure 30. In general, the viscous corrections improve the agreement between the calculations and the experiment.

The XTRAN2L inviscid results deviate from the experiment at the lowest frequencies but otherwise show proper trends with increasing frequency.

MBB-A3 Airfoil

The six test cases studied for the MBB-A3 airfoil are listed in table III. The selected cases are specified to be at the supercritical design point ($M = 0.765$, $\alpha_m = 1.5°$, and $c_l = 0.519$) given in reference 4. Included are cases for airfoil pitch oscillation about the quarter-chord and for plunge oscillation, each at three reduced frequencies, $k = 0.1, 0.3$, and 0.9. The Reynolds number is 6×10^6 for all cases. The calculated cases are for the actual experimental values of Mach number and angle of attack rather than for values that have been adjusted to match flow conditions in the wind tunnel, as is frequently done in comparisons with these particular data. The pressure distributions are presented in figures 31 to 37, and the unsteady lift and pitching-moment coefficients are presented in table VII. Calculated values only are presented for the six unsteady cases.

The steady pressure distribution is shown in figure 31. The experimental data are taken from figure 8.2 of reference 27. The experiment shows a supercritical flow without a discernible shock wave typical of the flow at the design point. The region of supercritical flow terminates at about $x/c = 0.53$. The viscous calculation indicates a moderate-strength shock wave at nearly the same location with $c_l = 0.568$. Away from the shock, agreement between the viscous calculation and the experiment is very good, although some discrepancies are noted near the leading edge. The viscous solution shows a marked improvement over the inviscid calculation, especially downstream of the region of supercritical flow. For this case, the inclusion of viscous effects yields a significant improvement in the calculation of the steady pressure distribution.

The calculated unsteady pressure distributions for the MBB-A3 airfoil are given in figures 32 to 37. In all cases, the viscous calculations for the upper surface are substantially different from the inviscid calculations insofar as shock location and strength are concerned. For the (subcritical) lower surface, both viscous and inviscid calculations are nearly coincident. The effect of varying frequency from $k = 0.1$ to 0.9 may be seen by comparing figures 32 to 34 for pitch and figures 35 to 37 for plunge. For pitch, increasing the frequency to $k = 0.9$ leads to a decrease in the magnitude of the shock pulse. This effect is more pronounced for the inviscid calculations. For plunge, the most obvious effect is the increasing overall pressure level with increasing frequency. This increase is consistent with

piston theory which predicts forces proportional to frequency.

The calculated viscous and inviscid unsteady forces listed in table VII are plotted in figure 38. As the figure shows, the differences between the viscous and inviscid results decrease with increasing frequency. In the low frequency region, the inviscid solutions seem to exhibit a nonphysical behavior in that the imaginary components do not approach zero as the frequency tends toward zero. In contrast, the imaginary components of the viscous solutions are clearly tending toward zero with decreasing frequency.

NACA 0012 Airfoil

The AGARD cases investigated for the NACA 0012 airfoil involve greater mean angles of attack (up to $4.86°$) and larger amplitude pitch oscillations (up to $4.59°$) than those studied previously for the other airfoils. Although application of the small-disturbance theory to these cases may be questionable, the results are presented here to evaluate further the limits of the present theory. Unsteady pressure distributions are compared on the basis of first-harmonic components only. The experimental pressure data presented were obtained by harmonic analysis of the time history data given in reference 28. The experiments were conducted as part of a study of dynamic stall, and no steady measurements were reported. The test cases are listed in table IV, and the results are presented in figures 39 to 44 and table VIII.

Steady pressure distributions for viscous and inviscid calculations are presented in figure 39. The main viscous effects are a decrease in the leading-edge suction peak and a slight rise in the pressure level on the lower surface. For case 5 (fig. 39(d)), viscous effects are negligible. In all cases, the numerical values of the boundary-layer shape parameter suggest that the flow is close to separation at the trailing edge.

The unsteady pressure distributions are shown in figures 40 to 43. Note that for cases 2 and 3 (figs. 41 and 42), no viscous results could be obtained because of the severity of the test cases, that is, the probable onset of flow separation at the trailing edge. As shown in figure 40, for case 1 the viscous effects are small and the viscous calculation underpredicts both the inviscid method and the experiment. For cases 2 and 3, the inviscid calculations underpredict the mean pressures but the first harmonics of the unsteady pressures are quite accurate. In test case 5 (fig. 43) the inviscid result slightly underpredicts the mean pressure and agrees well with the unsteady pressures. The unsteady viscous results for case 5 indicate a viscous effect even though the steady

calculation (fig. 39(d)) is virtually identical to the inviscid result. The viscous calculation underpredicts both the inviscid calculation and the experiment.

Plots of the lift and pitching-moment coefficients versus α for the oscillatory cases 1, 2, 3, and 5 are presented in figure 44. The lift coefficient comparisons are from very good to good with the inviscid results being closer to the experiment than the viscous results for cases 1 and 5. The pitching-moment coefficients show a systematic difference between the experimental and calculated values that may result from the underprediction of leading-edge-suction peak pressures on the upper surface discussed above. For case 1, the inviscid calculation is closer to the experiment than the viscous calculation, whereas for case 5 both the inviscid and viscous moment coefficients are of comparable accuracy. The characteristic shape of the c_m versus α curves is indicative of a large contribution of the second harmonic. In figure 44(d), the different shape of the c_m versus α curve is a result of an increased amplitude of the third-harmonic component. These cases demonstrate that the inviscid XTRAN2L code can predict with reasonable accuracy the airloads due to large-amplitude pitch oscillations, whereas the viscous code (for attached flow) encounters computational difficulties undoubtedly due to the onset of flow separation at the trailing edge.

Conclusions

A method is presented for calculating unsteady transonic flow with viscous interaction. The method uses Green's steady-flow lag-entrainment equations in connection with an unsteady, transonic, inviscid small-disturbance computer code. The viscous equations are explicitly coupled with the unsteady code in a quasi-steady manner. The method includes an option that allows viscous-inviscid iterations at each time step to ensure converged solutions. The method has been applied to several transonic test cases recommended by the AGARD Structures and Materials Panel. Comparisons with both inviscid analyses and experiments are presented. The results demonstrate that accurate solutions to transonic flows with viscous effects are obtained for flows involving moderate-strength shock waves. The following general conclusions may be drawn from the results:

1. For the conventional NACA 64A006 and 64A010A airfoils with weak or moderate-strength shock waves, the viscous calculations compare more favorably with the experiments than do the inviscid calculations, especially in the vicinity of the shock pulse. The pressures downstream of the shock are more accurately predicted by the viscous calculations.

2. For flows involving strong shocks located well aft on the airfoil, both the viscous and inviscid calculations deteriorate, although the viscous shock is generally somewhat forward and slightly weaker than the inviscid shock.

3. For subcritical cases, viscous and inviscid calculations are in good agreement with each other and with experimental data.

4. Frequency effects are well predicted, with agreement being noticeably better between viscous calculations and experiment at intermediate frequencies. The effect of increasing the oscillation frequency is to narrow the shock pulse.

5. The effect of increasing the oscillation amplitude is well predicted by both viscous and inviscid calculations with the viscous results being closer to the experiments. Higher amplitude motions have a larger unsteady shock motion with a broader shock pulse in the harmonic pressure distributions.

6. Prediction of unsteady forces by the viscous theory is good to marginal. The unsteady moments from the viscous calculations show the same trends as the experimental data, but some differences are noted in amplitude.

7. The effect of the boundary layer on unsteady pressures can be large even though steady-flow effects are small.

8. For the supercritical MBB-A3 airfoil, the steady-flow pressure distribution calculated by the viscous theory is in excellent agreement with the experiment, whereas the inviscid results are quite different. Calculated unsteady results show substantial viscous effects.

9. Results for the NACA 0012 airfoil are calculated at high mean angles of attack and large oscillation amplitudes that may be outside the limits of the small-disturbance theory. The inviscid XTRAN2L code predicts the airloads with reasonable accuracy, whereas the viscous code (for attached flow) encounters computational difficulties, undoubtedly due to the onset of flow separation at the trailing edge.

10. The results presented demonstrate that viscous solutions computed with the present algorithm can provide predictions of pressure distributions for unsteady transonic flow involving moderate-strength shock waves that correlate better, sometimes significantly better, with experimental values than do the inviscid solutions.

Appendix A

Summary of Boundary-Layer Equations

The boundary-layer equations used in the present analysis are based upon the integral method of Green (ref. 12) as implemented by Rizzetta (ref. 13). The displacement thickness δ^* is computed as a function of the boundary-layer momentum thickness θ and the shape factor H:

$$\delta^* = \theta \cdot H$$

The functions θ and H in this equation are determined, together with the entrainment coefficient C_E from Green's lag-entrainment equations. In the nondimensional variables consistent with equation (1), these equations are (ref. 13)

$$\frac{d}{dx}\left(\frac{\theta}{c}\right) = f_1 + f_2\phi_{xx} = \frac{C_f}{2} - (H + 2 - M_e^2)\varepsilon^{2/3}\frac{\theta}{c}\phi_{xx} \tag{A1}$$

$$\frac{\theta}{c}\frac{d\overline{H}}{dx} = f_3 + f_4\phi_{xx} = \left(C_E - \frac{H_1}{2}C_f\right)\frac{d\overline{H}}{dH_1} + H_1(H+1)\frac{d\overline{H}}{dH_1}\varepsilon^{2/3}\frac{\theta}{c}\phi_{xx} \tag{A2}$$

$$\frac{\theta}{c}\frac{dC_E}{dx} = f_5 + f_6\phi_{xx} = F\left\{\frac{2.8}{H+H_1}\left[(C_\tau)_{\text{EQO}}^{1/2} - \lambda C_\tau^{1/2}\right]\right.$$

$$\left. + \left(\frac{\theta}{U_e}\frac{dU_e}{d\xi}\right)_{\text{EQ}}\right\} - F\left[1 + 0.075M_e^2\,\frac{1 + \frac{\gamma-1}{2}rM_e^2}{1 + 0.1M_e^2}\right]\varepsilon^{2/3}\frac{\theta}{c}\phi_{xx} \tag{A3}$$

The subscript e in these equations refers to quantities evaluated at the boundary-layer edge, the subscript EQ denotes the equilibrium conditions, and the subscript EQO denotes the equilibrium conditions in absence of secondary influences on the turbulence structure. The various dependent variables and functions are evaluated from the following expressions:

$$\frac{U_e}{U} = 1 + \varepsilon^{2/3}\phi_x$$

$$\frac{M_e}{M} = 1 + \left(1 + \frac{\gamma - 1}{2}M^2\right)\varepsilon^{2/3}\phi_x$$

$$\frac{\rho_e}{\rho} = 1 - M^2\varepsilon^{2/3}\phi_x$$

$$\frac{T_e}{T} = 1 - (\gamma - 1)\varepsilon^{2/3}M^2\phi_x$$

$$\frac{\mu_e}{\mu} = \left(\frac{T_e}{T}\right)^{3/2}\frac{1 + (N_{\text{Su}}/T)}{(T_e/T) + (N_{\text{Su}}/T)}$$

$$F = \frac{0.02C_E + C_E^2 + \frac{0.8C_{fo}}{3}}{0.01 + C_E}$$

$$C_\tau = \left(1 + 0.1M_e^2\right)\left(0.024C_E + 1.2C_E^2 + 0.32C_{fo}\right)$$

$$\lambda = \begin{cases} 1 & \text{(on airfoil)} \\ 1/2 & \text{(on wake)} \end{cases}$$

$$\left(\frac{\theta}{U_e}\frac{dU_e}{d\xi}\right)_{\text{EQO}} = \frac{1.25}{H}\left[\frac{C_f}{2} - \left(\frac{\overline{H} - 1}{6.432\overline{H}}\right)^2(1 + 0.04M_e^2)^{-1}\right]$$

$$(C_E)_{\mathrm{EQO}} = H_1 \left[\frac{C_f}{2} - (H+1) \left(\frac{\theta}{U_e} \frac{dU_e}{d\xi} \right)_{\mathrm{EQO}} \right]$$

$$(C_\tau)_{\mathrm{EQO}} = \left(1 + 0.1 M_e^2 \right) \left[0.024(C_E)_{\mathrm{EQO}} + 1.2(C_E)_{\mathrm{EQO}}^2 + 0.32 C_{fo} \right]$$

$$N_{\mathrm{Re},\theta} = \frac{(\rho_e/\rho)\ (U_e/U)\ (\theta/c)}{\mu_e/\mu} N_{\mathrm{Re}}$$

$$r = N_{\mathrm{Pr},t}^{1/3}$$

$$F_c = \left(1 + \frac{\gamma - 1}{2} r M_e^2 \right)^{1/2}$$

$$F_r = 1 + 0.056 M_e^2$$

$$C_{fo} = \frac{1}{F_c} \left[\frac{0.01013}{\log_{10}(F_r N_{\mathrm{Re},\theta}) - 1.02} - 0.00075 \right]$$

$$\frac{\overline{H}}{\overline{H}_o} = \overline{H} \left\{ 1 - 6.55 \left[\frac{C_{fo}}{2} \left(1 + 0.04 M_e^2 \right) \right]^{1/2} \right\}$$

$$C_f = \begin{cases} C_{fo} \left[0.9 \left(\frac{\overline{H}}{\overline{H}_o} - 0.4 \right)^{-1} - 0.5 \right] & \text{(on airfoil)} \\ 0 & \text{(on wake)} \end{cases}$$

$$H = (\overline{H} + 1) \left(1 + \frac{\gamma - 1}{2} r M_e^2 \right) - 1$$

$$H_1 = 3.15 + \frac{1.72}{\overline{H} - 1} - 0.01(\overline{H} - 1)^2$$

$$\frac{d\overline{H}}{dH_1} = -\frac{(\overline{H} - 1)^2}{1.72 + 0.02(\overline{H} - 1)^3}$$

$$C = (C_\tau)_{\mathrm{EQO}}(1 + 0.1 M_e^2)^{-1} \lambda^{-2} - 0.32 C_{fo}$$

$$(C_E)_{\mathrm{EQ}} = \left(\frac{C}{1.2} + 0.0001 \right)^{1/2} - 0.01$$

$$\left(\frac{\theta}{U_e} \frac{dU_e}{d\xi} \right)_{\mathrm{EQ}} = \left[\frac{1}{H_1(H+1)} \right] \left[\frac{H_1 C_f}{2} - (C_E)_{\mathrm{EQ}} \right]$$

The additional parameters required to specify the boundary-layer equations completely, together with the default values in the code (in parentheses), are the free-stream chord Reynolds number N_{Re} (10^7), the free-stream temperature T in degrees kelvin (300 K), the turbulent Prandtl number $N_{\mathrm{Pr},t}$ (0.9 for air), and the Sutherland law viscosity constant N_{Su} in degrees kelvin (110 K for air). With the exception of the Reynolds number, the default values were used in all the calculations presented herein.

With these definitions, and the inviscid velocity potential ϕ from the inviscid solution algorithm, the lag-entrainment equations are fully defined. The values of $\theta, H,$ and C_E at the initial streamwise station are determined from the equations for turbulent flow over a flat plate. Downstream of the initial station, equations (A1), (A2), and (A3) are numerically integrated to obtain the viscous parameters.

Appendix B

Effect of Upwind Switch in Boundary-Layer Calculations

A test case for the NACA 64A010A airfoil has been calculated both with and without the type-dependent differencing in the boundary-layer calculations to demonstrate the improvement that has been obtained. The parameters for this test case correspond with those of case 3 in table II: $M = 0.796$ and $\alpha_m = 0°$. A converged steady viscous solution was used as a starting solution for the airfoil undergoing harmonic oscillations in pitch. Although both the lift and pitching moment calculated with type-dependent differencing have the spurious amplitude effect, only the pitching-moment result is shown here since it is the more sensitive parameter. A plot of the calculated pitching-moment time history is shown in figure 45. The jump due to upwind switching can be clearly seen. The pitching-moment time history calculated with the present code (no switching) oscillates harmonically with no indication of the jump.

The present method (no switching) is further evaluated for the same airfoil by recalculating some results of Berry et al. presented in reference 29, which used the method with type-dependent differencing and showed significant amplitude effects. In these calculations, the airfoil is given a small prescribed pulse motion in pitch, and a fast Fourier transform is used to calculate the aerodynamic forces. For this case, the Mach number is 0.796 and $\alpha_m = -0.21°$. The pulse computations presented by Berry et al. (see fig. 5 of ref. 29) showed that the magnitude of the unsteady viscous lift coefficient increased as the pulse amplitude increased from 0.1° to 1.0°. This calculation was repeated with the present code for pulse amplitudes from 0.1° to 4.0°. The results are shown in figure 46, which presents plots of the lift coefficient as a function of reduced frequency for pulse amplitudes of 0.1° and 4.0°. As the figure shows, for reduced frequencies less than 0.8, no amplitude effects are indicated. At reduced frequencies greater than 0.8, the results for 4.0° deviate slightly from those at 0.1°. Berry et al. also presented aeroelastic calculations including viscous effects that showed significant amplitude effects, very likely due to inclusion of type-dependent differencing in the viscous boundary-layer calculation.

References

1. Ballhaus, W. F.; and Goorjian, P. M.: Implicit Finite-Difference Computations of Unsteady Transonic Flows About Airfoils. *AIAA J.*, vol. 15, no. 12, Dec. 1977, pp. 1728–1735.

2. Edwards, J. W.; Bland, S. R.; and Seidel, D. A.: *Experience With Transonic Unsteady Aerodynamic Calculations.* NASA TM-86278, 1984.

3. Bland, Samuel R.; and Seidel, David A.: *Calculation of Unsteady Aerodynamics for Four AGARD Standard Aeroelastic Configurations.* NASA TM-85817, 1984.

4. Bland, S. R., compiler: *AGARD Two-Dimensional Aeroelastic Configurations.* AGARD-AR-156, Aug. 1979.

5. Melnik, R. E.; Chow, R. R.; Mead, H. R.; and Jameson, A.: *An Improved Viscid/Inviscid Interaction Procedure for Transonic Flow Over Airfoils.* NASA CR-3805, 1985.

6. Shamroth, Stephen J.: *Calculation of Steady and Unsteady Airfoil Flow Fields Via the Navier-Stokes Equations.* NASA CR-3899, 1985.

7. Rumsey, Christopher L.; Thomas, James L.; Warren, Gary P.; and Liu, Grace C.: Upwind Navier-Stokes Solutions for Separated Periodic Flows. AIAA-86-0247, Jan. 1986.

8. Melnik, R. E.: Turbulent Interactions on Airfoils at Transonic Speeds—Recent Developments. *Computation of Viscous-Inviscid Interactions,* AGARD-CP-291, Feb. 1981, pp. 10-1–10-34.

9. Streett, Craig L.: Viscous-Inviscid Interaction for Transonic Wing-Body Configurations Including Wake Effects. *AIAA J.*, vol. 20, no. 7, July 1982, pp. 915–923.

10. LeBalleur, J. C.; and Girodroux-Lavigne, P.: A Viscous-Inviscid Interaction Method for Computing Unsteady Transonic Separation. *Third Symposium on Numerical and Physical Aspects of Aerodynamic Flows,* California State Univ., Jan. 1985, pp. 5–49.

11. Houwink, R.; and Veldman, A. E. P.: Steady and Unsteady Separated Flow Computations for Transonic Airfoils. AIAA-84-1618, June 1984.

12. Green, J. E.; Weeks, D. J.; and Brooman, J. W. F.: *Prediction of Turbulent Boundary Layers and Wakes in Compressible Flow by a Lag-Entrainment Method.* R. & M. No. 3791, British Aeronautical Research Council, 1977.

13. Rizzetta, Donald P.: *Procedures for the Computation of Unsteady Transonic Flows Including Viscous Effects.* NASA CR-166249, 1982.

14. Guruswamy, P.; and Goorjian, P. M.: Effects of Viscosity on Transonic-Aerodynamic and Aeroelastic Characteristics of Oscillating Airfoils. *A Collection of Technical Papers, Part 2: Structural Dynamics— AIAA/ASME/ASCE/AHS 24th Structures, Structural Dynamics and Materials Conference,* 1983, pp. 253–165. (Available as AIAA-83-0888.)

15. Houwink, R.: *Results of a New Version of the LTRAN2-NLR Code (LTRANV) for Unsteady Viscous Transonic Flow Computations.* NLR TR 81078 U, National Aerospace Lab. NLR (Amsterdam, Netherlands), July 7, 1981.

16. Howlett, James T.: Efficient Self-Consistent Viscous-Inviscid Solutions for Unsteady Transonic Flow. AIAA-85-0482, Jan. 1985.

17. Whitlow, Woodrow, Jr.: *XTRAN2L: A Program for Solving the General-Frequency Unsteady Transonic Small Distrubance Equation.* NASA TM-85723, 1983.

18. *Compendium of Unsteady Aerodynamic Measurements.* AGARD-R-702, Aug. 1982.

19. Houwink, R.; and Van der Vooren, J.: Improved Version of LTRAN2 for Unsteady Transonic Flow Computations. *AIAA J.*, vol. 18, no. 8, Aug. 1980, pp. 1008–1010.

20. Seidel, David A.; and Batina, John T.: *User's Manual for XTRAN2L (Version 1.2): A Program for Solving the General-Frequency Unsteady Transonic Small-Disturbance Equation.* NASA TM-87737, 1986.

21. Seidel, David A.; Bennett, Robert M.; and Whitlow, Woodrow, Jr.: *An Exploratory Study of Finite Difference Grids for Transonic Unsteady Aerodynamics.* NASA TM-84583, 1982.

22. Tijdeman, H.; and Schippers, P.: *Results of Pressure Measurements on an Airfoil With Oscillating Flap in Two-Dimensional High Subsonic and Transonic Flow (Zero Incidence and Zero Mean Flap Position).* NLR TR 73078 U, National Lucht- Ruimtevaartlab. (Amsterdam), July 13, 1973.

23. Salas, M. D.; Jameson, A.; and Melnik, R. E.: *A Comparative Study of the Nonuniqueness Problem of the Potential Equation.* NASA TP-2385, 1985.

24. Salas, M. D.; and Gumbert, Clyde R.: *Breakdown of the Conservative Potential Equation.* NASA TP-2539, 1986.

25. Fuglsang, Dennis F.; and Williams, Marc H.: NonIsentropic Unsteady Transonic Small Disturbance Theory. *A Collection of Technical Papers, Part 2: Structural Dynamics—AIAA/ASME/ASCE/AHS 26th Structures, Structural Dynamics and Materials Conference,* 1985, pp. 83–95. (Available as AIAA-85-0600.)

26. Davis, Sanford S.; and Malcolm, Gerald N.: *Experimental Unsteady Aerodynamics of Conventional and Supercritical Airfoils.* NASA TM-81221, 1980.

27. Bucciantini, G.; Oggiano, M. S.; and Onorato, M.: Supercritical Airfoil MBB-A3 Surface Pressure Distributions, Wake and Boundary Condition Measurements. *Experimental Data Base for Computer Program Assessment,* AGARD-AR-138, May 1979, pp. A8-1–A8-25.

28. Landon, R. H.: NACA 0012. Oscillatory and Transient Pitching. *Compendium of Unsteady Aerodynamic Measurements,* AGARD-R-702, Aug. 1982, pp. 3-1–3-25.

29. Berry, H. M.; Batina, J. T.; and Yang, T. Y.: Viscous Effects on Transonic Airfoil Stability and Response. *J. Aircr.*, vol. 23, no. 5, May 1986, pp. 361–369.

Table I. Analytical Test Cases for NACA 64A006 Airfoil

$[\alpha_m = \alpha_o = \beta_m = 0°; \ x_\beta/c = 0.75]$

Case	M	N_{Re}	β_o, deg	f, Hz	k
1	0.800	2.30×10^6	1	30	0.064
2	.800		1	120	.254
3	.825		1	30	.062
4	.825		2	30	.062
5	.825		1	120	.248
6	.850		1	30	.060
7	.850		1	120	.242
8	.875		1	30	.059
9	.875		2	30	.059
10	.875		1	120	.235
11	.960		1	30	.054
12	.960		1	120	.217

Table II. Analytical Test Cases for NACA 64A010A Airfoil

$[\alpha_m = 0°; \ x_\alpha/c = 0.25]$

Case	M	N_{Re}	α_o, deg	f, Hz	k
1	0.490	2.5×10^6	0.96	10.4	0.100
2	.502	10.0	1.02	10.8	.100
3	.796	12.5	1.03	4.2	.025
4	.796	12.5	1.02	8.6	.051
5	.796	12.5	1.02	17.2	.101
6	.796	12.5	1.01	34.4	.202
7	.796	12.5	.99	51.5	.303
8	.796	12.5	.51	17.1	.101
9	.797	12.5	2.00	17.2	.101
10	.802	3.4	.94	33.2	.200

Table III. Analytical Test Cases for MBB-A3 Airfoil

$$\left[x_\alpha/c = 0.25; \ N_{\text{Re}} = 6 \times 10^6\right]$$

Case	M	α_m, deg	α_o, deg	h_o/c	k
3	0.765	1.5	0.50	0	0.100
4	↓	↓	.50	0	.300
5			.50	0	.900
11			0	.01	.100
12			0	.01	.300
13	↓	↓	0	.01	.900

Table IV. Analytical Test Cases for NACA 0012 Airfoil

$$[x_\alpha/c = 0.25]$$

Case	M	U, m/sec	N_{Re}	α_m, deg	α_o, deg	f, Hz	k
1	0.601	197	4.8×10^6	2.89	2.41	50	0.081
2	.599	197	4.8	3.16	4.59	50	↓
3	.599	197	4.8	4.86	2.44	50	
5	.755	243	5.5	0.02	2.51	62	↓

Table V. NACA 64A006 Airfoil Harmonic Forces

Case	Inviscid Real	Inviscid Imaginary	Viscous Real	Viscous Imaginary	Experiment Real	Experiment Imaginary	Linear Real	Linear Imaginary
Lift-curve slope due to flap rotation, c_{l_β}								
1	4.793	−2.053	4.474	−1.858	3.192	−0.817	4.412	−1.674
2	2.546	−1.744	2.404	−1.600	2.608	−1.238	2.596	−1.483
3	4.986	−2.459	4.629	−2.203	3.355	−.817	4.519	−1.854
4	5.006	−2.520	4.636	−2.232			4.519	−1.854
5	2.336	−1.968	2.218	−1.787	2.717	−1.508	2.517	−1.600
6	5.148	−3.434	4.783	−2.930	3.515	−.873	4.626	−2.074
7	1.672	−1.891	1.682	−1.796	2.504	−1.731	2.399	−1.709
8	3.568	−5.687	3.858	−4.624	3.663	−1.247	4.689	−2.353
9	3.493	−5.726	3.831	−4.455			4.689	−2.353
10	1.699	−1.372	1.648	−1.262	1.819	−1.505	2.235	−1.790
11	1.555	.025	1.566	.018	.543	.261	4.080	−3.797
12	1.537	−.004	1.553	−.026			2.051	−1.574
Pitching-moment-curve slope due to flap rotation, c_{m_β}								
1	−1.248	−0.052	−1.167	−0.042	−1.005	−0.016	−1.118	−0.060
2	−1.368	.024	−1.259	.032	−1.188	.030	−1.251	−.055
3	−1.383	−.043	−1.288	−.028	−1.070	−.035	−1.195	−.059
4	−1.405	−.036	−1.299	−.026			−1.195	−.059
5	−1.526	.172	−1.388	.163	−1.352	.101	−1.341	.004
6	−1.703	.103	−1.547	.074	−1.150	−.046	−1.292	−.056
7	−1.460	.685	−1.389	.576	−1.450	.231	−1.444	.097
8	−2.079	1.655	−1.997	1.238	−1.360	.099	−1.422	−.048
9	−2.062	1.835	−1.984	1.274			−1.422	−.048
10	−.902	.644	−.850	.594	−1.189	.514	−1.549	.245
11	−.963	−.013	−.966	−.010	−.280	−.170	−2.610	.451
12	−.956	.004	−.956	.017			−1.239	.699
Hinge-moment-curve slope due to flap rotation, c_{h_β}								
1	−0.082	−0.003	−0.083	−0.002	−0.060	−0.004	−0.090	0.000
2	−.082	−.024	−.081	−.019	−.066	−.018	−.088	−.021
3	−.083	−.005	−.085	−.002	−.062	−.006	−.095	.001
4	−.082	−.005	−.085	−.003			−.095	.001
5	−.087	−.026	−.087	−.020	−.075	−.019	−.094	−.021
6	−.080	−.013	−.085	−.007	−.062	−.009	−.101	.001
7	−.100	−.030	−.098	−.020	−.075	−.023	−.101	−.021
8	−.072	−.071	−.098	−.005	−.057	−.016	−.109	.001
9	−.111	.010	−.115	.027			−.109	.001
10	−.111	−.024	−.100	−.005	−.087	−.023	−.111	−.020
11	−.190	−.002	−.184	−.002	−.016	−.032	−.184	.005
12	−.188	.001	−.181	.004			−.180	.015

Table VI. NACA 64A010A Airfoil Harmonic Forces

Case	Inviscid Real	Inviscid Imaginary	Viscous Real	Viscous Imaginary	Experiment Real	Experiment Imaginary	Linear Real	Linear Imaginary
Lift-curve slope due to pitch, c_{l_α}								
1	5.767	−0.561	5.565	−0.521	6.139	−1.149	5.765	−0.612
2	5.802	−.581	5.649	−.549	6.136	−1.036	5.790	−.634
3	12.552	−4.202	11.141	−3.183	9.316	−1.378	9.020	−1.621
4	9.836	−4.092	9.094	−3.338	8.622	−2.479	7.920	−1.972
5	7.342	−3.446	7.033	−2.918	6.790	−3.387	6.639	−1.793
6	5.635	−2.157	5.487	−1.886	4.887	−2.521	5.585	−.952
7	4.942	−1.341	4.862	−1.157	4.635	−.905	5.265	−.227
8	7.370	−3.384	7.053	−2.892	6.795	−3.403	6.639	−1.793
9	7.247	−3.731	6.965	−3.029	6.141	−3.113	6.639	−1.793
10	5.496	−2.421	5.313	−1.976	5.308	−2.471	5.605	−1.005
Pitching-moment-curve slope due to pitch, c_{m_α}								
1	−0.052	−0.186	−0.023	−0.178	0.165	−0.163	−0.003	−0.196
2	−.054	−.189	−.032	−.183	.167	−.201	−.004	−.199
3	−.903	.169	−.637	.059	.000	−.102	−.013	−.095
4	−.709	.039	−.535	−.035	−.005	−.232	−.038	−.196
5	−.600	−.160	−.478	−.207	−.061	−.338	−.081	−.360
6	−.648	−.472	−.540	−.494	−.189	−.653	−.162	−.665
7	−.793	−.631	−.694	−.665	−.374	−1.023	−.265	−.962
8	−.583	−.195	−.465	−.231	−.195	−.314	−.081	−.360
9	−.674	−.014	−.538	−.113	−.239	−.302	−.081	−.360
10	−.744	−.310	−.595	−.374	−.384	−.546	−.172	−.669

Table VII. Calculated Harmonic Forces for MBB-A3 Airfoil

Case	Inviscid Real	Inviscid Imaginary	Viscous Real	Viscous Imaginary	Linear Real	Linear Imaginary
Lift-curve slope due to pitch, c_{l_α}
3	6.460	−5.352	6.757	−2.770	6.548	−1.581
4	4.362	−.954	4.539	−.783	5.220	−.054
5	4.791	2.136	4.709	1.998	5.424	1.998
Pitching-moment-curve slope due to pitch, c_{m_α}
3	−0.835	0.909	−0.376	−0.251	−0.058	−0.325
4	−.346	−.233	−.412	−.539	−.180	−.896
5	−.847	−1.686	−.754	−1.656	−1.082	−2.000
Lift-curve slope due to plunge, c_{l_h}
11	−1.173	−1.147	−0.687	−1.268	−0.220	−0.629
12	−1.135	−2.203	−1.032	−2.318	−.386	−1.368
13	.131	−6.690	.079	−6.532	−.128	−3.700
Pitching-moment-curve slope due to plunge, c_{m_h}
11	0.228	0.144	−0.013	0.069	−0.020	0.007
12	.092	.108	−.081	.178	−.136	.068
13	−1.011	1.156	−1.060	1.061	−.592	.780

Table VIII. NACA 0012 Airfoil Harmonic Forces

Case	Inviscid Real	Inviscid Imaginary	Viscous Real	Viscous Imaginary	Experiment Real	Experiment Imaginary	Linear Real	Linear Imaginary
Lift-curve slope due to pitch, c_{l_α}
1	6.531	−1.055	5.858	−0.801	6.797	−1.306	6.273	−0.938
2	6.638	−1.111			6.616	−.891	6.266	−.932
3	6.845	−1.235			6.372	−.803	6.266	−.932
5	7.838	−3.031	6.875	−1.999	7.896	−3.217	6.863	−1.619
Pitching-moment-curve slope due to pitch, c_{m_α}
1	0.004	−0.198	0.122	−0.191	0.207	−0.232	−0.010	−0.185
2	.059	−.223			.224	−.244	−.010	−.185
3	.174	−.272			.303	−.287	−.010	−.185
5	−.153	−.317	.110	−.354	−.090	−.262	−.042	−.261

NACA 64A006

NACA 64A010A

MBB-A3

NACA 0012

Figure 1. Airfoil sections studied.
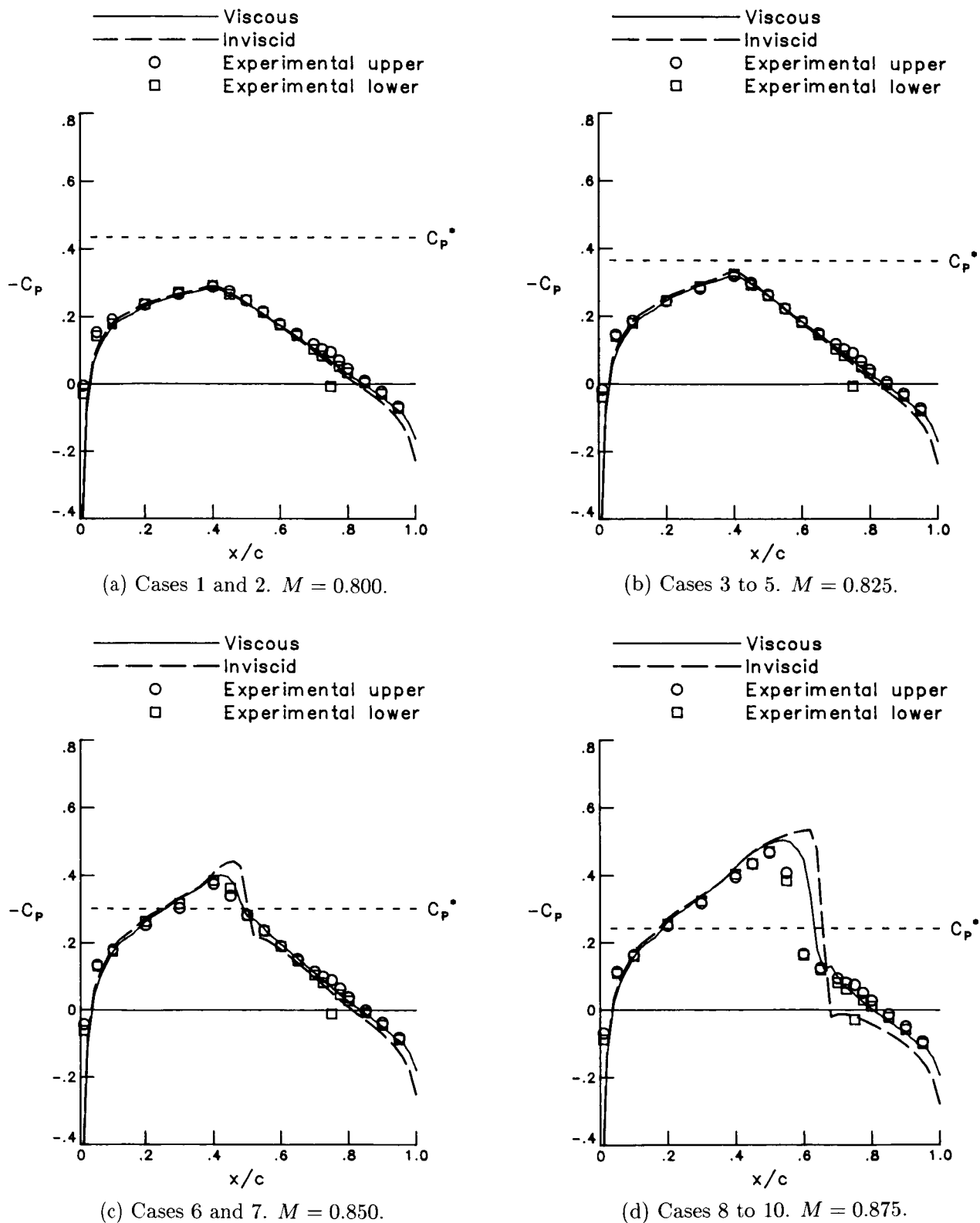
Figure 2. Steady pressure distribution for cases 1 to 12 for NACA 64A006 airfoil. $\alpha_m = 0°$; $N_{Re} = 2.3 \times 10^6$.
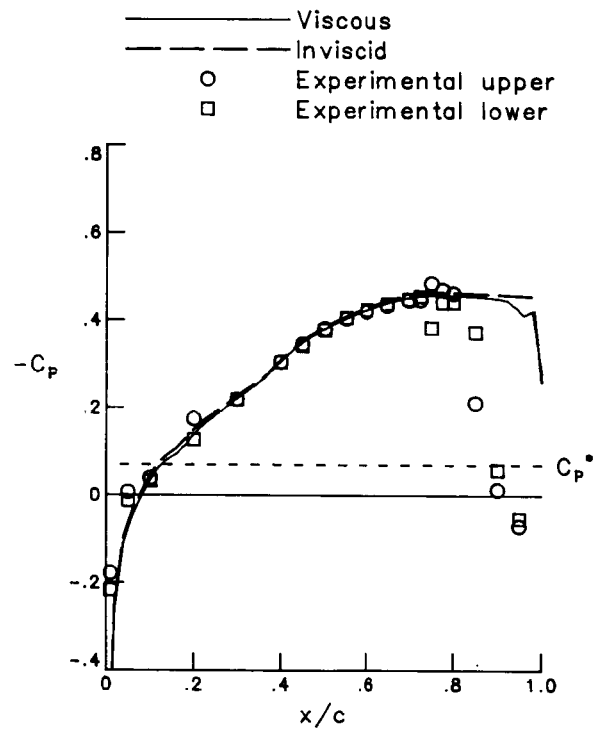
(e) Cases 11 and 12. $M = 0.960$.

Figure 2. Concluded.
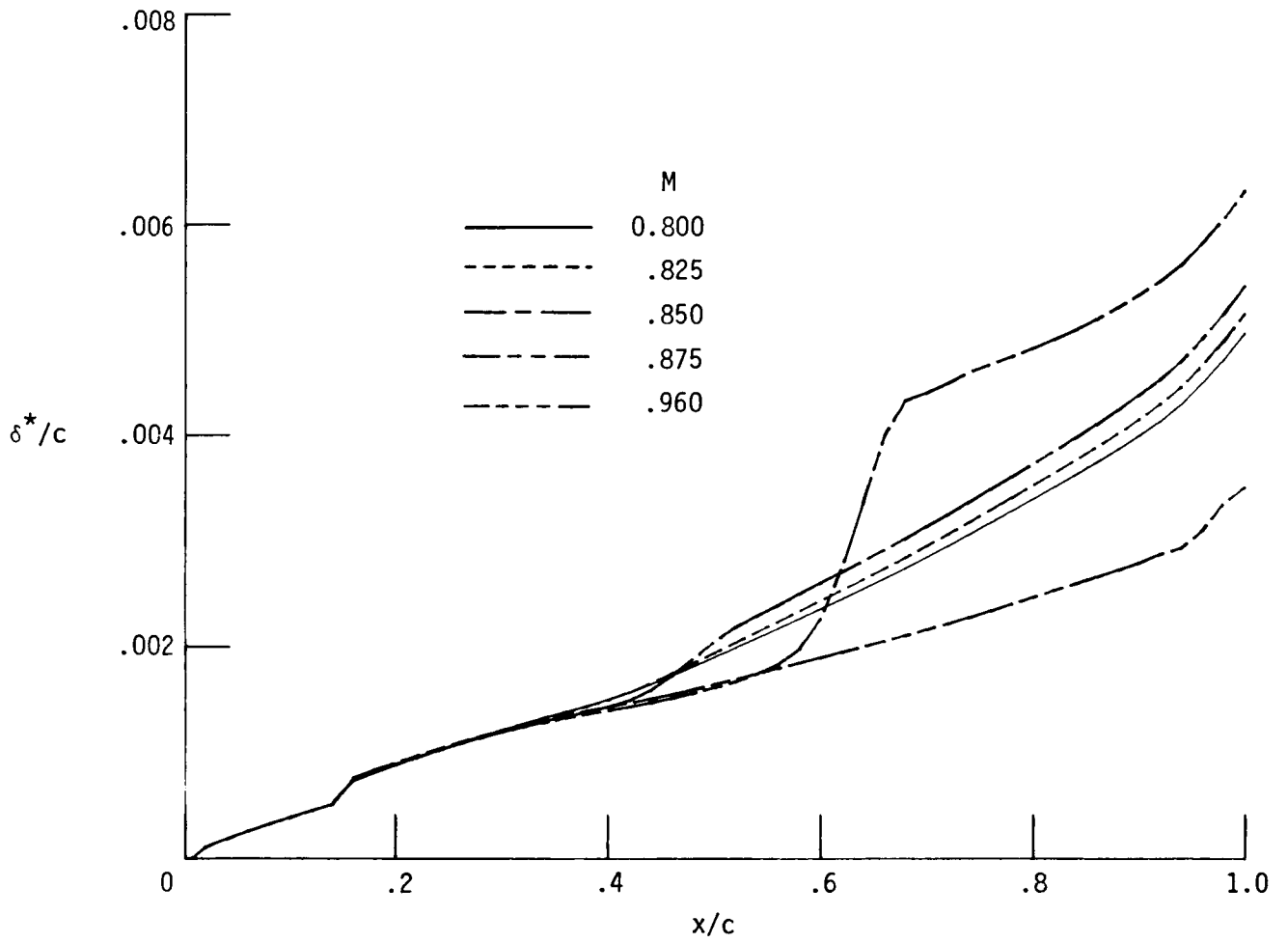
Figure 3. Effect of Mach number on boundary-layer displacement thickness for NACA 64A006 airfoil.
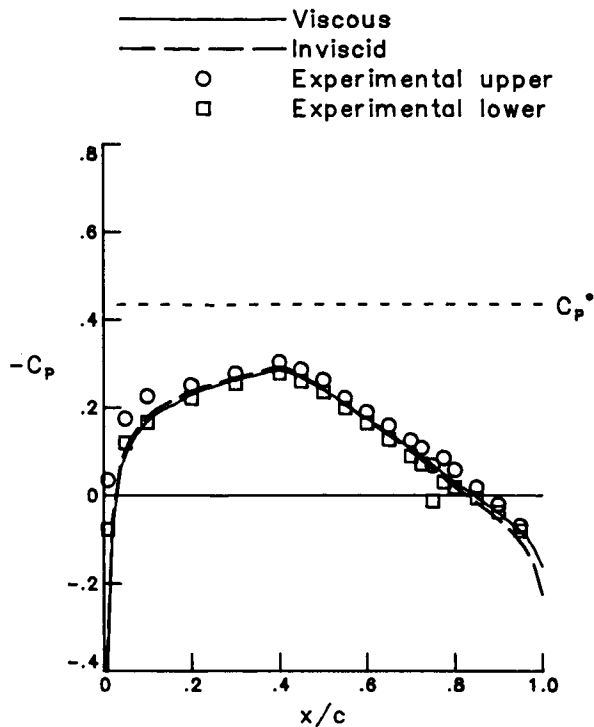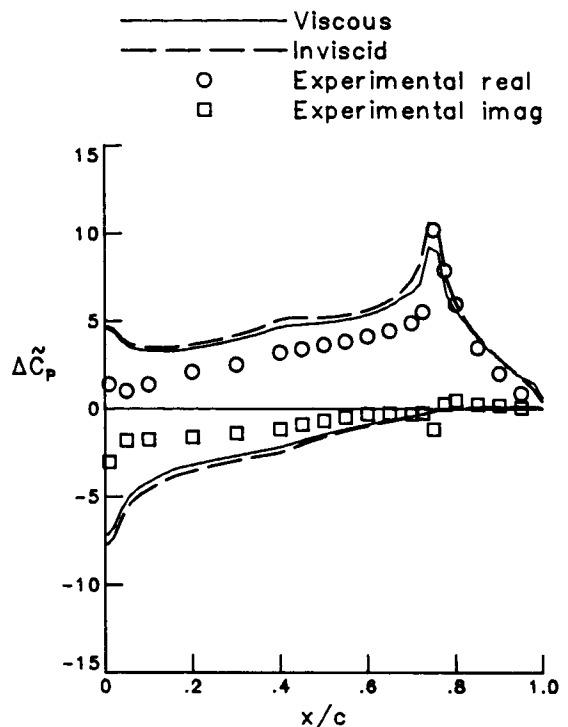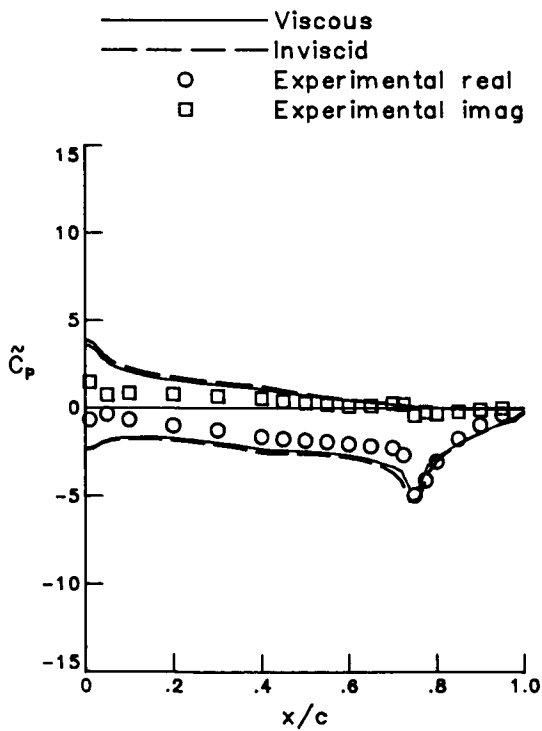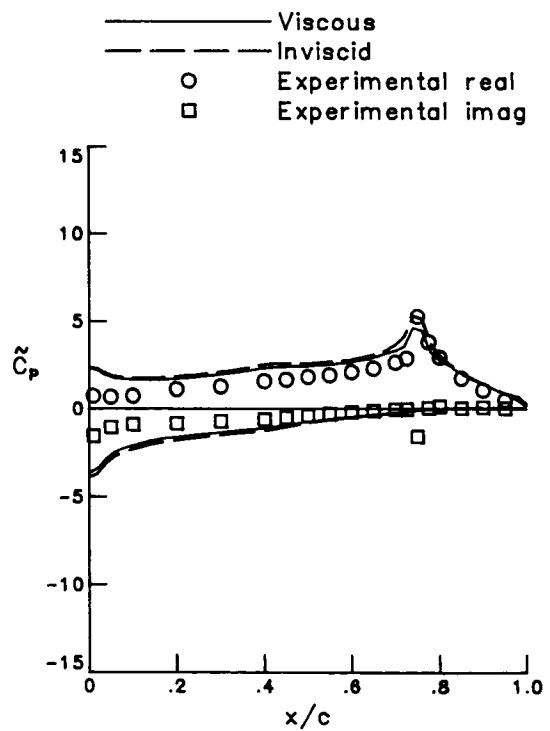
Figure 4. Unsteady pressure distribution for case 1 for NACA 64A006 airfoil. $M = 0.800; \beta_o = 1°; k = 0.064.$
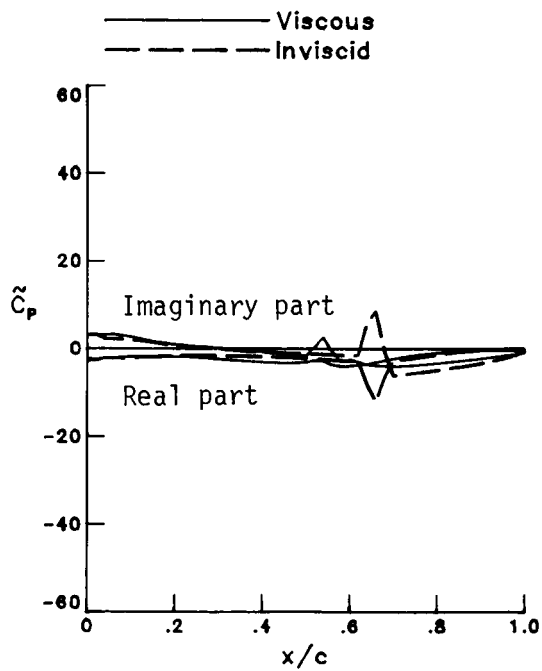
(a) Mean.

(b) Lifting.

(c) Upper surface.
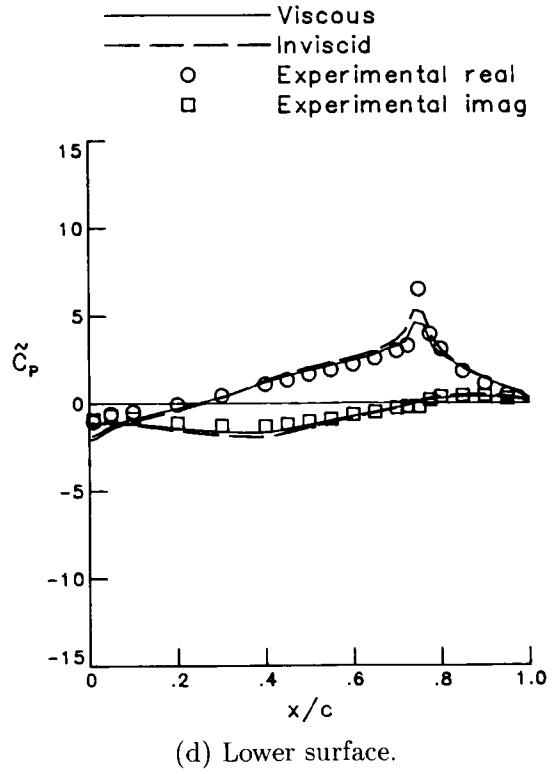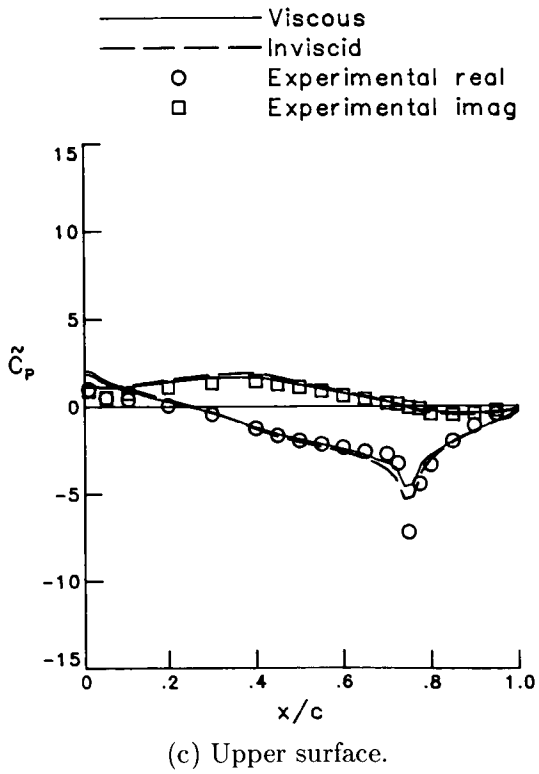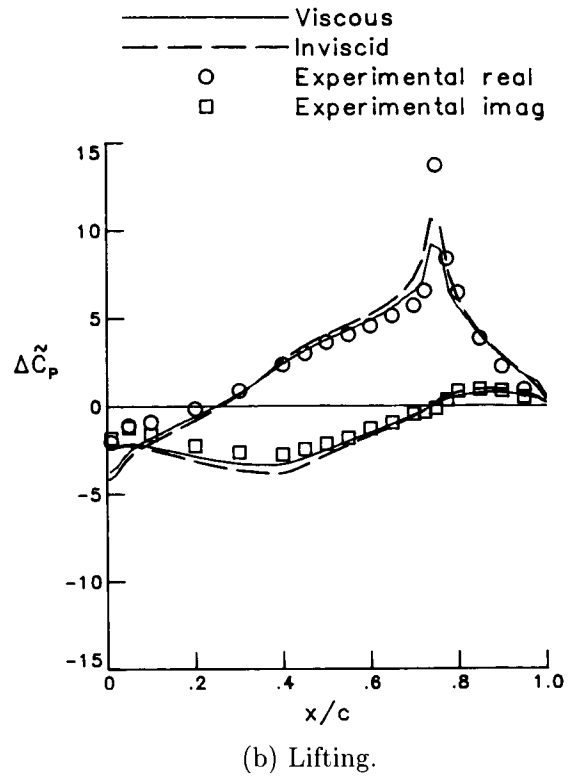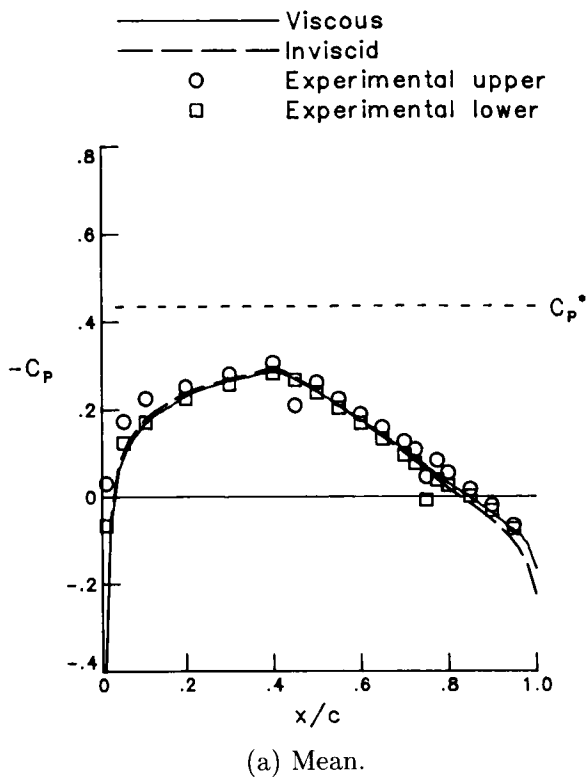
(d) Lower surface.

Figure 5. Unsteady pressure distribution for case 2 for NACA 64A006 airfoil. $M = 0.800; \beta_o = 1°; k = 0.254.$
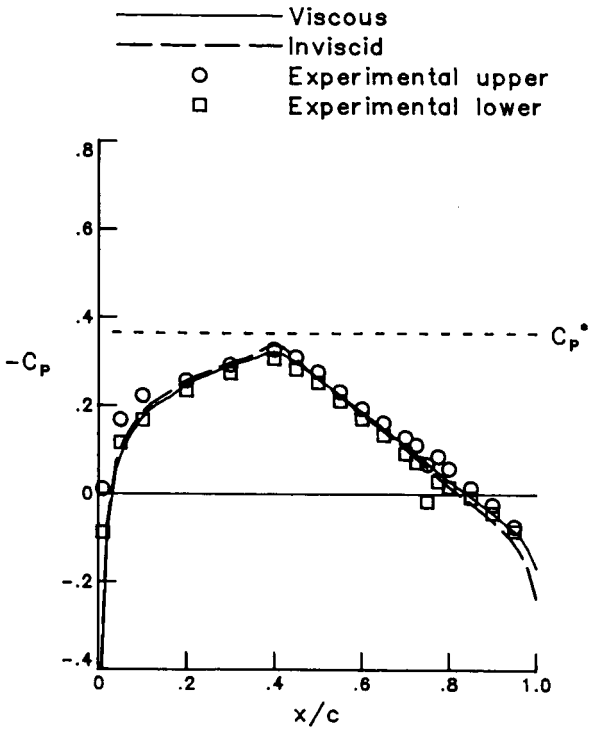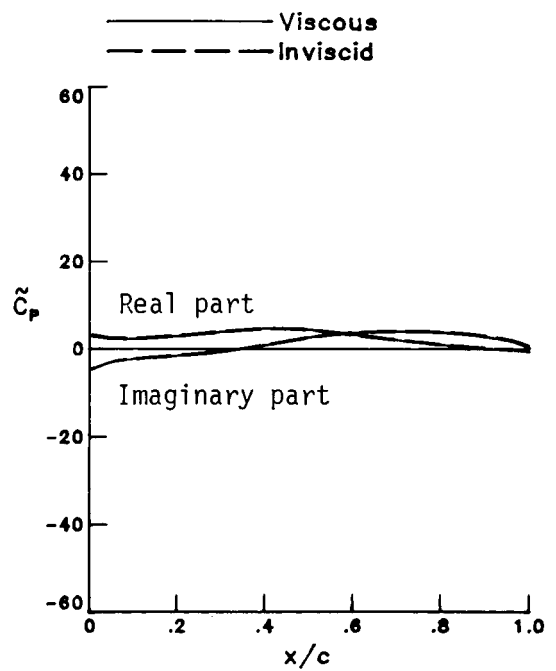
(a) Mean.
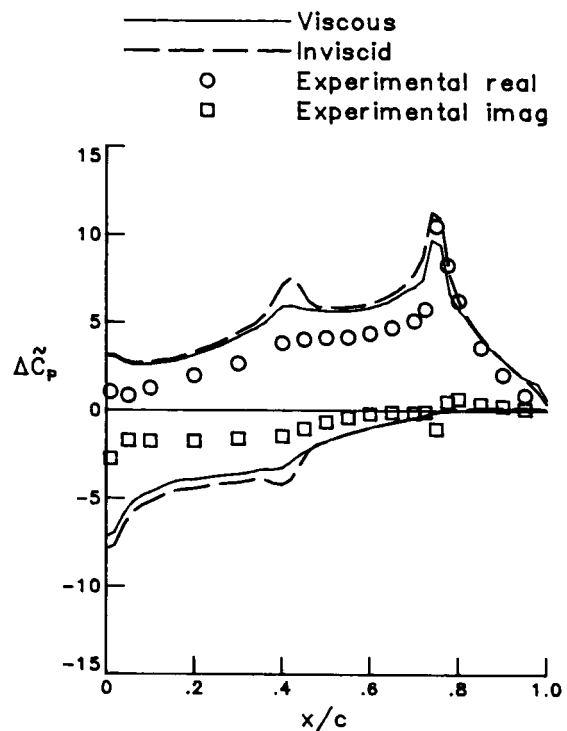
(b) Lifting.
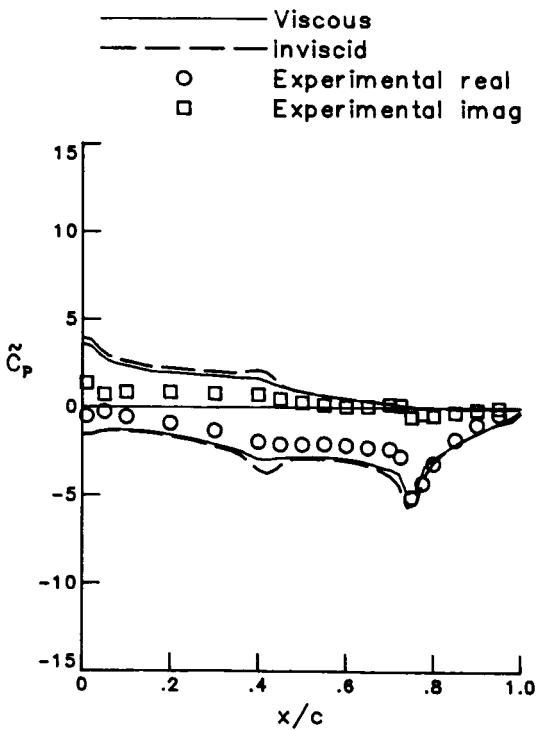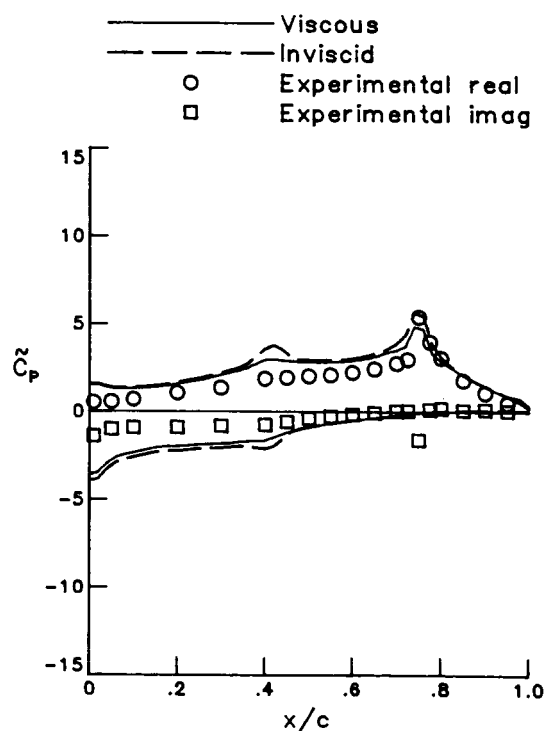
(c) Upper surface.

(d) Lower surface.

Figure 6. Unsteady pressure distribution for case 3 for NACA 64A006 airfoil. $M = 0.825; \beta_o = 1°; k = 0.062$.
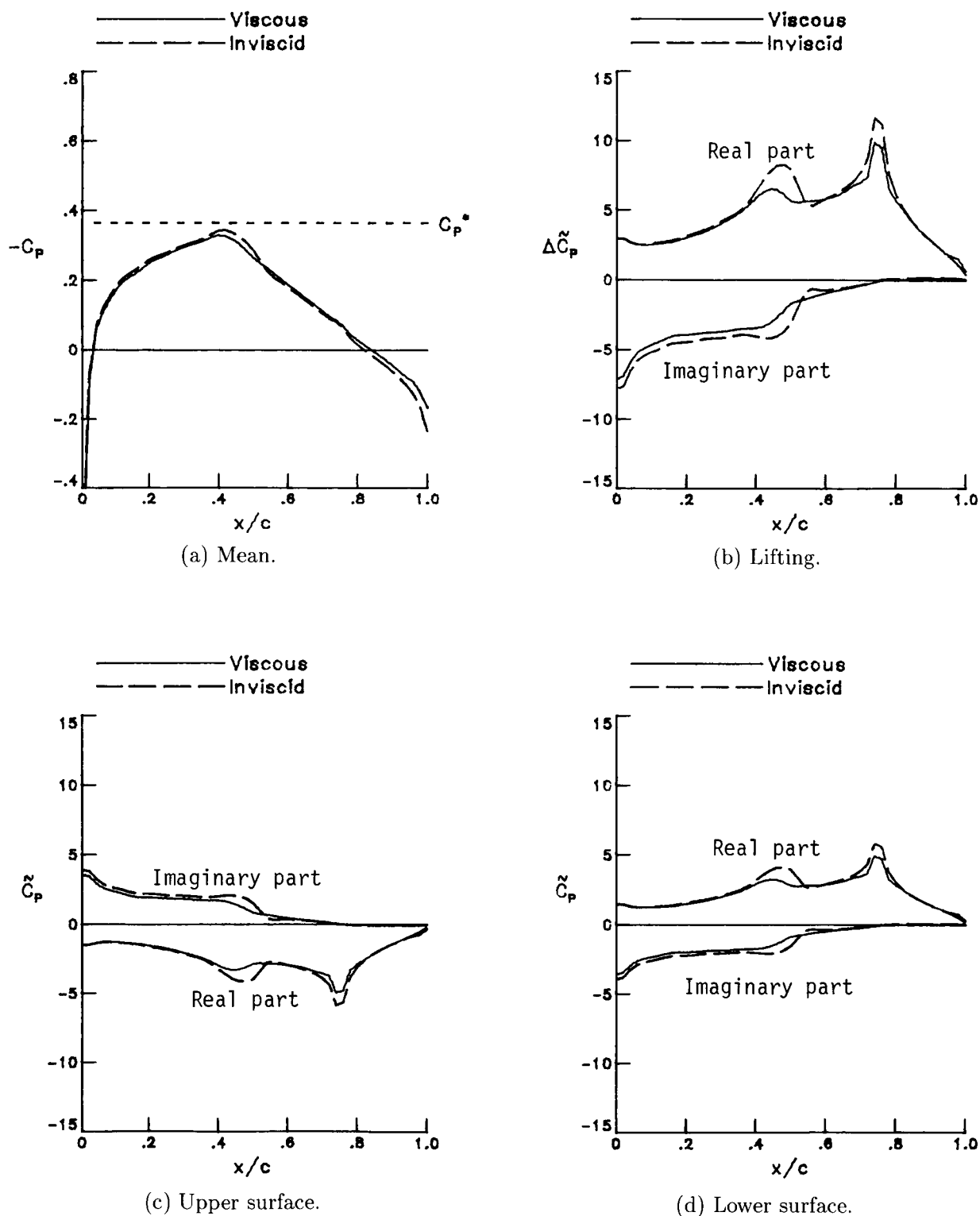
Figure 7. Unsteady pressure distribution for case 4 for NACA 64A006 airfoil. $M = 0.825$; $\beta_o = 2°$; $k = 0.062$.
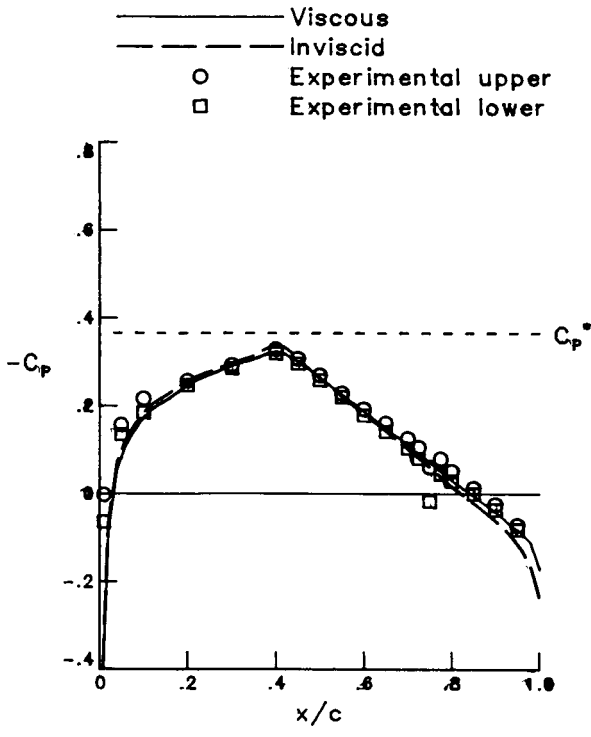
(a) Mean.
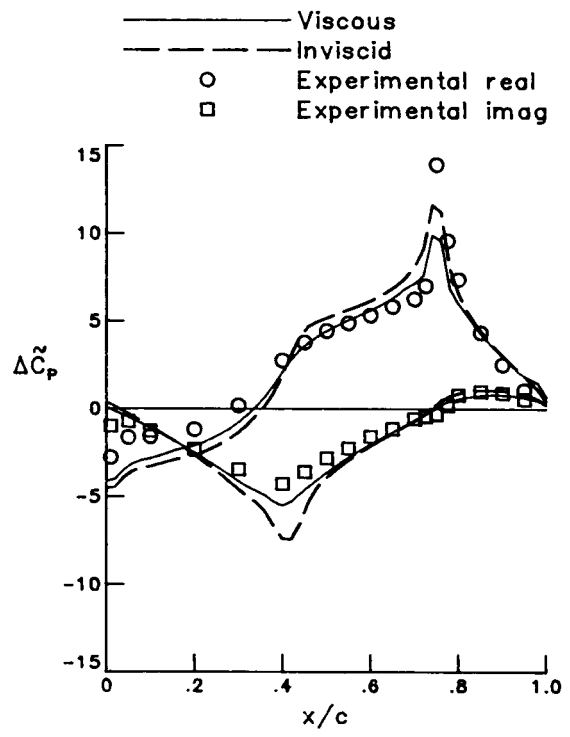
(b) Lifting.
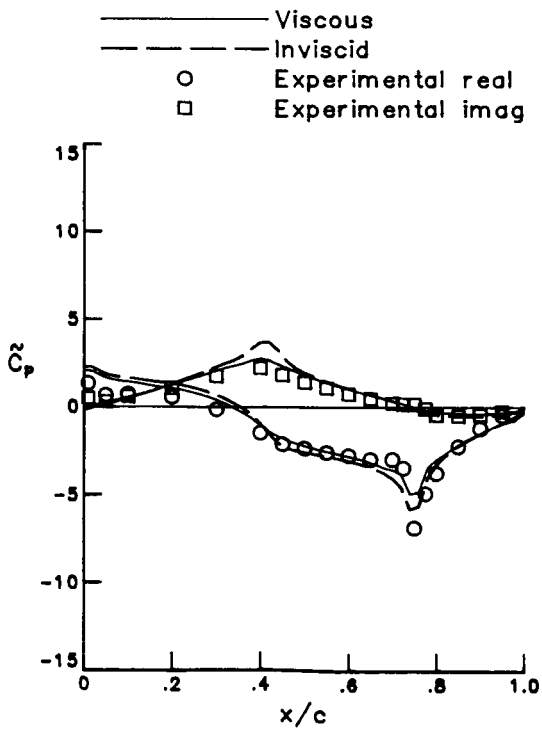
(c) Upper surface.
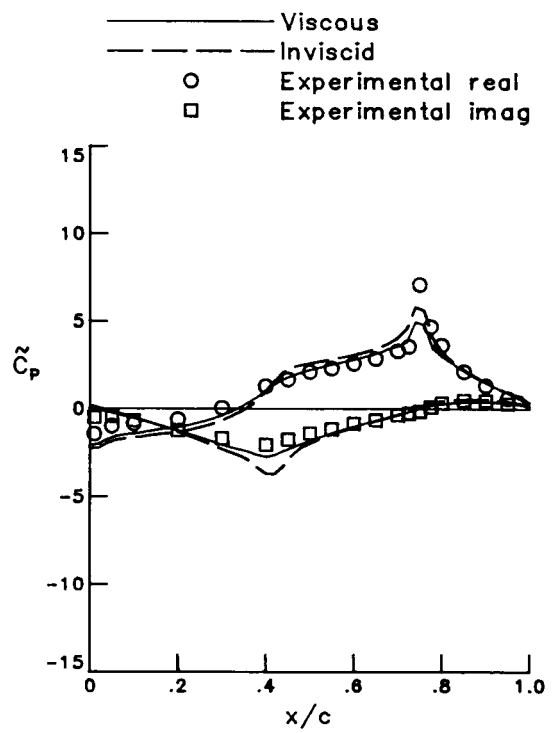
(d) Lower surface.

Figure 8. Unsteady pressure distribution for case 5 for NACA 64A006 airfoil. $M = 0.825; \beta_o = 1°; k = 0.248$.
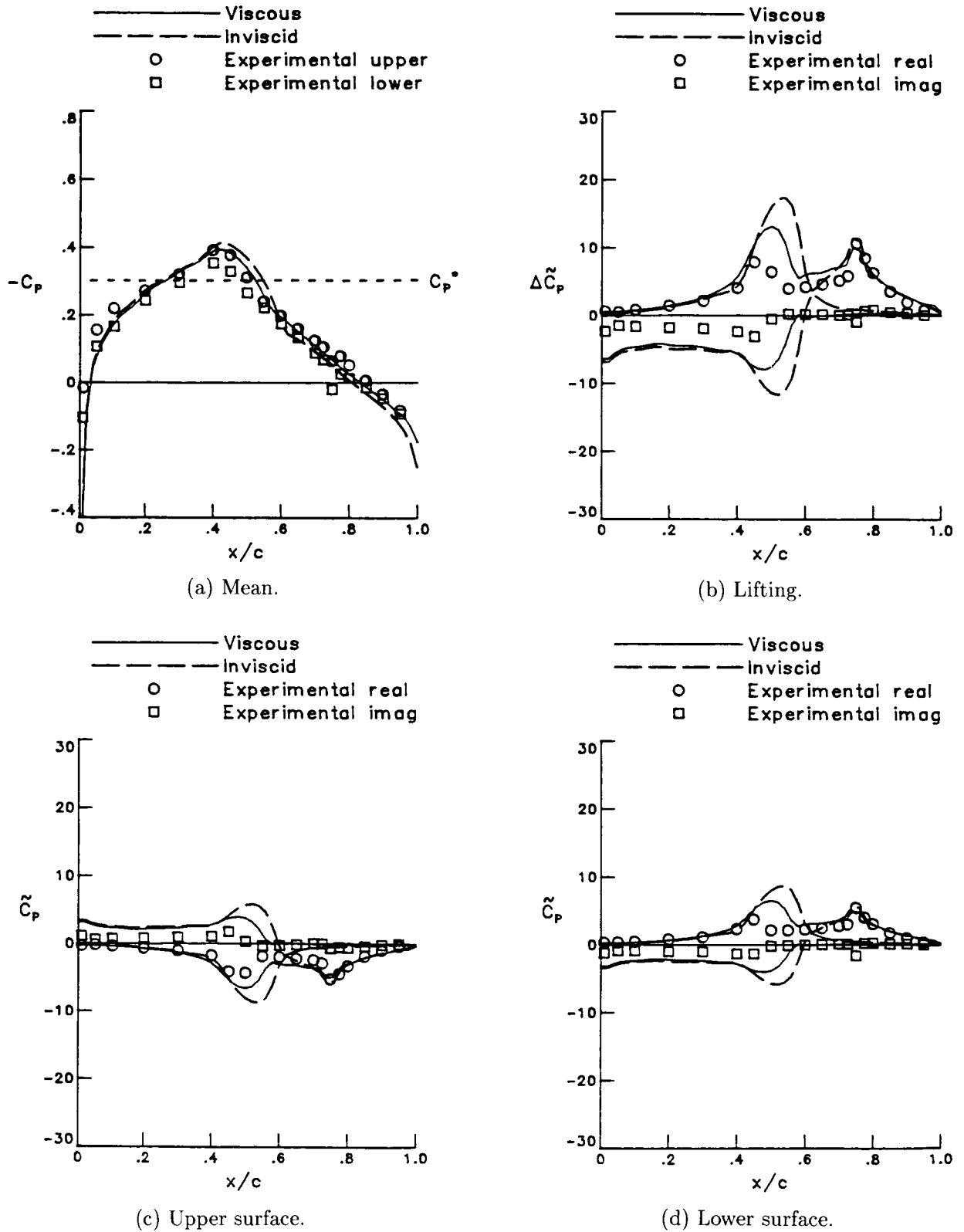
Figure 9. Unsteady pressure distribution for case 6 for NACA 64A006 airfoil. $M = 0.850; \beta_o = 1°; k = 0.060$.
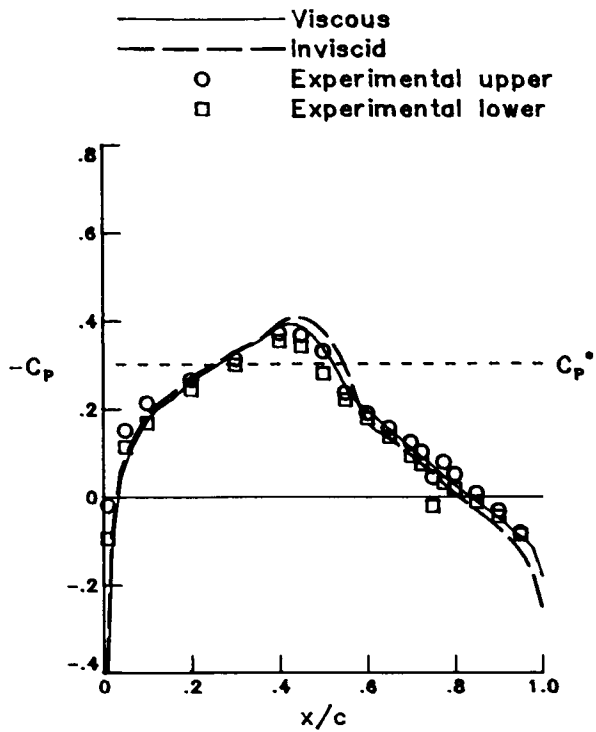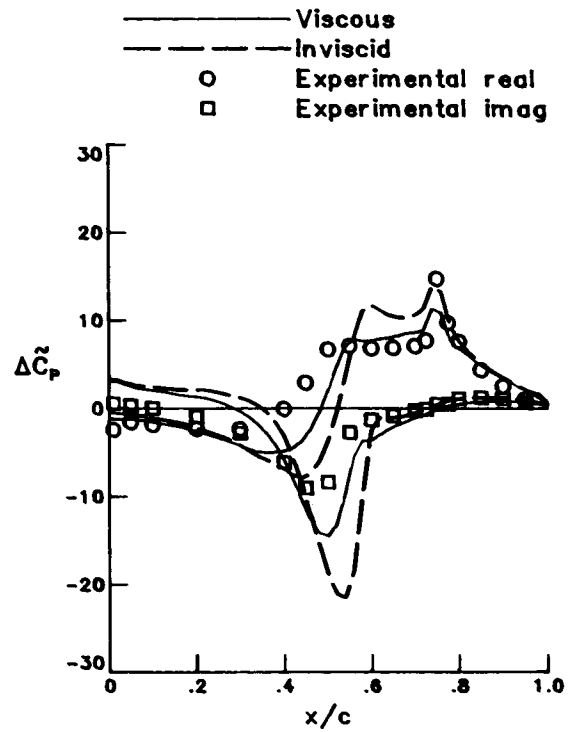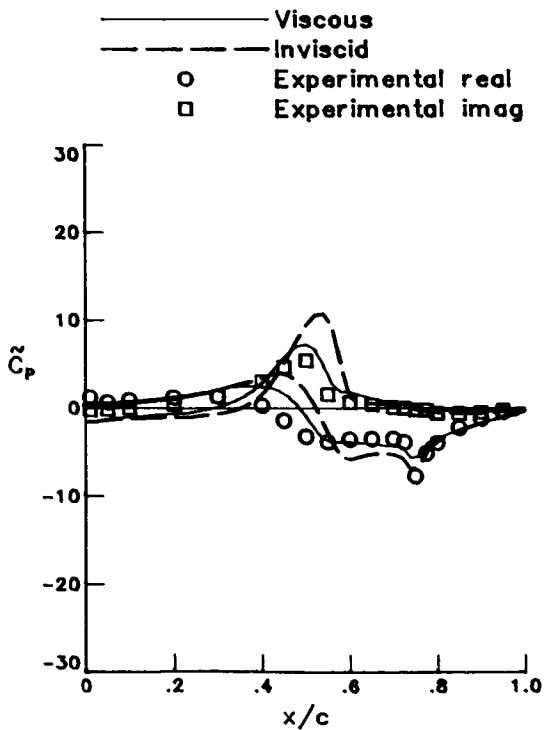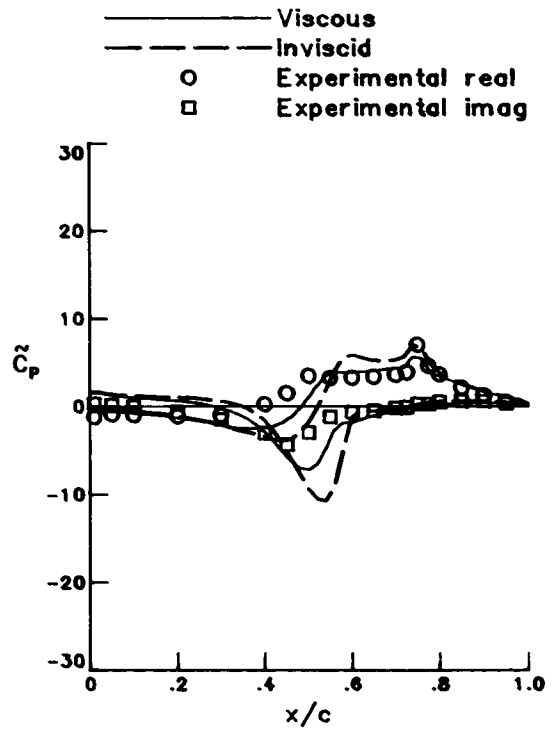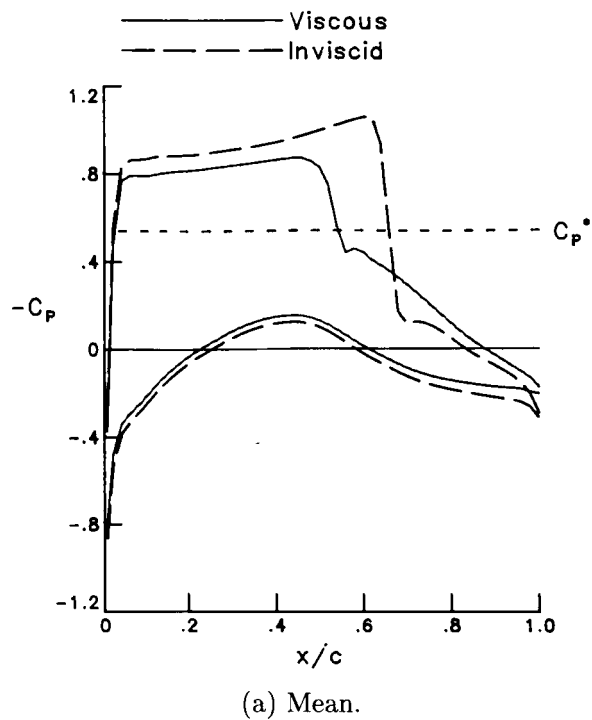
Figure 10. Unsteady pressure distribution for case 7 for NACA 64A006 airfoil. $M = 0.850; \beta_o = 1°; k = 0.242.$
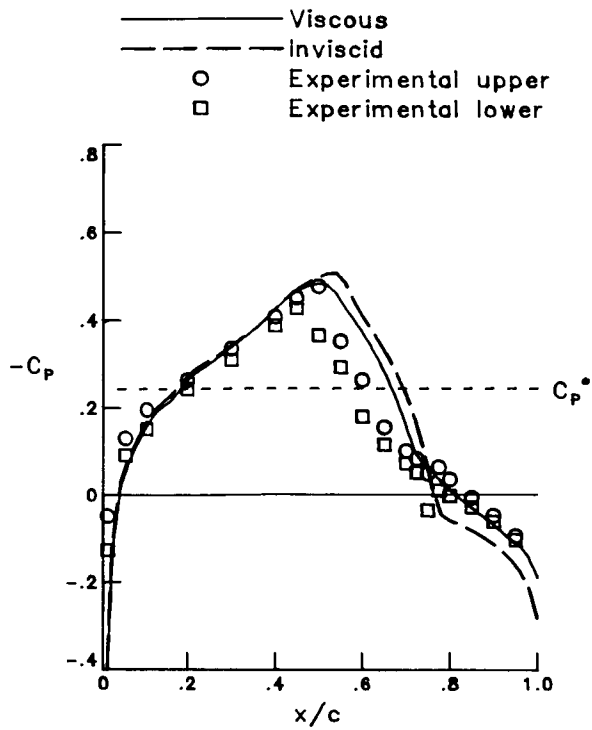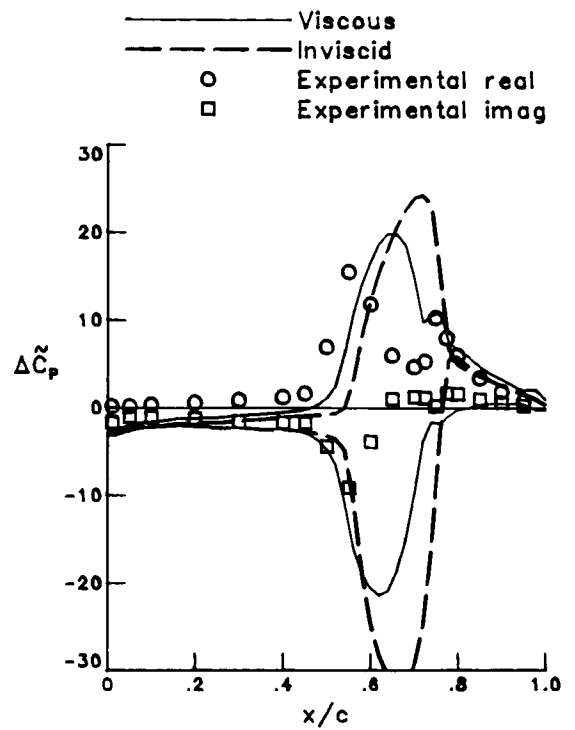
(a) Mean.

(b) Lifting.
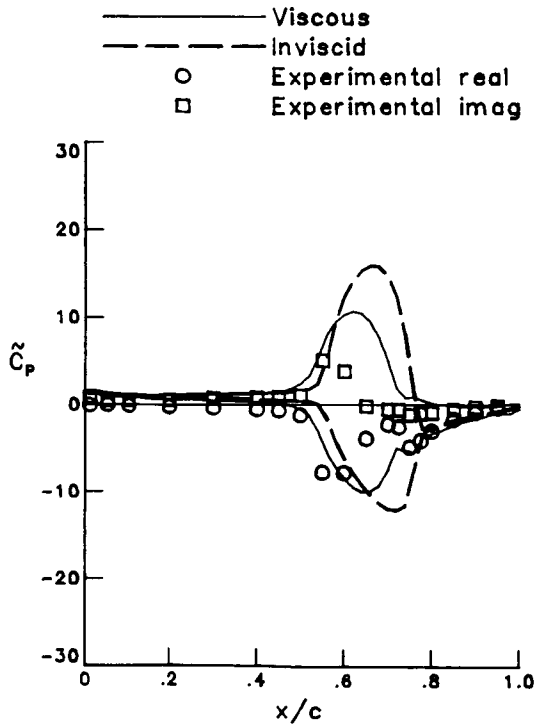
(c) Upper surface.
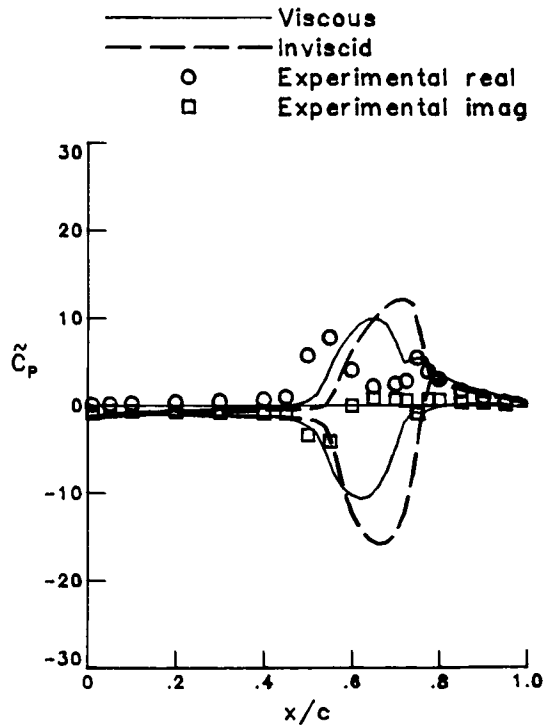
(d) Lower surface.

Figure 11. Unsteady pressure distribution for case 8 for NACA 64A006 airfoil. $M = 0.875$; $\beta_o = 1°$; $k = 0.059$.
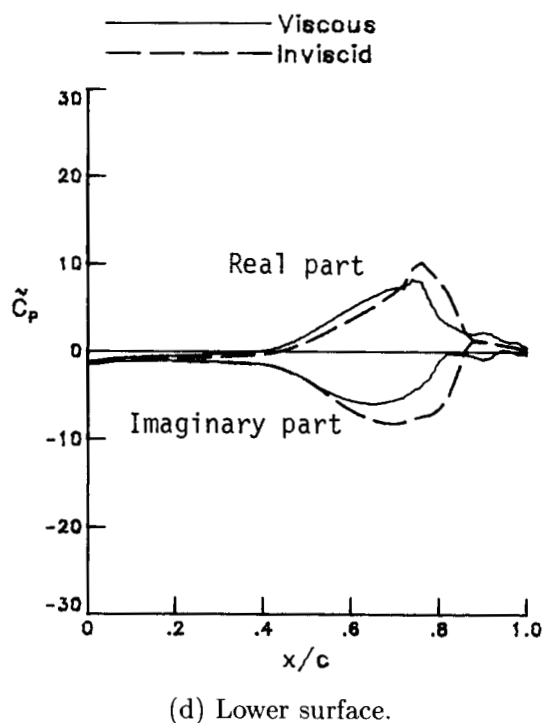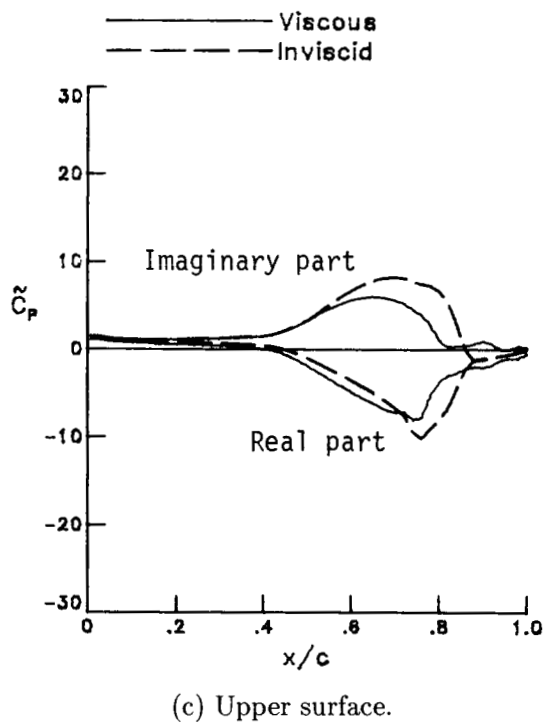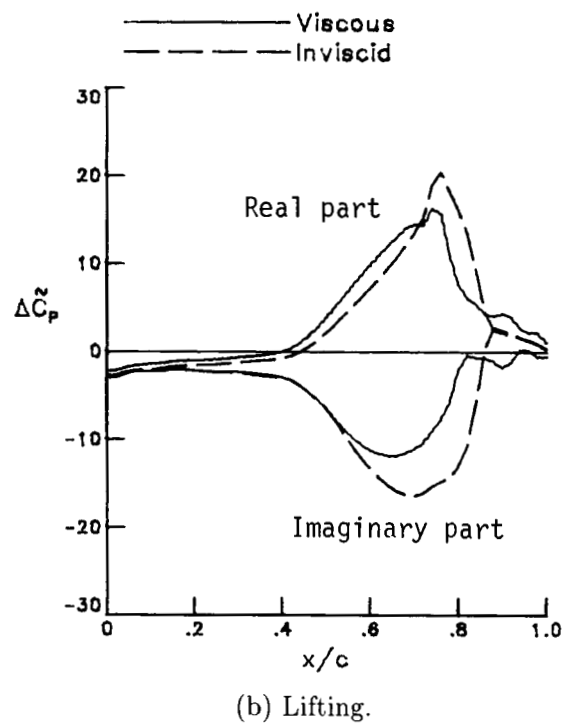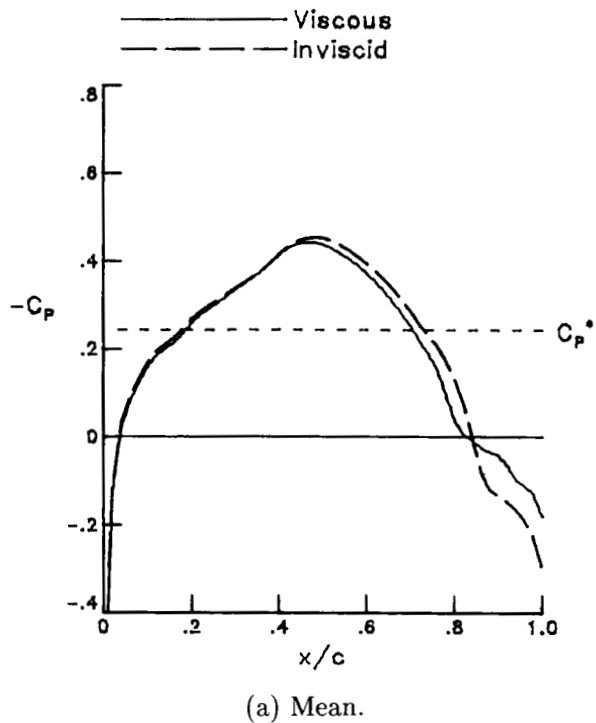
Figure 12. Unsteady pressure distribution for case 9 for NACA 64A006 airfoil. $M = 0.875$; $\beta_o = 2°$; $k = 0.059$.
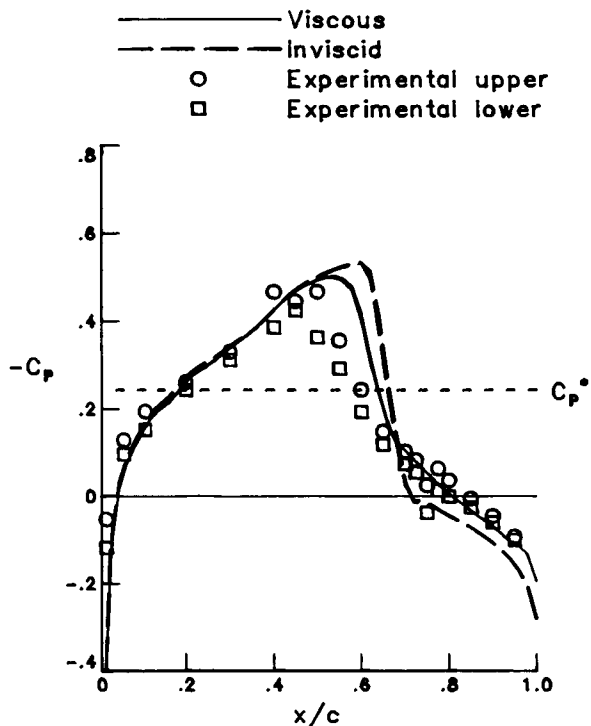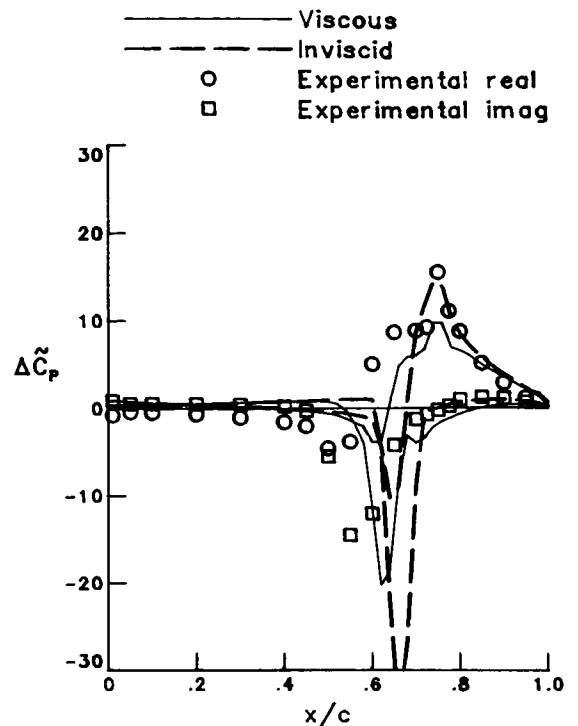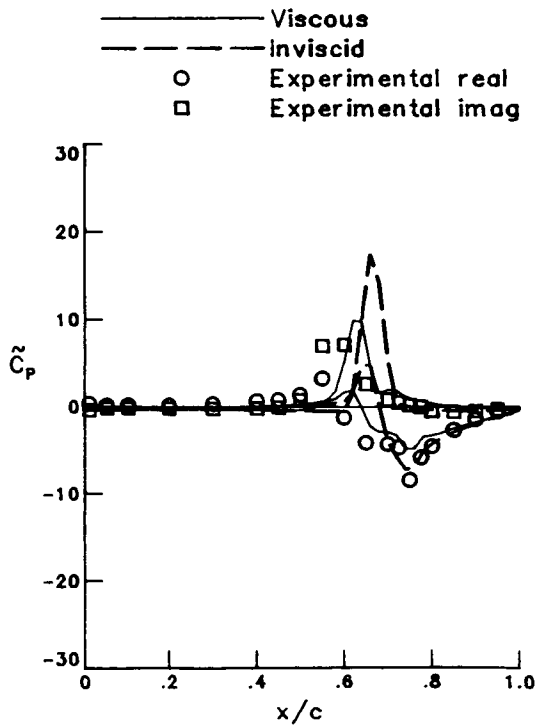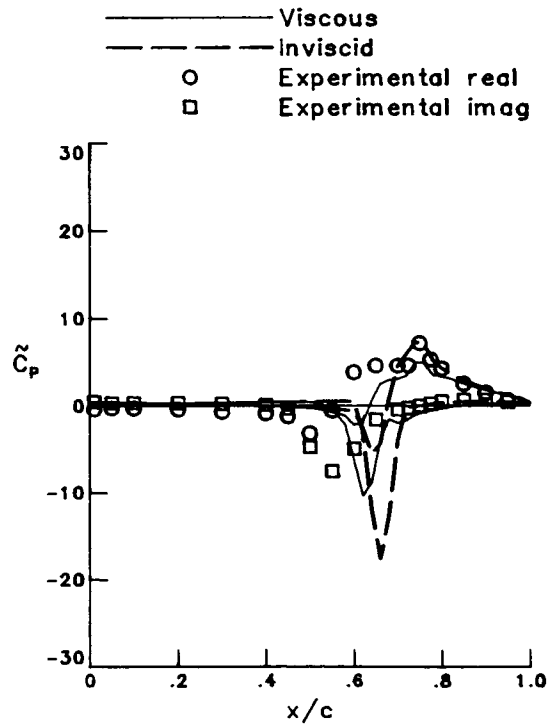
Figure 13. Unsteady pressure distribution for case 10 for NACA 64A006 airfoil. $M = 0.875$; $\beta_o = 1°$; $k = 0.235$.
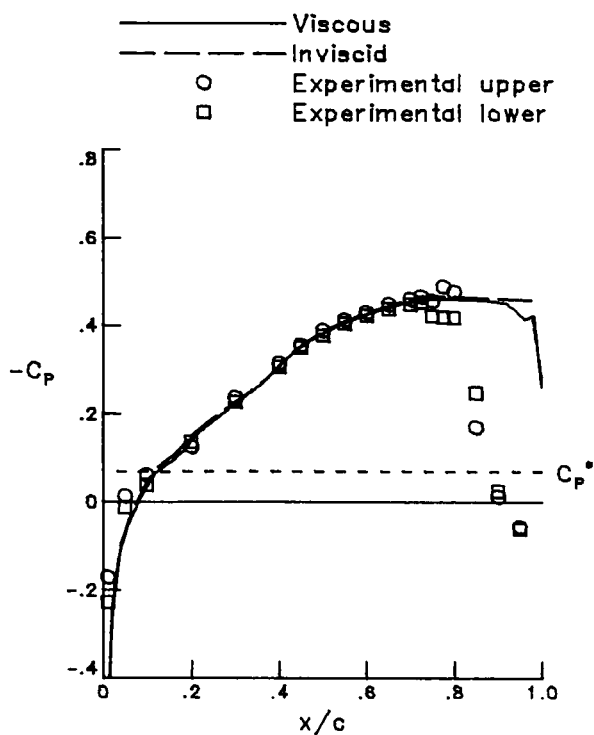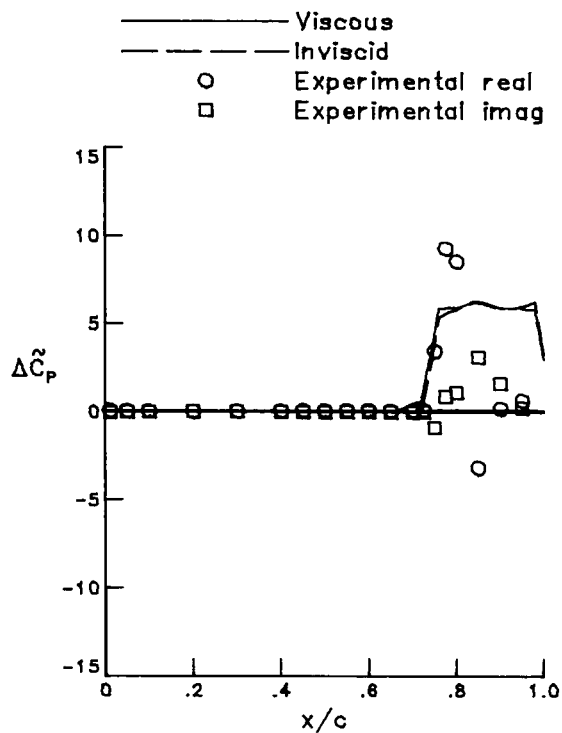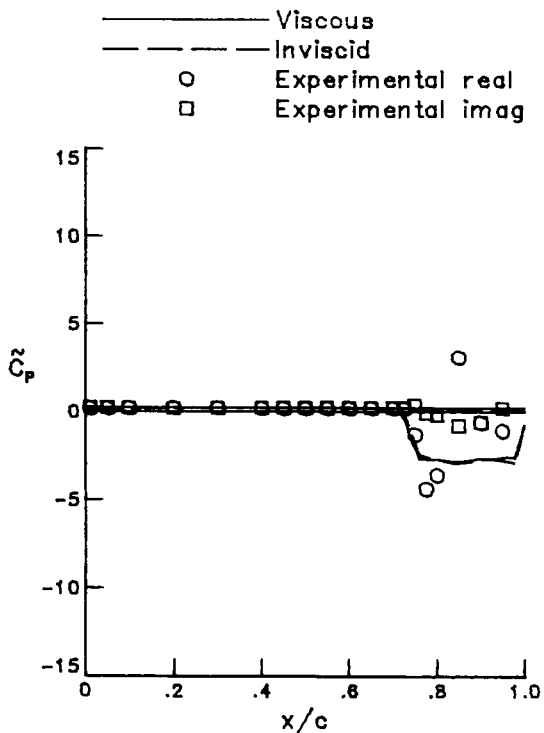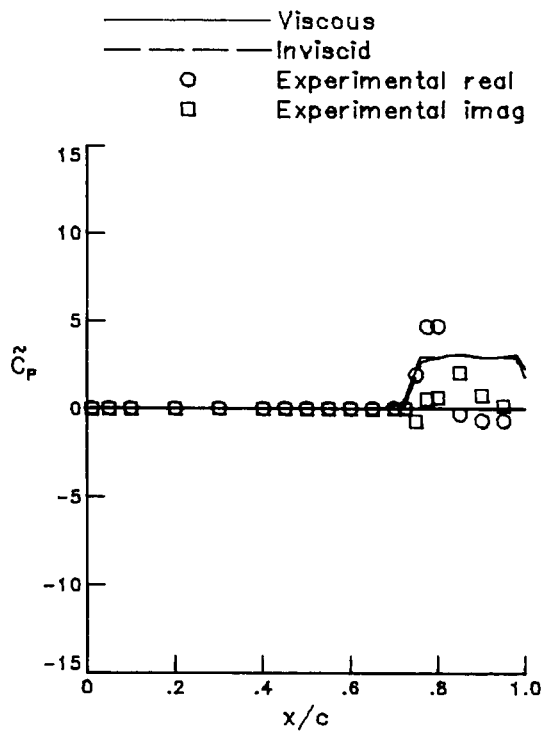
Figure 14. Unsteady pressure distribution for case 11 for NACA 64A006 airfoil. $M = 0.960$; $\beta_o = 1°$; $k = 0.054$.
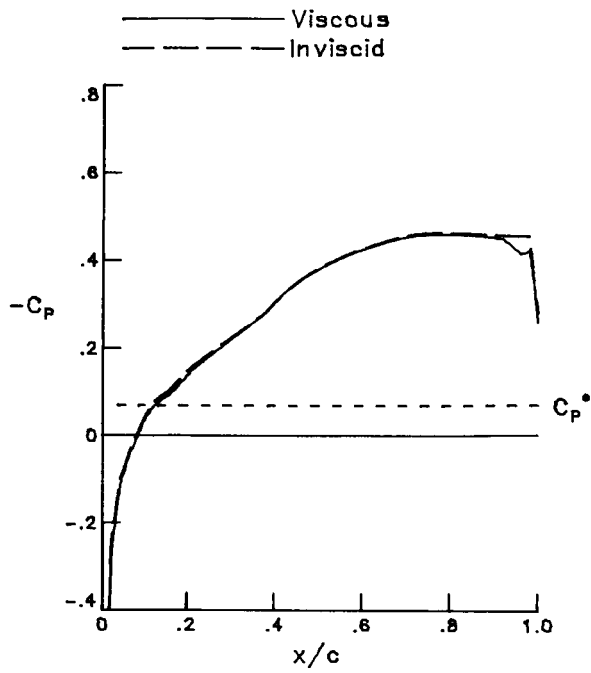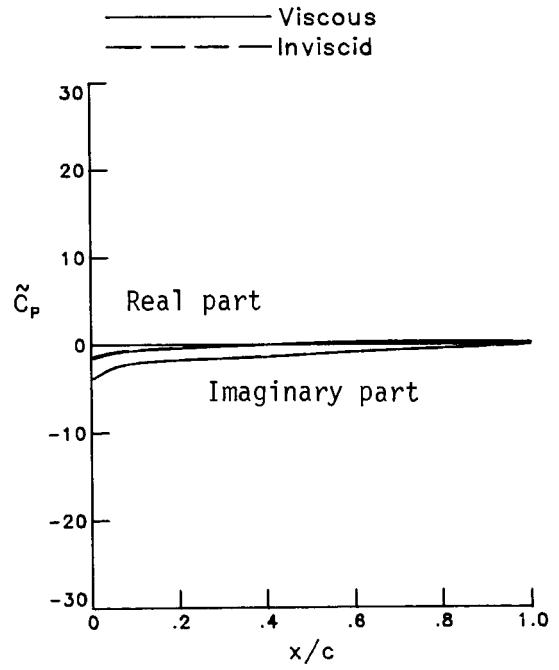
(a) Mean.
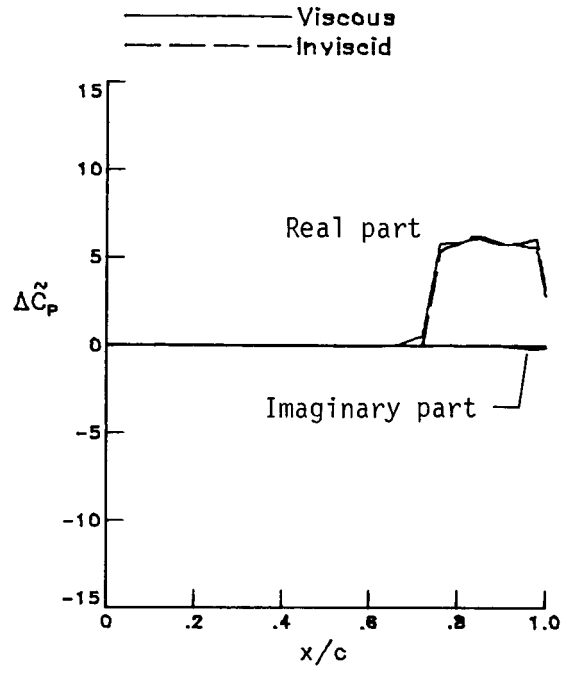
(b) Lifting.
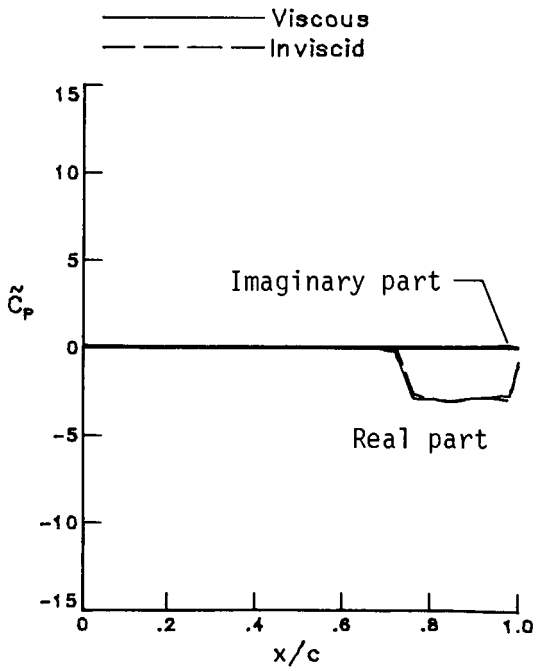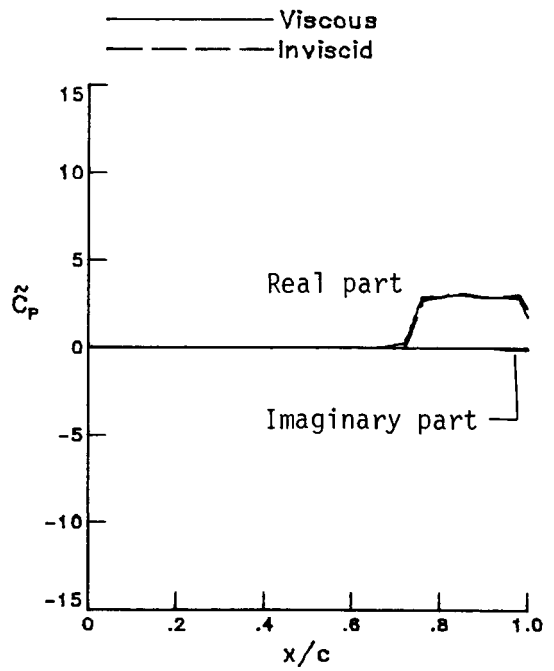
(c) Upper surface.

(d) Lower surface.
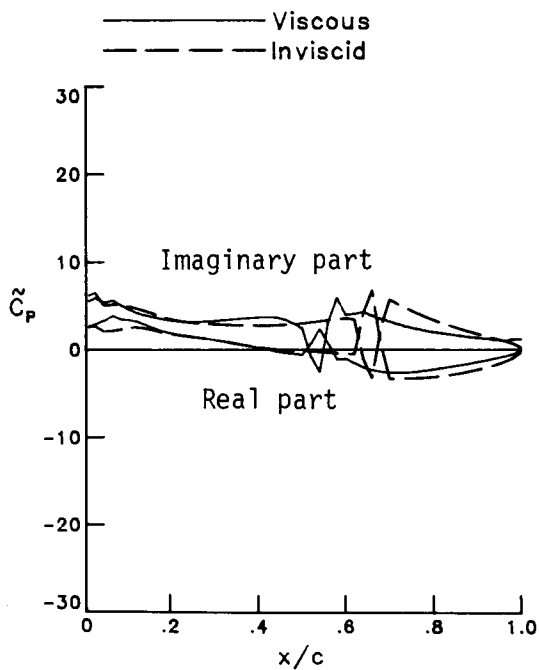
Figure 15. Unsteady pressure distribution for case 12 for NACA 64A006 airfoil. $M = 0.960; \beta_o = 1°; k = 0.217.$
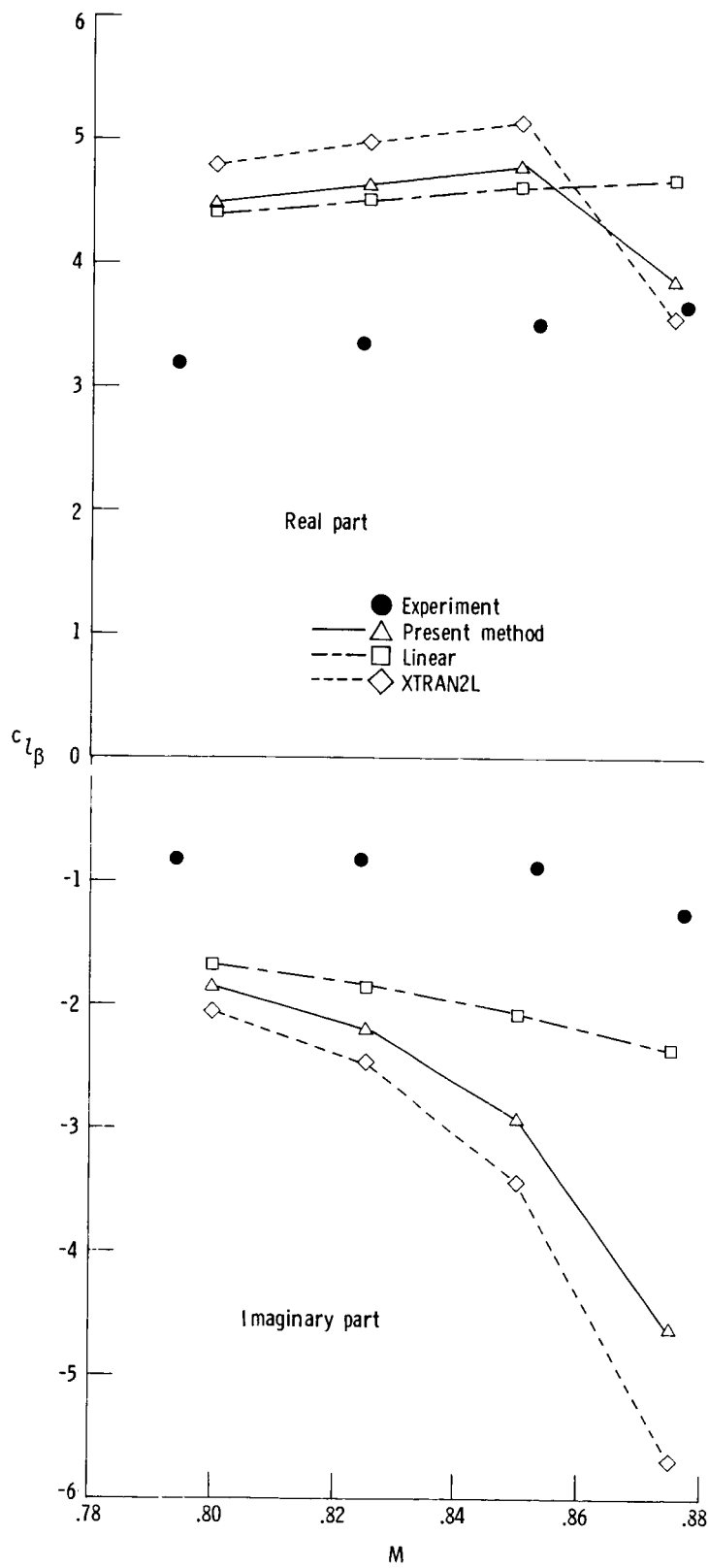
(a) Unsteady lift.

Figure 16. Comparison of unsteady forces for NACA 64A006 airfoil with $k = 0.06$. $\beta_o = 1°$.
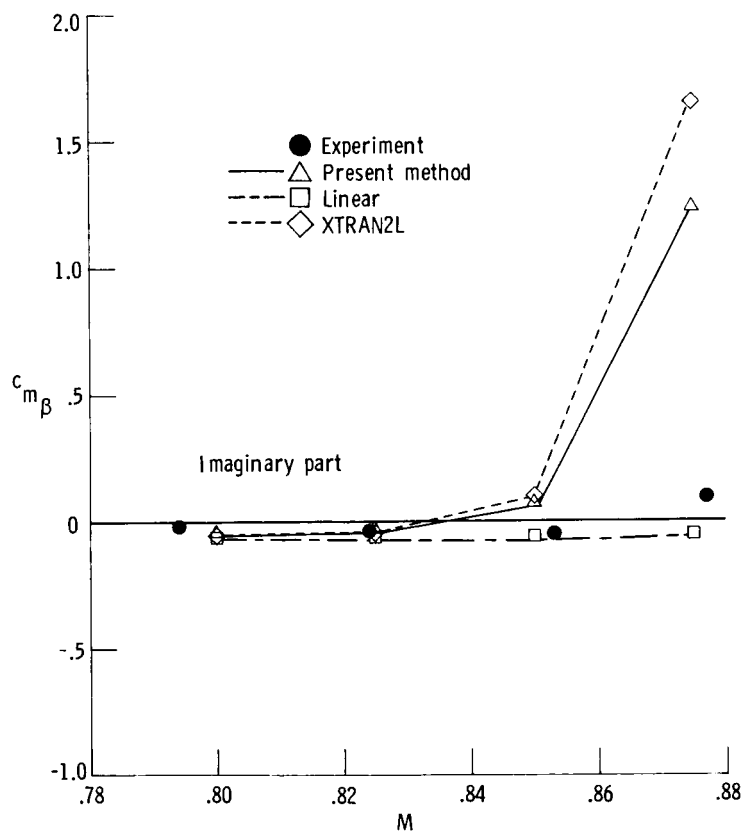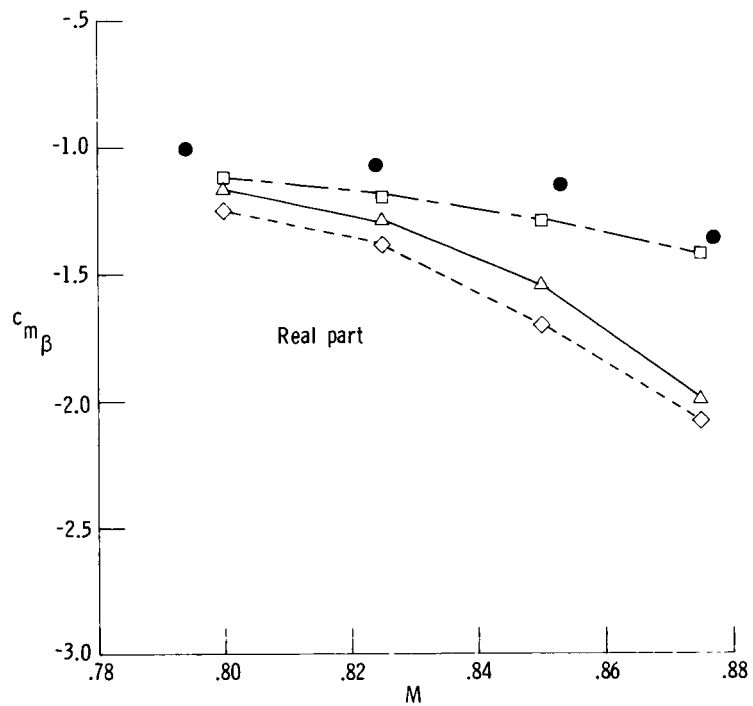
(b) Unsteady pitching moment.

Figure 16. Continued.
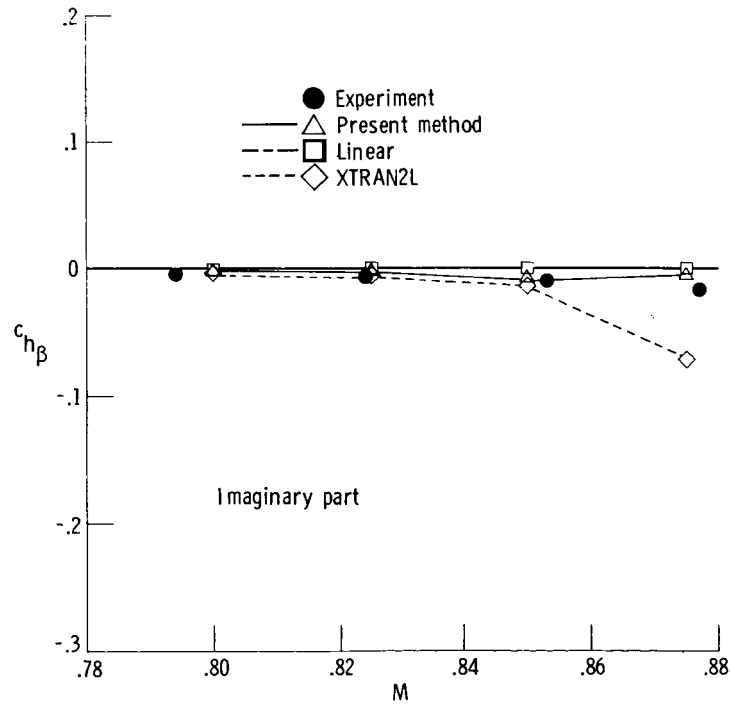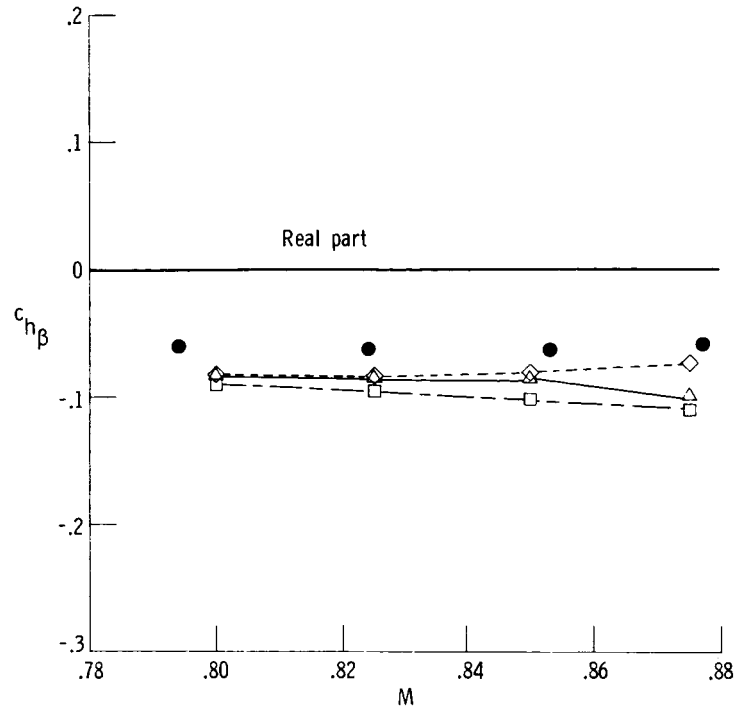
(c) Unsteady hinge moment.

Figure 16. Concluded.
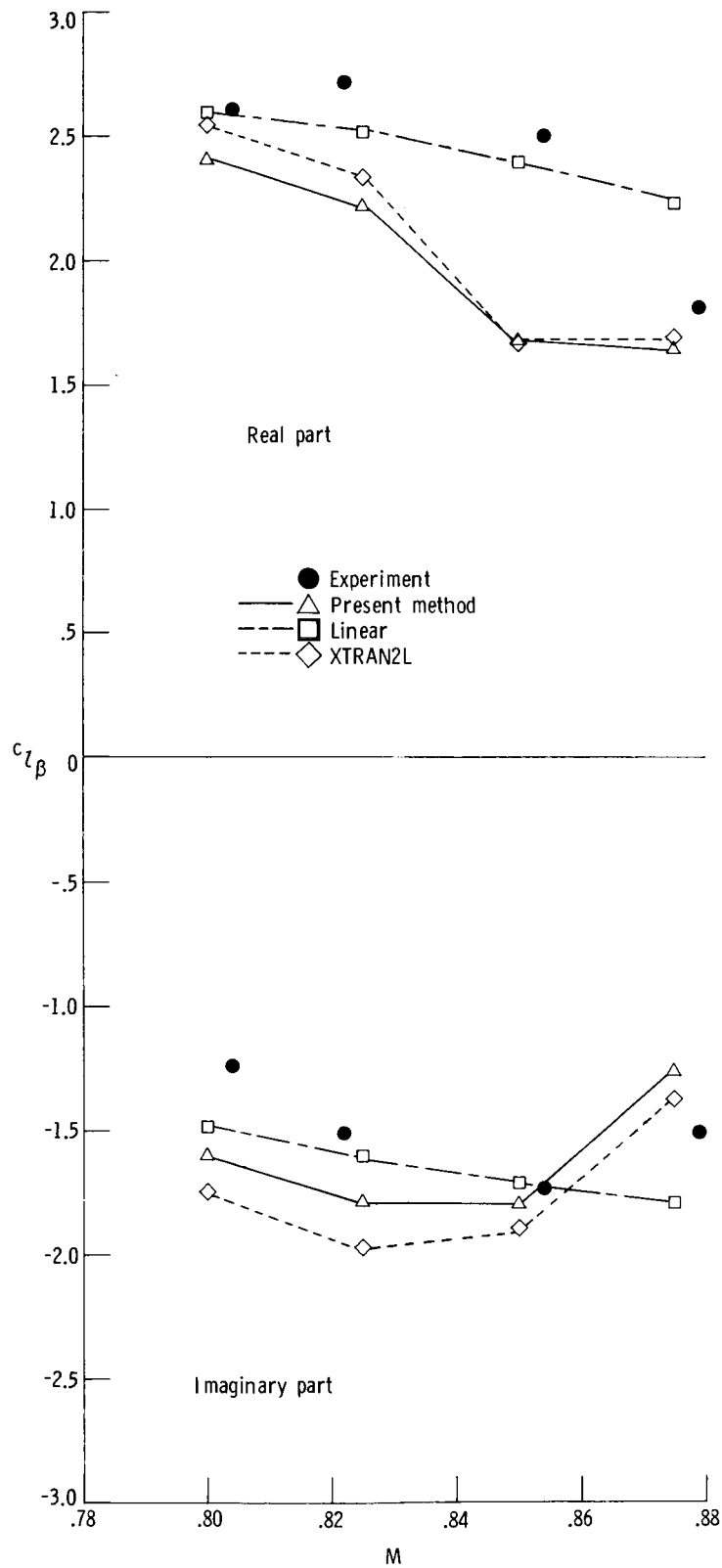
(a) Unsteady lift.

Figure 17. Comparison of unsteady forces for NACA 64A006 airfoil with $k = 0.24$. $\beta_o = 1°$.
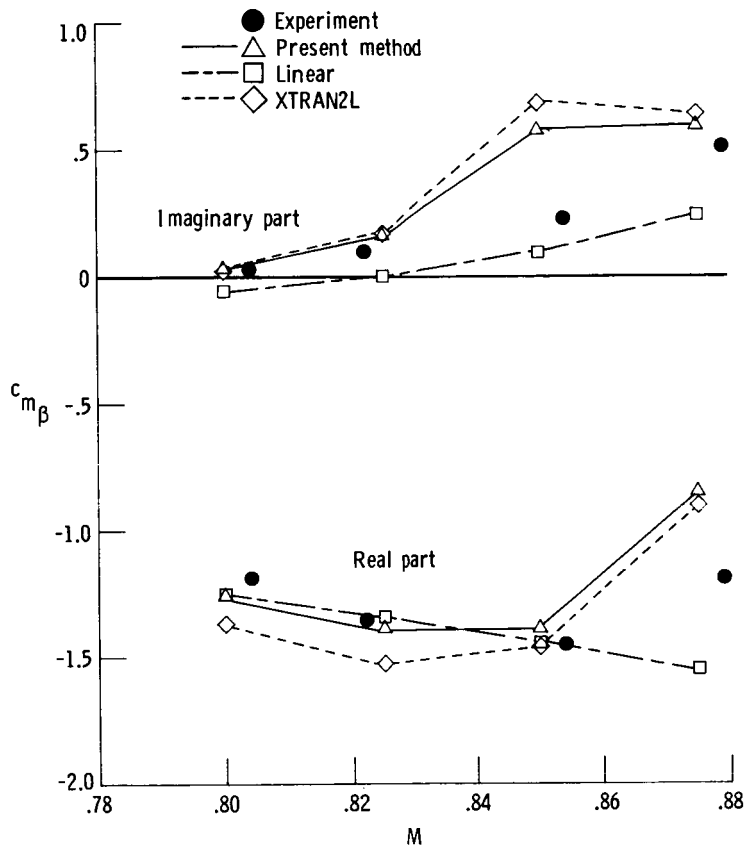
(b) Unsteady pitching moment.

Figure 17. Continued.
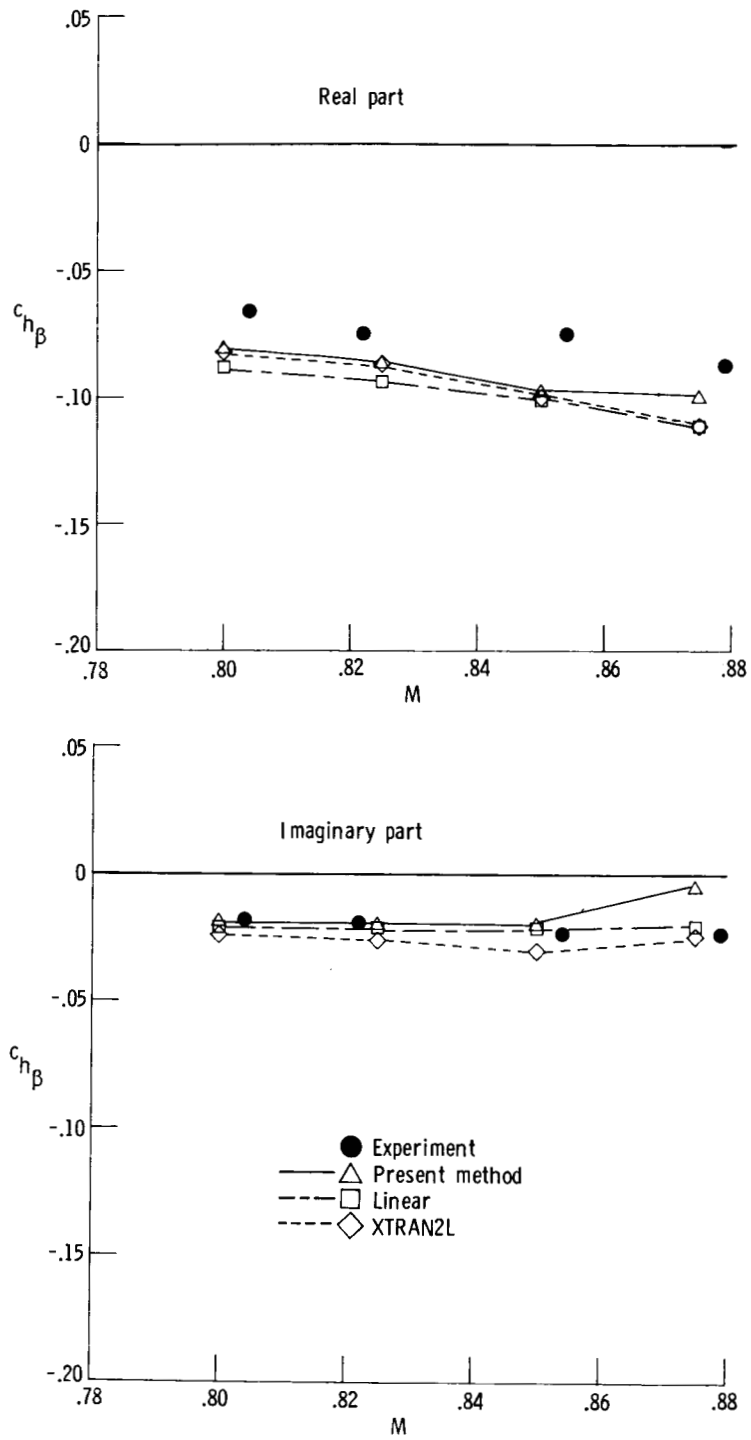
(c) Unsteady hinge moment.

Figure 17. Concluded.
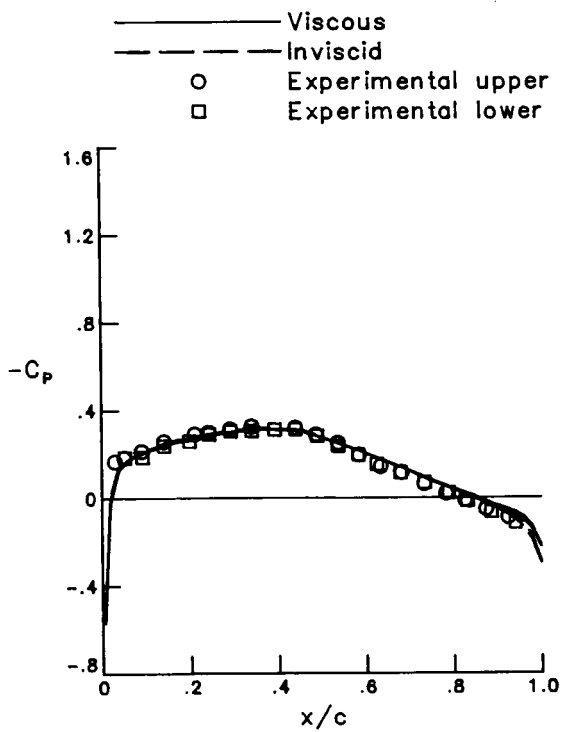
(a) Case 1. $M = 0.490$; $N_{Re} = 2.5 \times 10^6$.
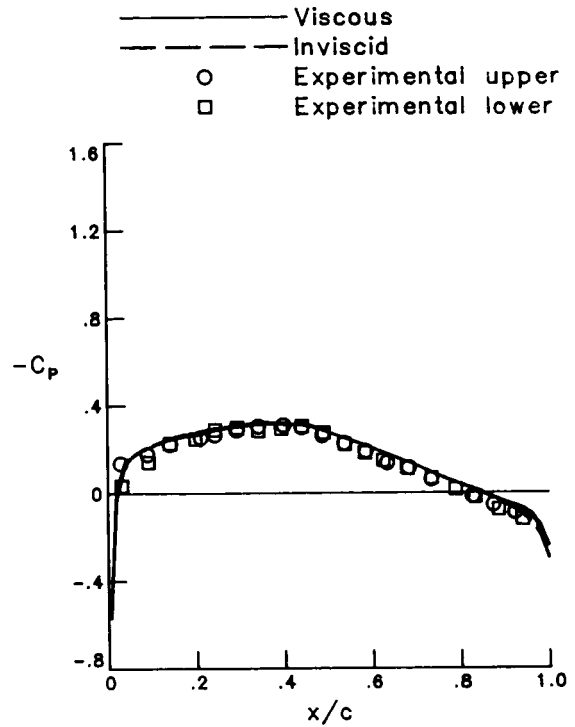
(b) Case 2. $M = 0.502$; $N_{Re} = 10.0 \times 10^6$.
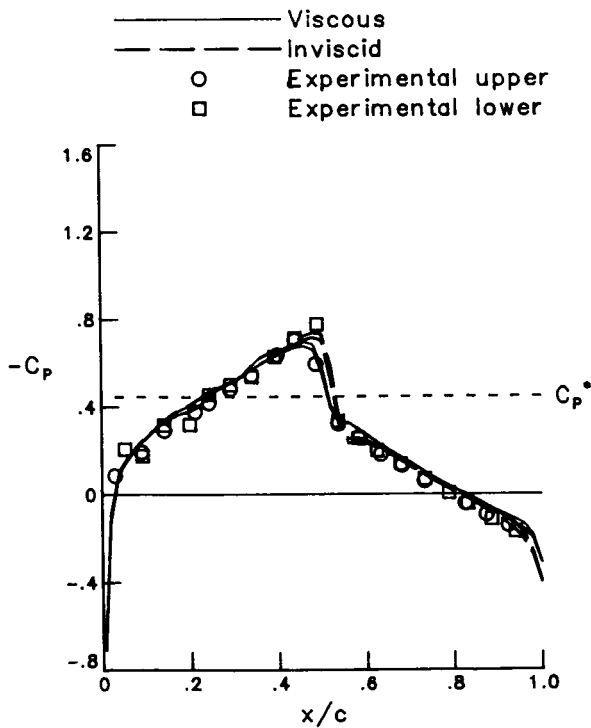
(c) Cases 3 to 8. $M = 0.796$; $N_{Re} = 12.5 \times 10^6$.
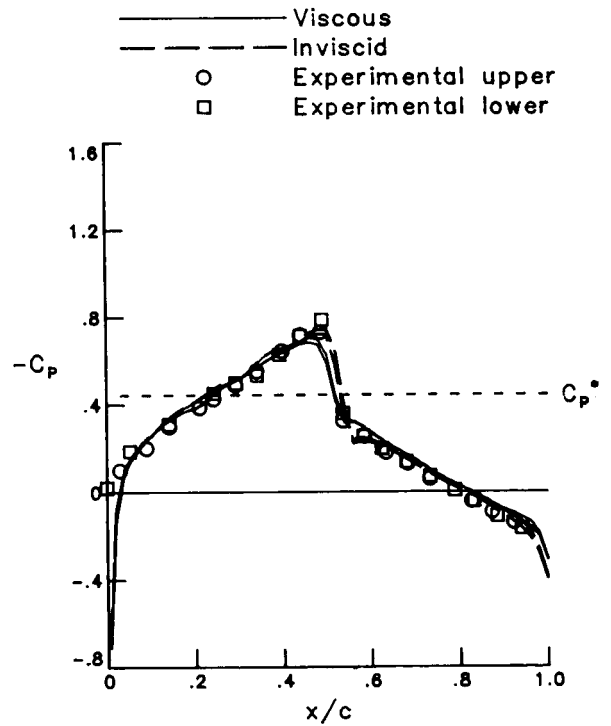
(d) Case 9. $M = 0.797$; $N_{Re} = 12.5 \times 10^6$.

Figure 18. Steady pressure distribution for cases 1 to 10 for NACA 64A010A airfoil. $\alpha_m = 0°$.
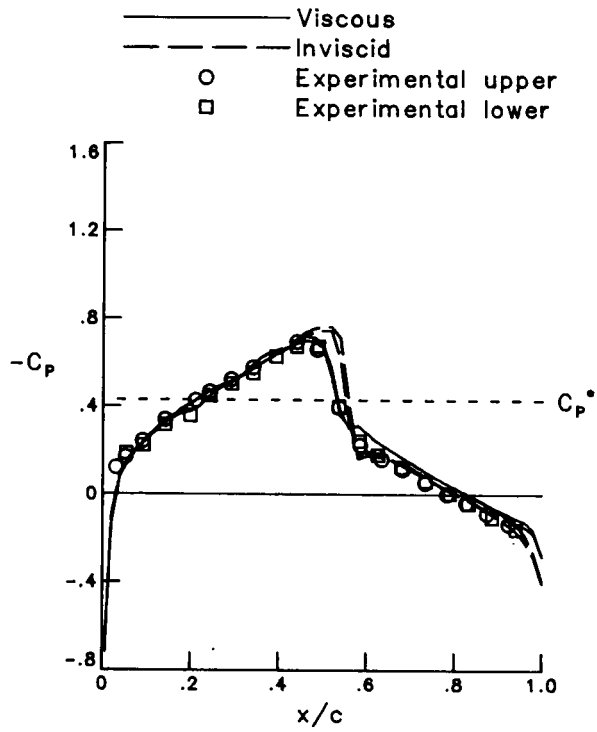
(e) Case 10. $M = 0.802$; $N_{\text{Re}} = 3.4 \times 10^6$.

Figure 18. Concluded.
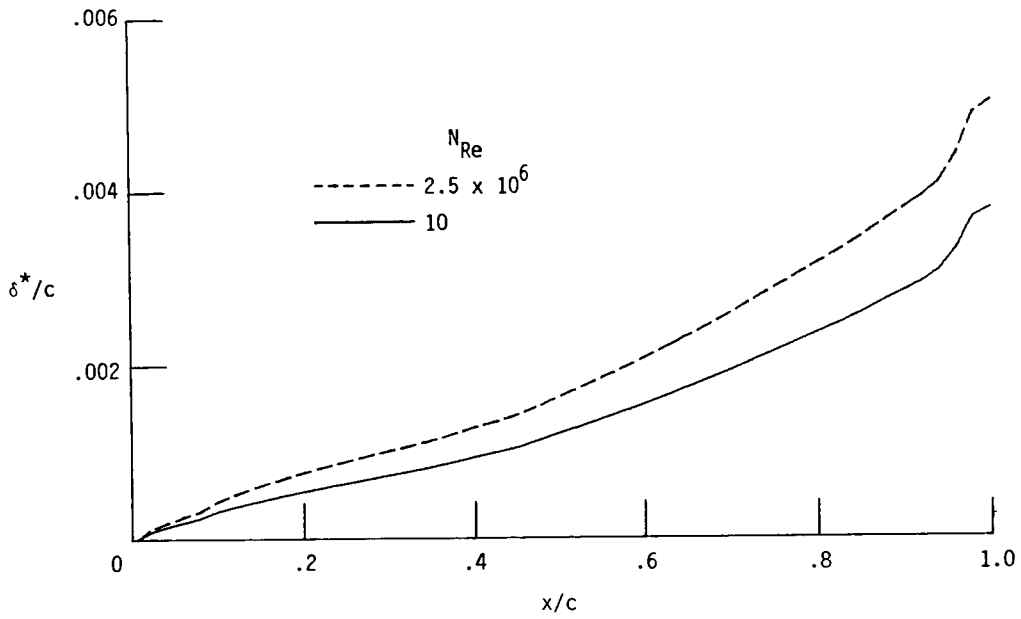
(a) $M \approx 0.5$.
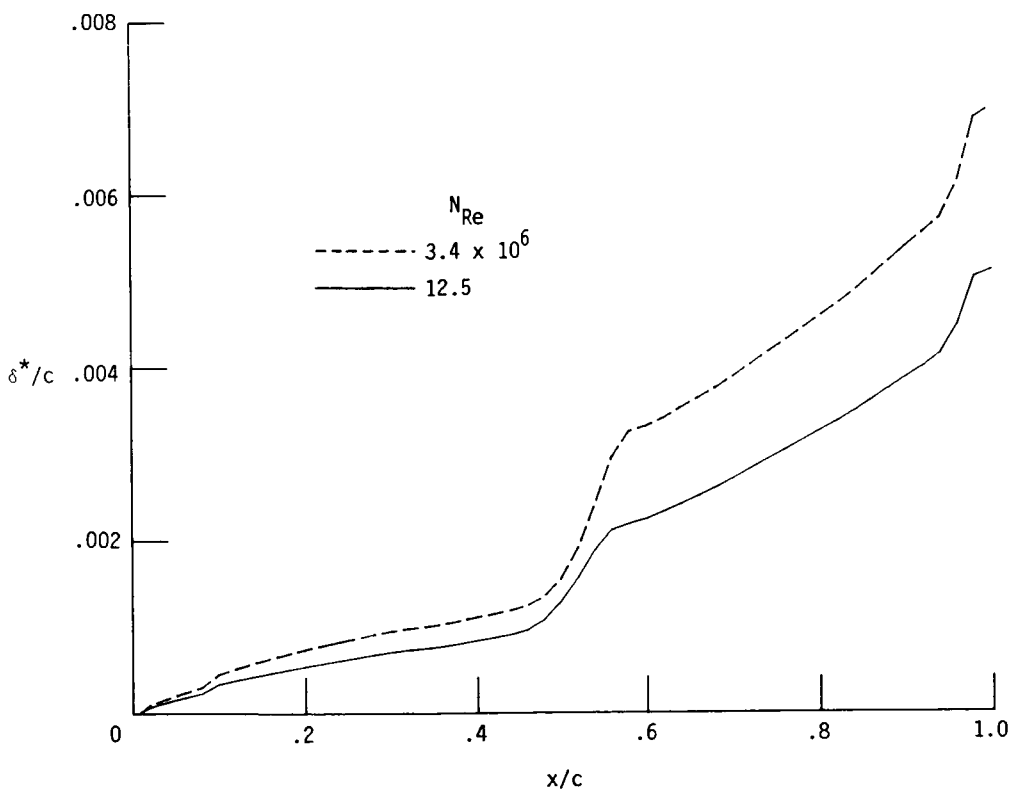
(b) $M \approx 0.8$.

Figure 19. Effect of Reynolds number on boundary-layer displacement thickness for NACA 64A010A airfoil in steady flow.
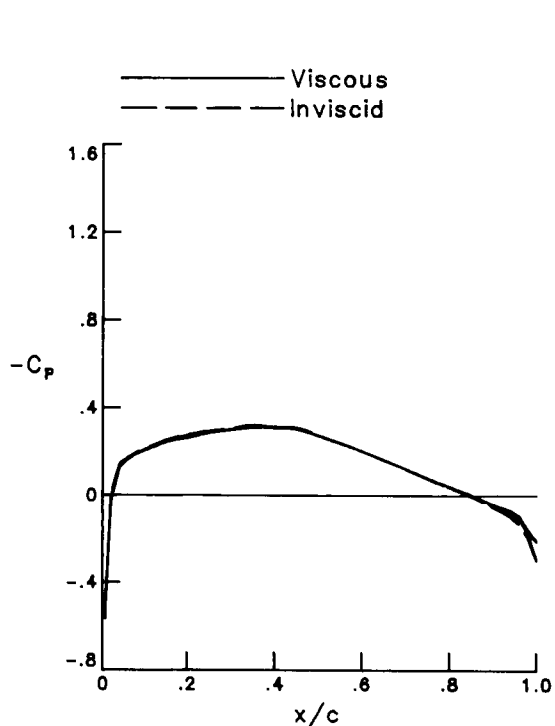
(a) Mean.
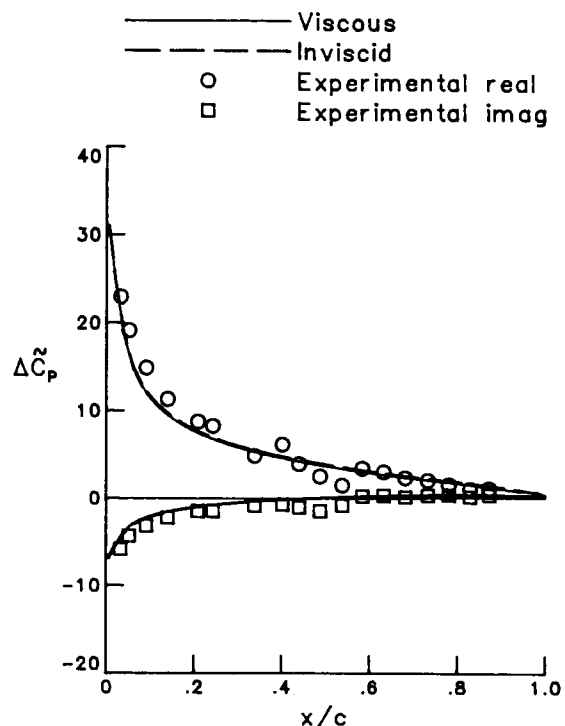
(b) Lifting.
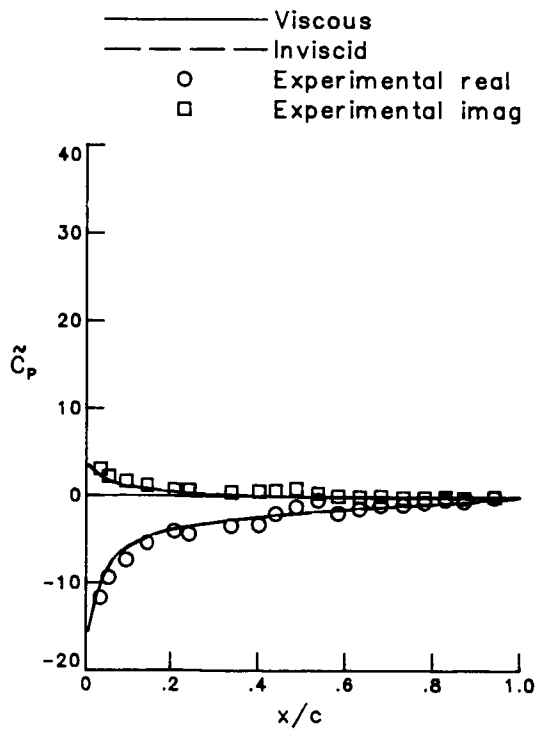
(c) Upper surface.
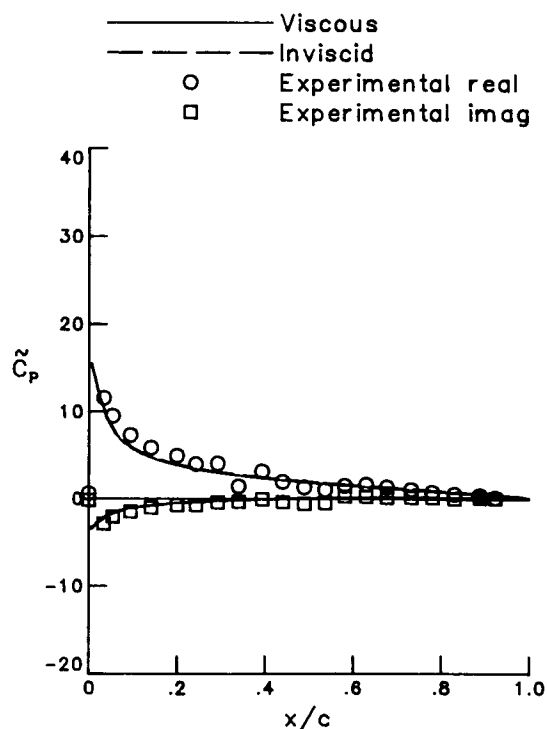
(d) Lower surface.

Figure 20. Unsteady pressure distribution for case 1 for NACA 64A010A airfoil. $M = 0.490$; $\alpha_o = 0.96°$; $k = 0.100$; $N_{Re} = 2.5 \times 10^6$.
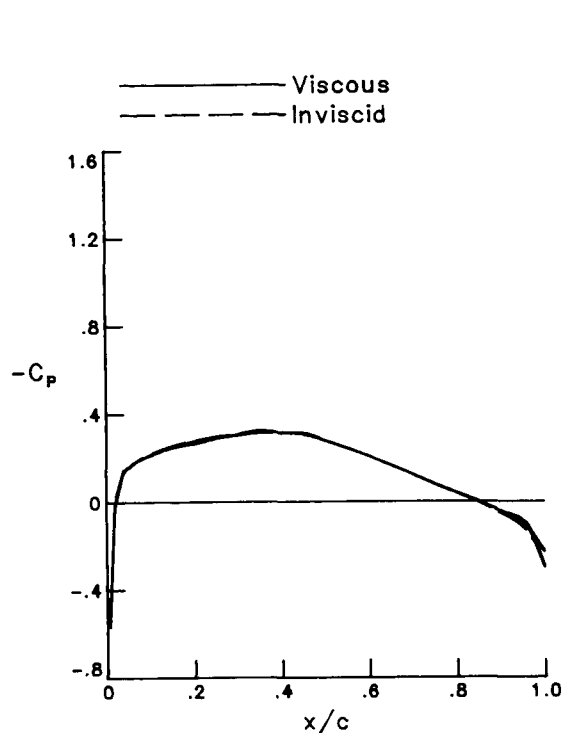
(a) Mean.
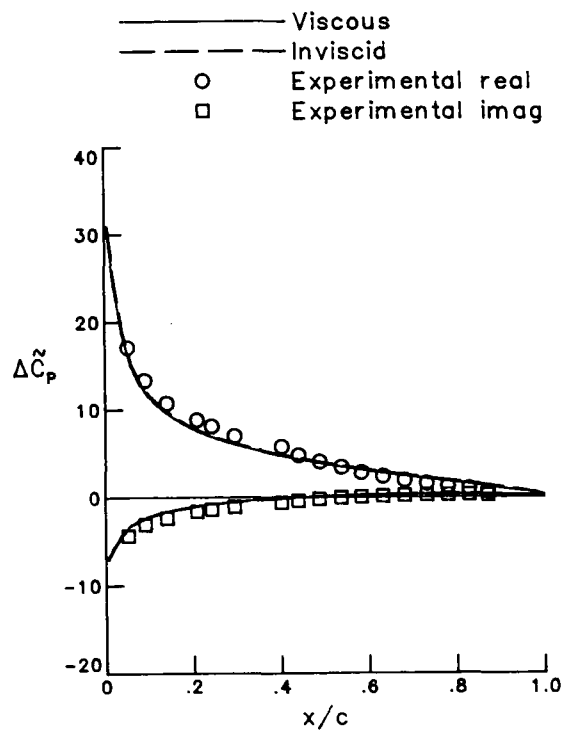
(b) Lifting.
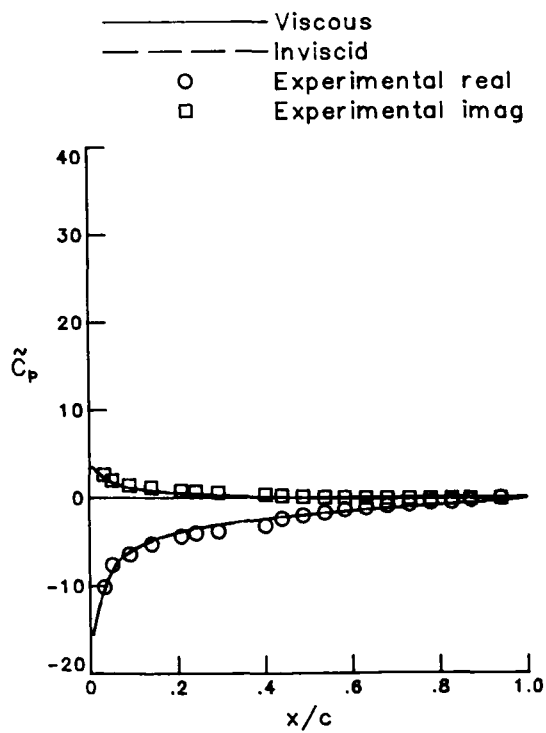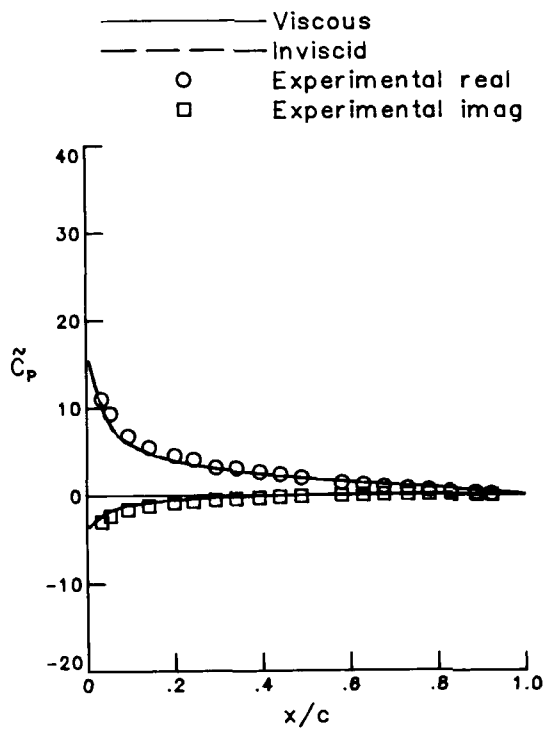
(c) Upper surface.

(d) Lower surface.

Figure 21. Unsteady pressure distribution for case 2 for NACA 64A010A airfoil. $M = 0.502$; $\alpha_o = 1.02°$; $k = 0.100$; $N_{Re} = 10 \times 10^6$.

(a) Mean.

(b) Lifting.

(c) Upper surface.
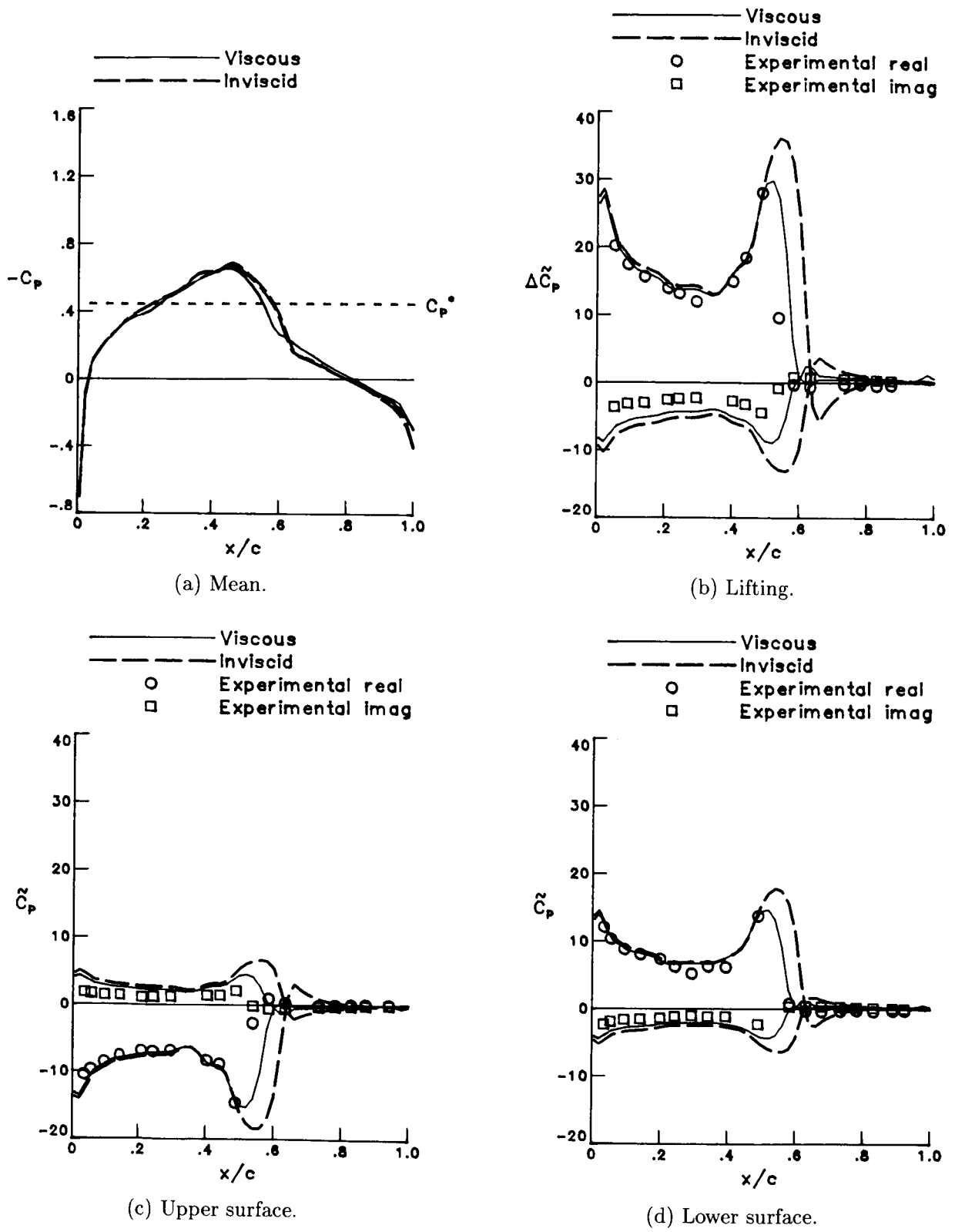
(d) Lower surface.

Figure 22. Unsteady pressure distribution for case 3 for NACA 64A010A airfoil. $M = 0.796$; $\alpha_o = 1.03°$; $k = 0.025$; $N_{Re} = 12.5 \times 10^6$.
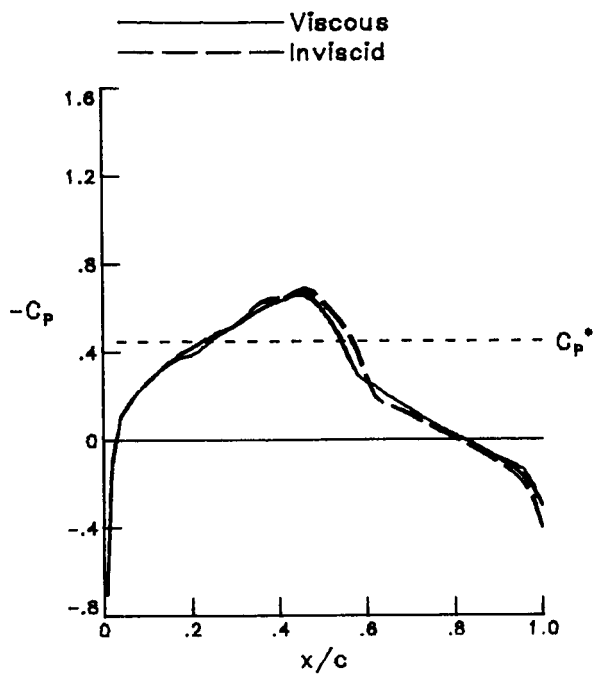
(a) Mean.
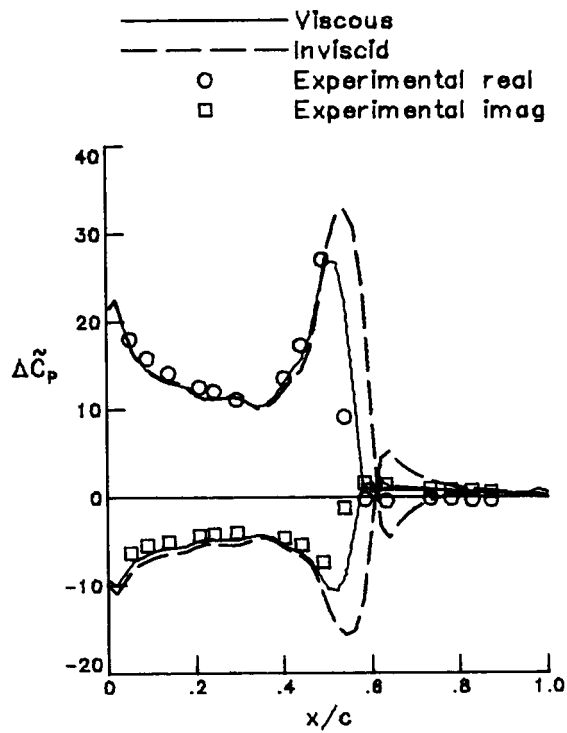
(b) Lifting.
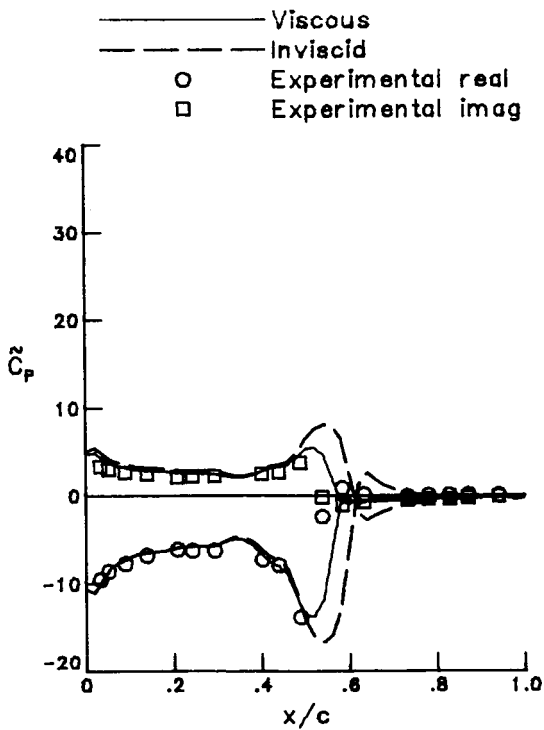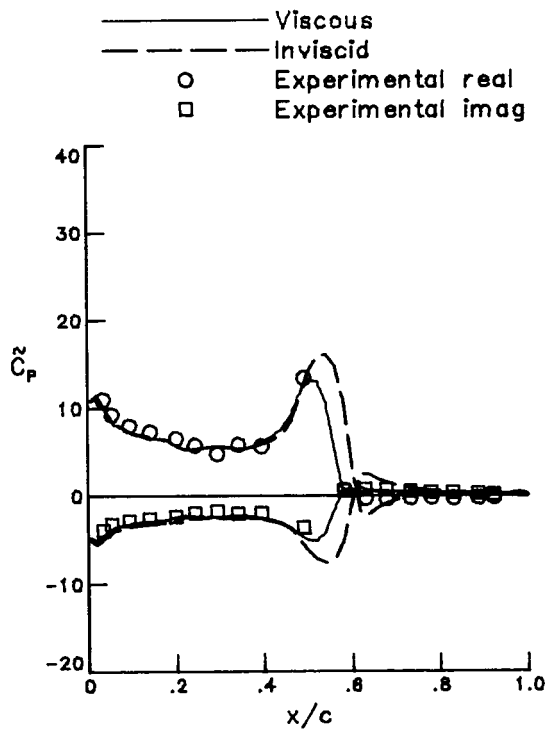
(c) Upper surface.

(d) Lower surface.

Figure 23. Unsteady pressure distribution for case 4 for NACA 64A010A airfoil. $M = 0.796$; $\alpha_o = 1.02°$; $k = 0.051$; $N_{Re} = 12.5 \times 10^6$.
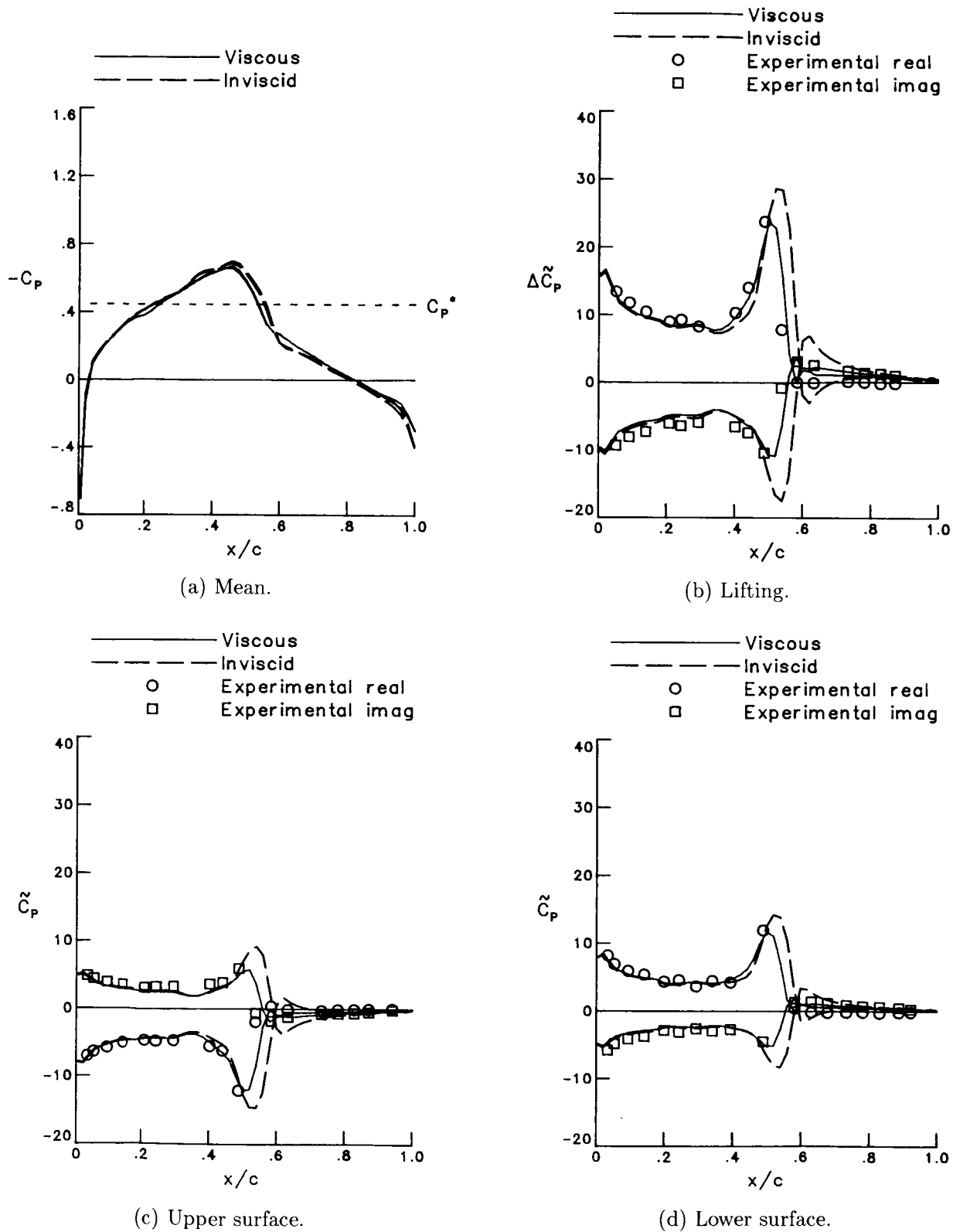
Figure 24. Unsteady pressure distribution for case 5 for NACA 64A010A airfoil. $M = 0.796$; $\alpha_o = 1.02°$; $k = 0.101$; $N_{Re} = 12.5 \times 10^6$.
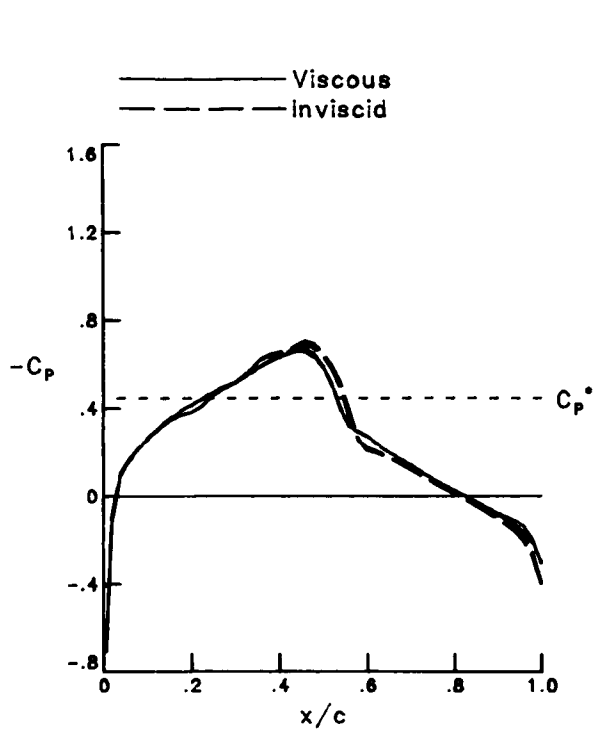
(a) Mean.
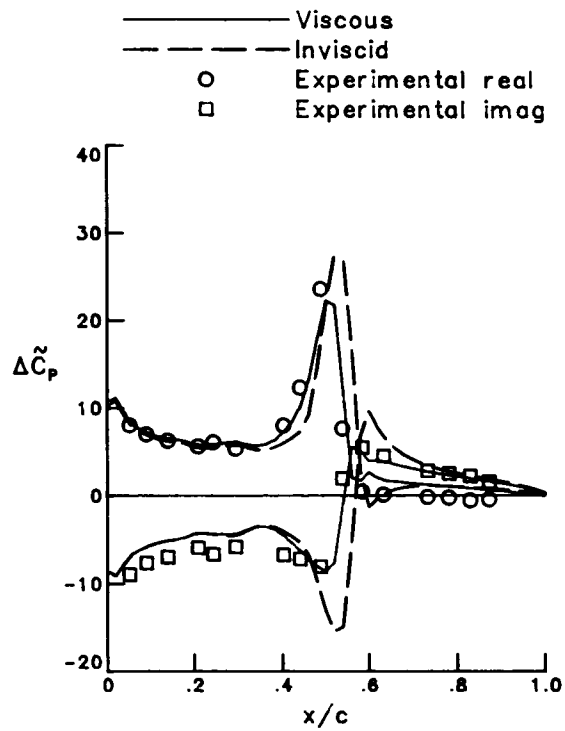
(b) Lifting.
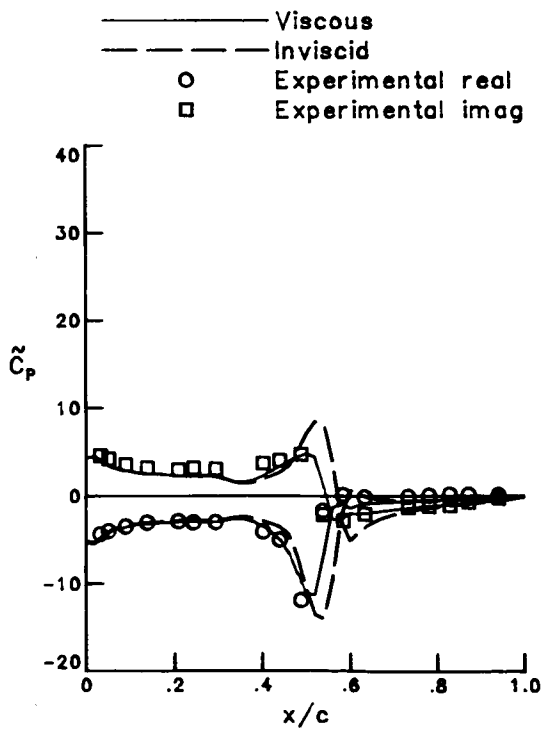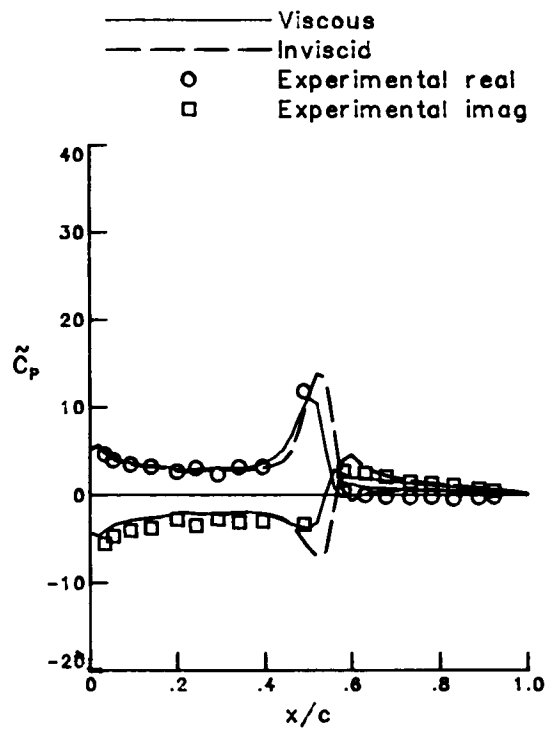
(c) Upper surface.

(d) Lower surface.

Figure 25. Unsteady pressure distribution for case 6 for NACA 64A010A airfoil. $M = 0.796$; $\alpha_o = 1.01°$; $k = 0.202$; $N_{\mathrm{Re}} = 12.5 \times 10^6$.

(a) Mean.

(b) Lifting.

(c) Upper surface.

(d) Lower surface.
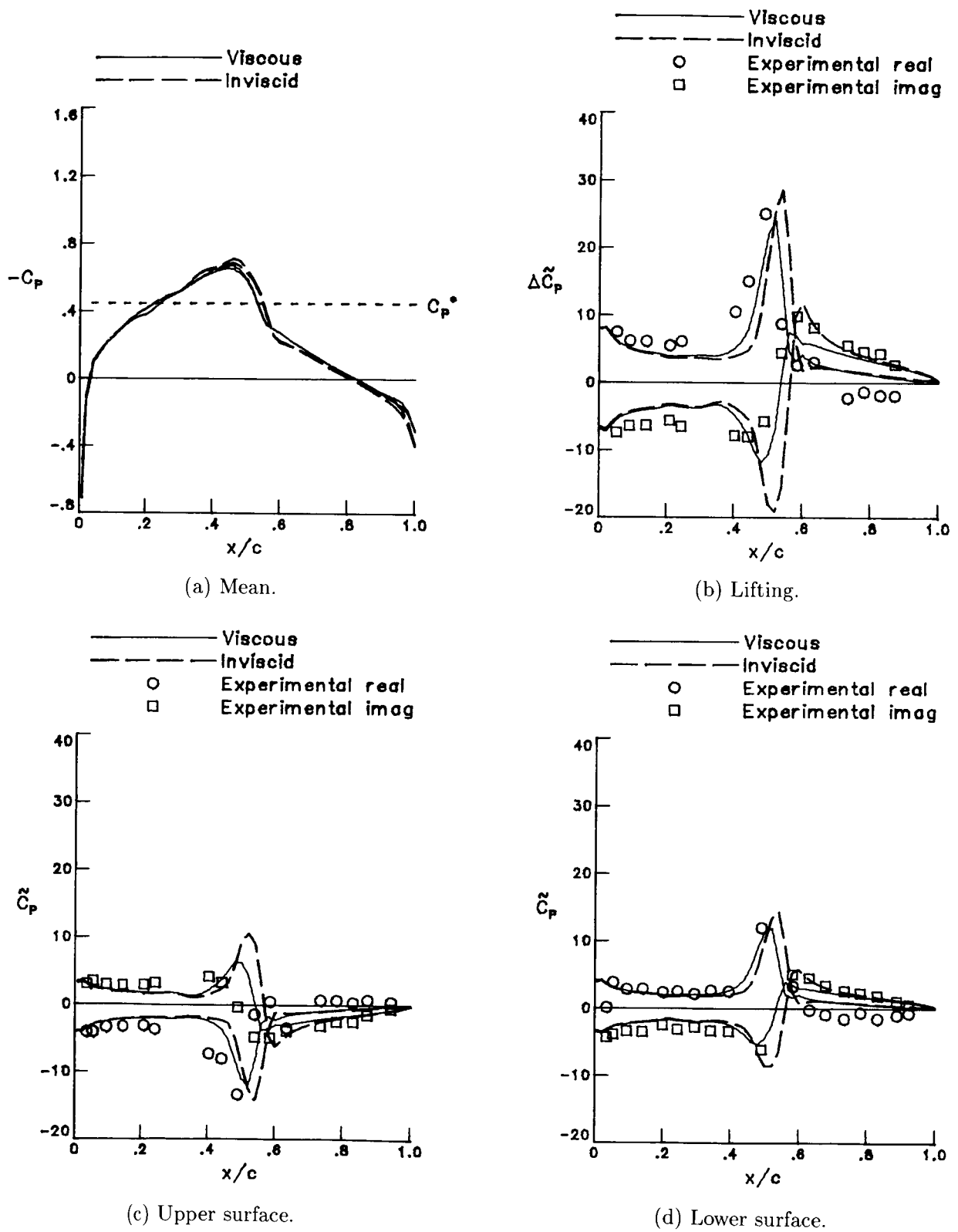
Figure 26. Unsteady pressure distribution for case 7 for NACA 64A010A airfoil. $M = 0.796$; $\alpha_o = 0.99°$; $k = 0.303$; $N_{Re} = 12.5 \times 10^6$.
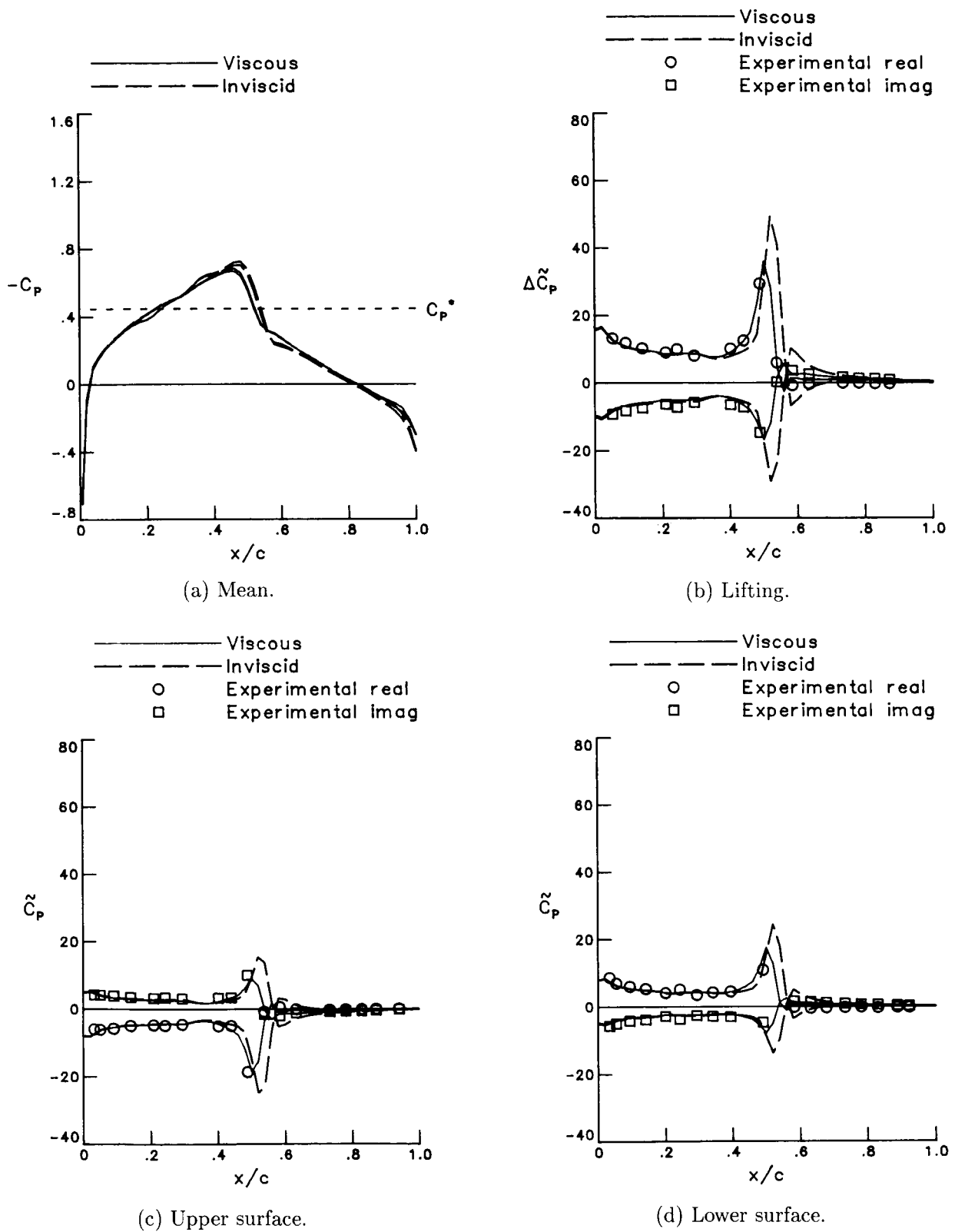
Figure 27. Unsteady pressure distribution for case 8 for NACA 64A010A airfoil. $M = 0.796$; $\alpha_o = 0.51°$; $k = 0.101$; $N_{Re} = 12.5 \times 10^6$.

(a) Mean.

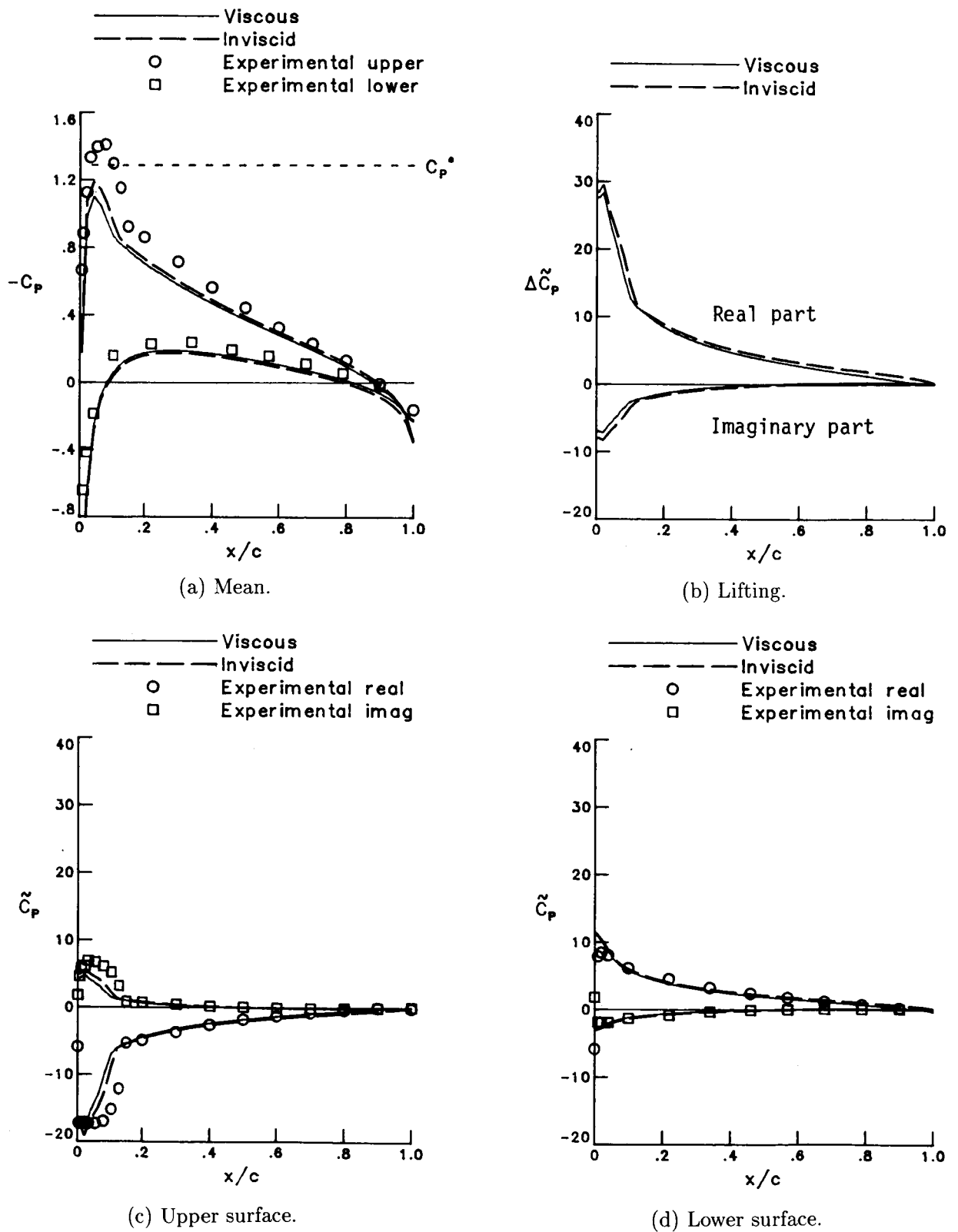(b) Lifting.

(c) Upper surface.

(d) Lower surface.
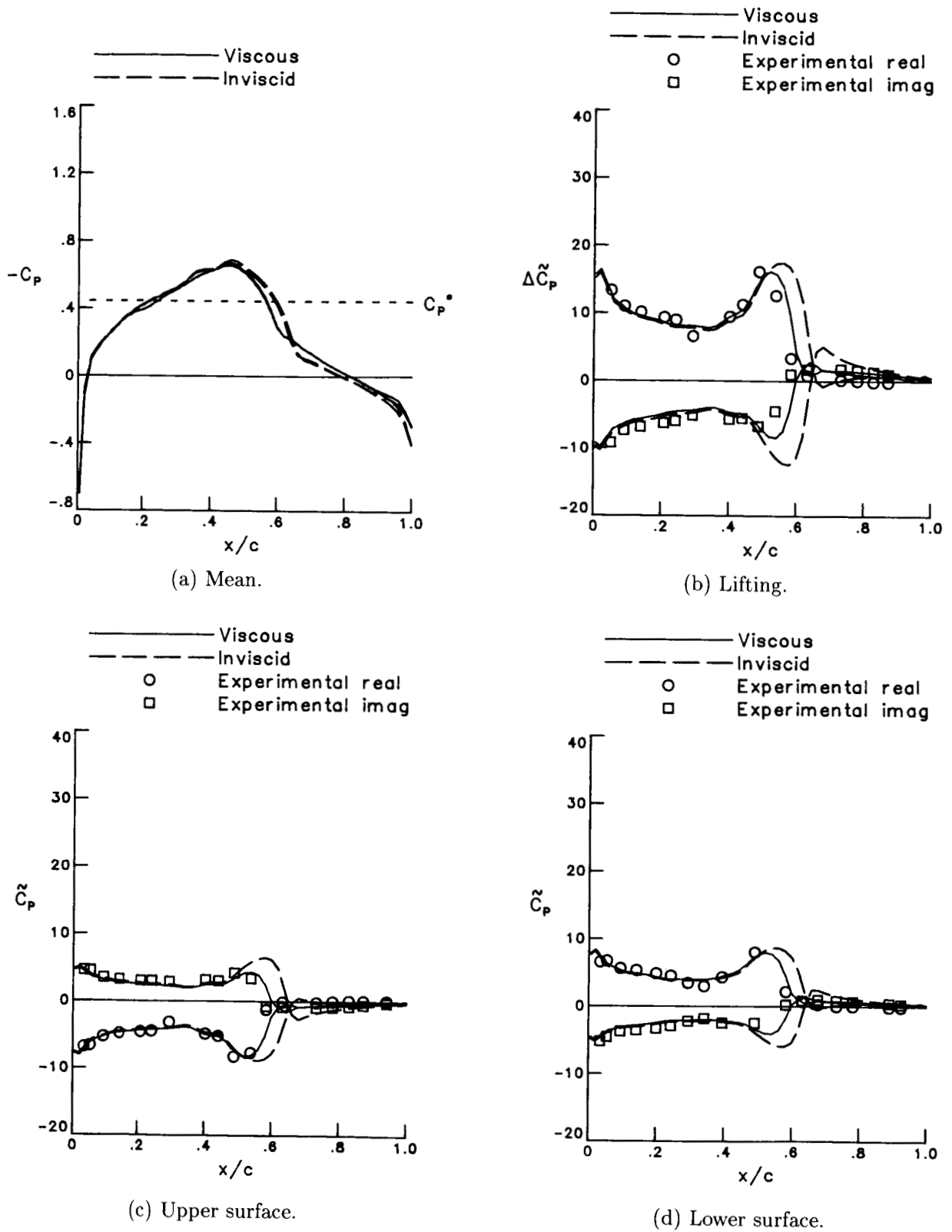
Figure 28. Unsteady pressure distribution for case 9 for NACA 64A010A airfoil. $M = 0.797$; $\alpha_o = 2.00°$; $k = 0.101$; $N_{Re} = 12.5 \times 10^6$.

(a) Mean.

(b) Lifting.

(c) Upper surface.

(d) Lower surface.
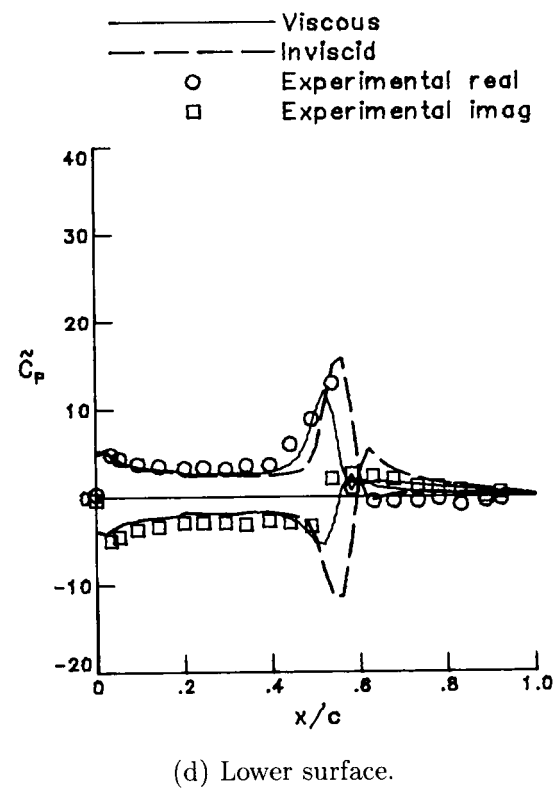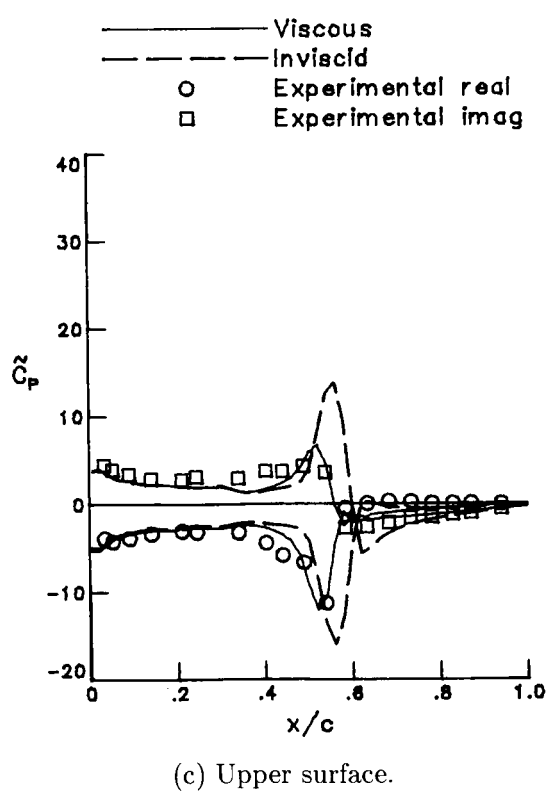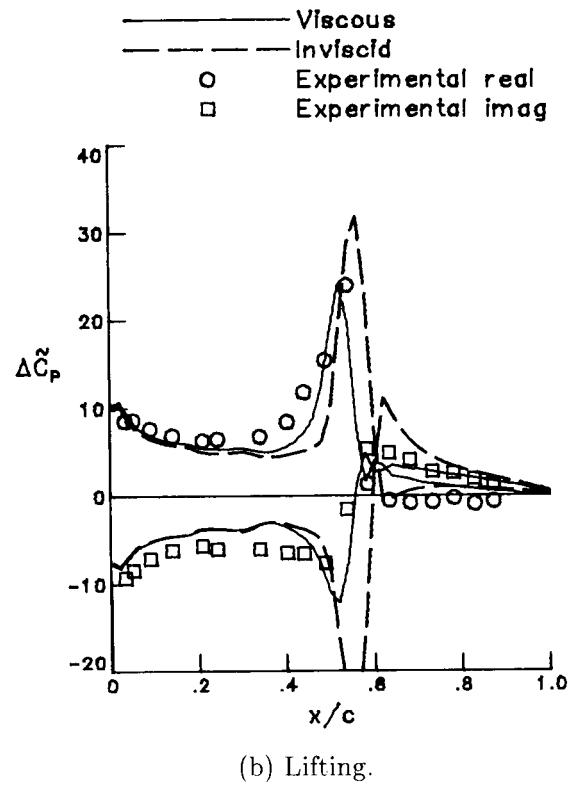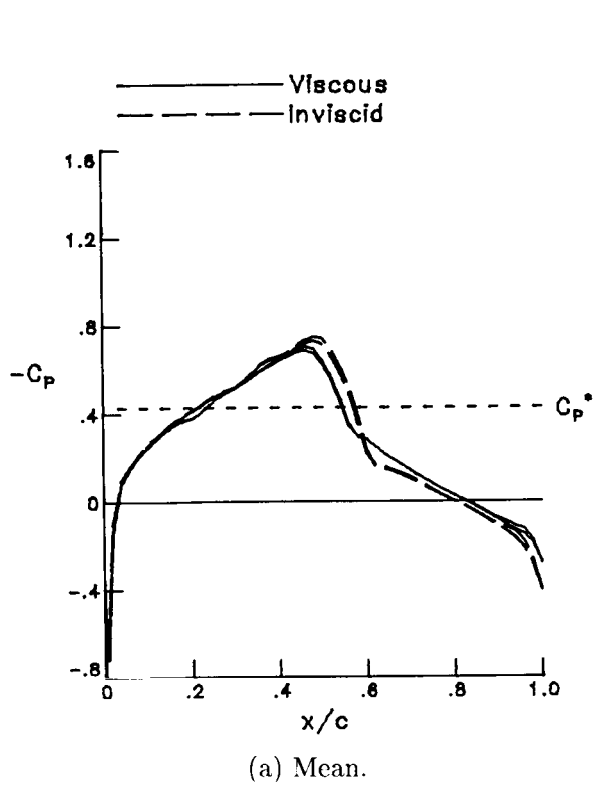
Figure 29. Unsteady pressure distribution for case 10 for NACA 64A010A airfoil. $M = 0.802$; $\alpha_o = 0.94°$; $k = 0.200$; $N_{\mathrm{Re}} = 3.4 \times 10^6$.
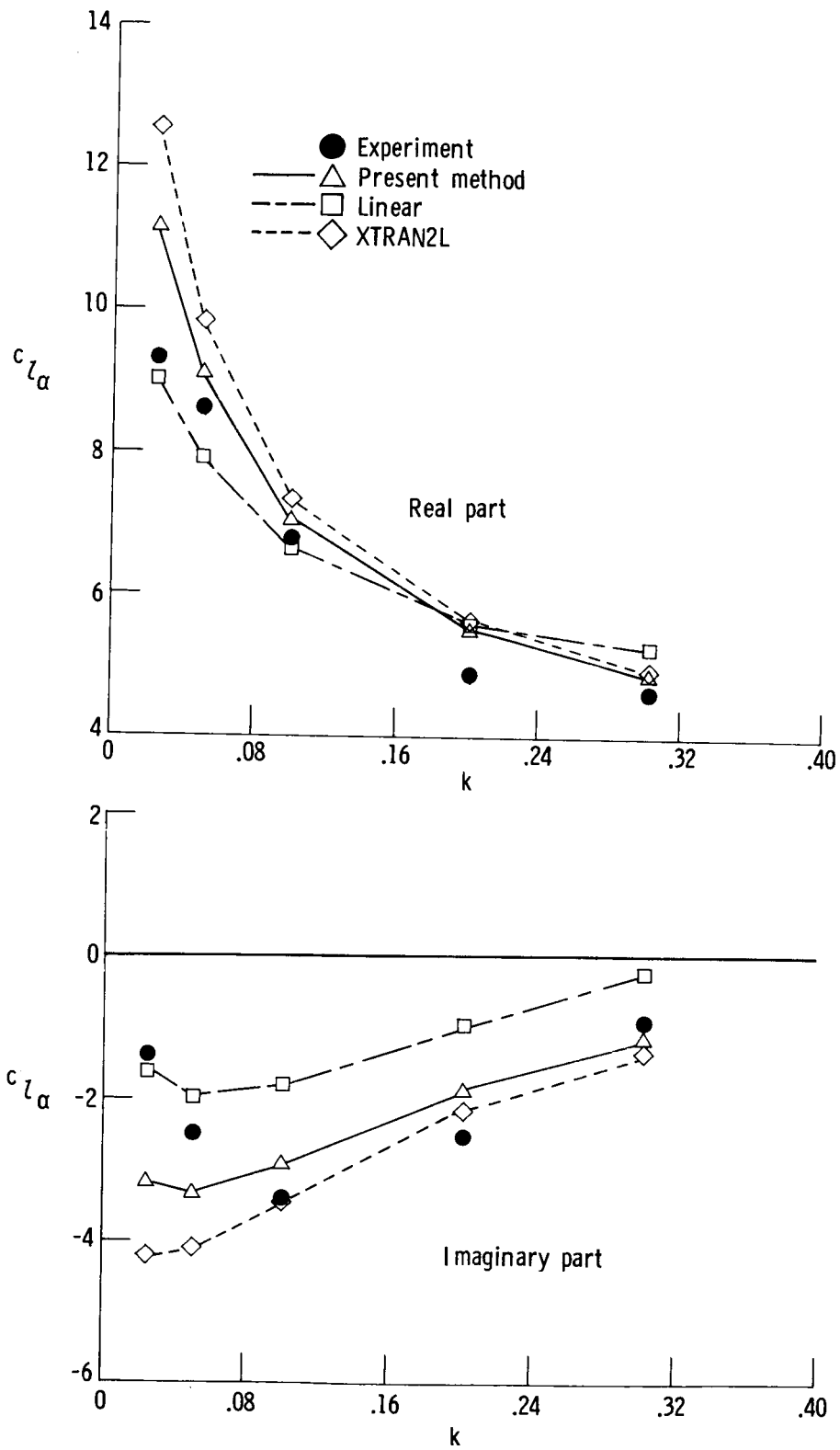
(a) Unsteady lift.

Figure 30. Comparison of unsteady forces for NACA 64A010A airfoil. $M = 0.796; \alpha_o = 1°$.
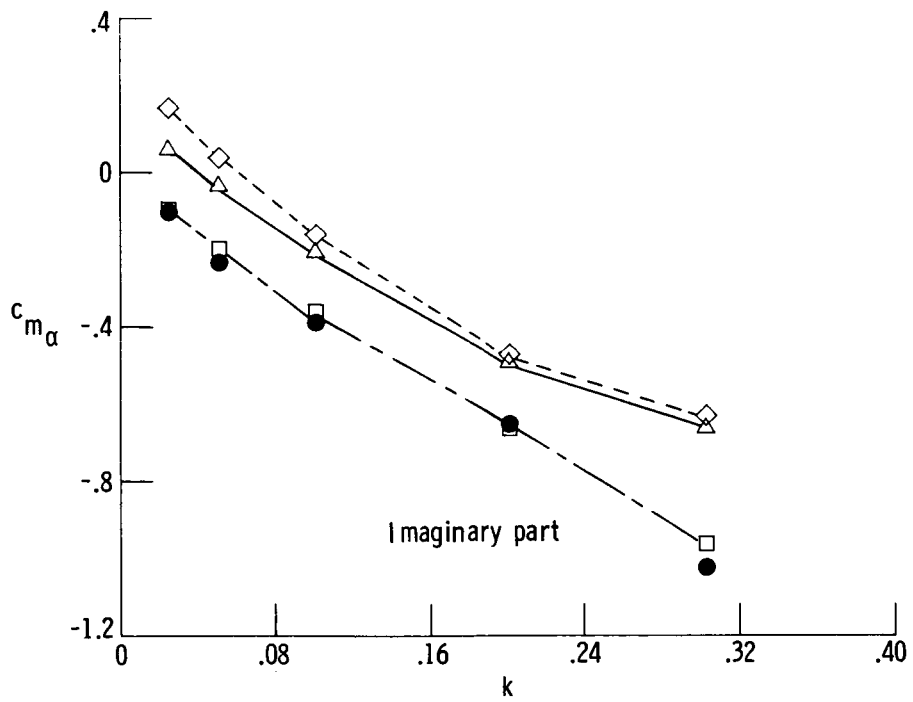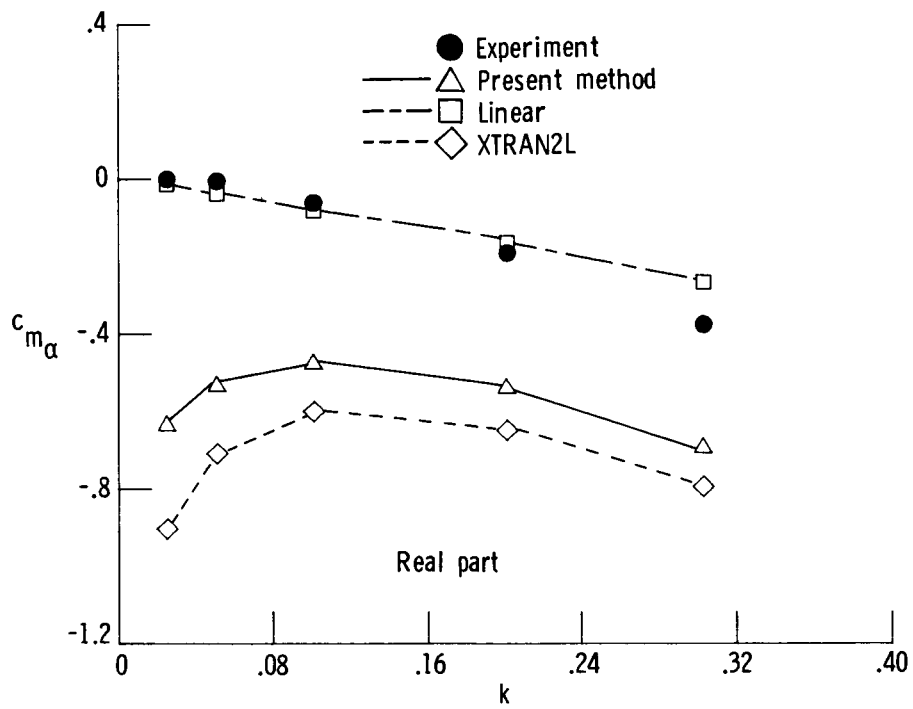
(b) Unsteady pitching moment.

Figure 30. Concluded.
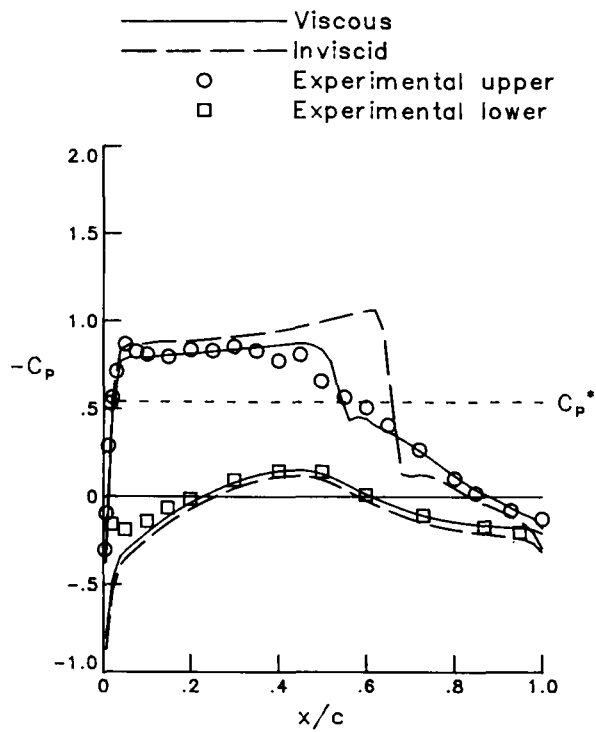
Figure 31. Steady pressure distribution for cases 3 to 5 and 11 to 13 for MBB-A3 airfoil. $M = 0.765; \alpha_m = 1.5°$.
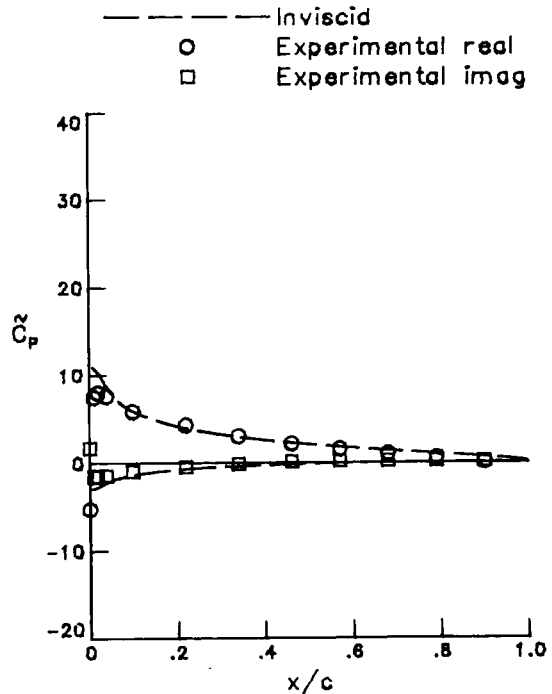
(a) Mean.

(b) Lifting.
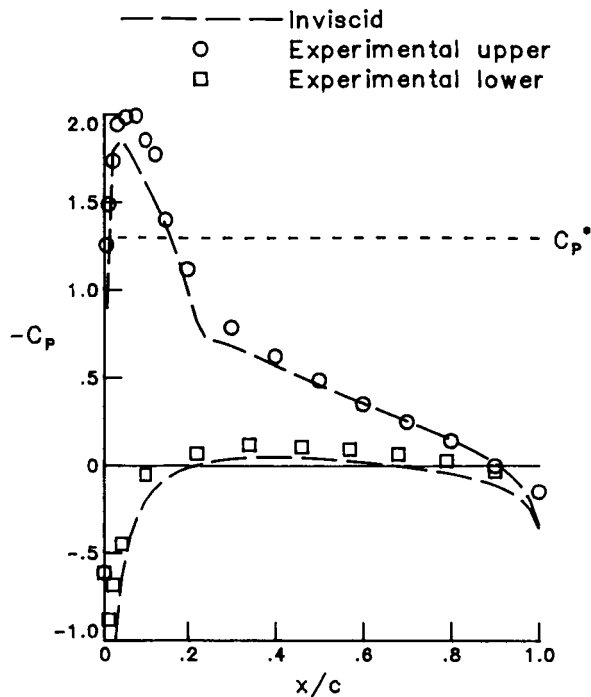
(c) Upper surface.
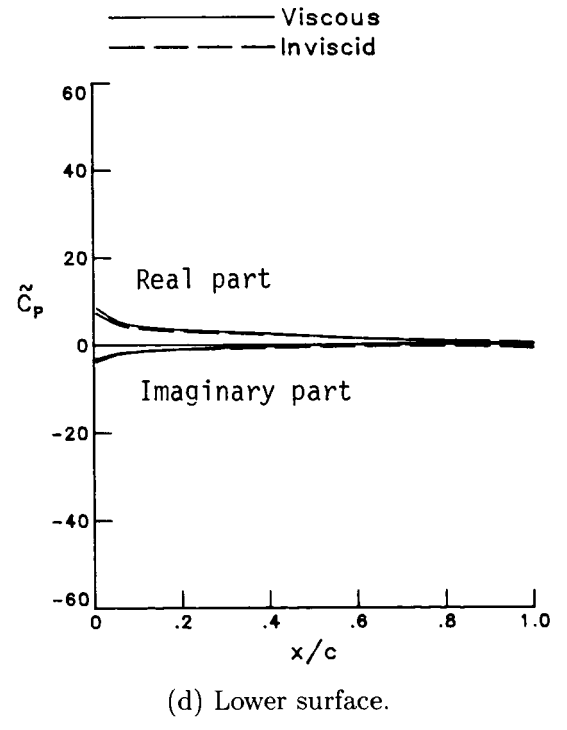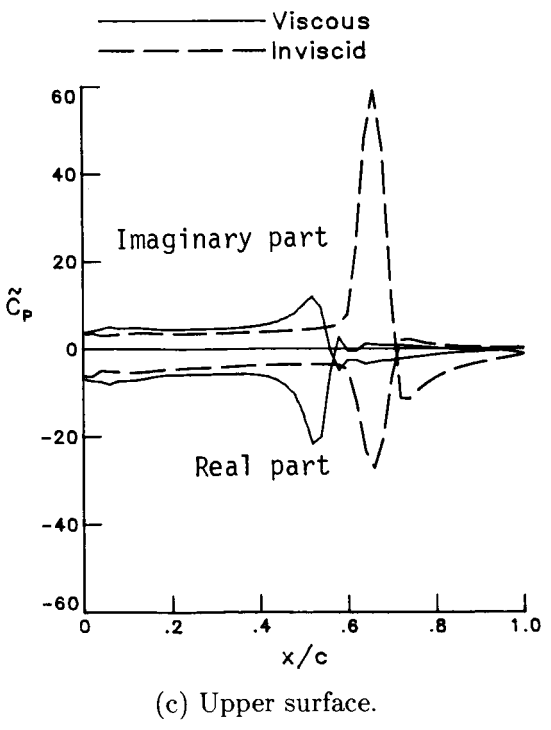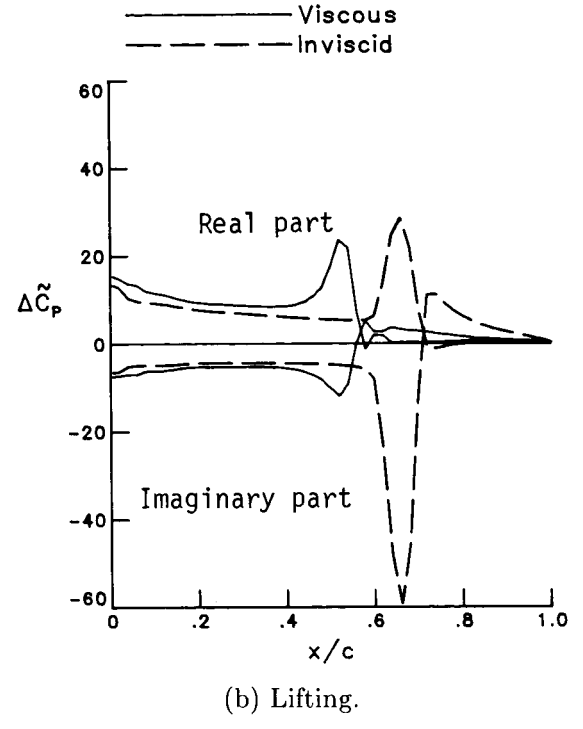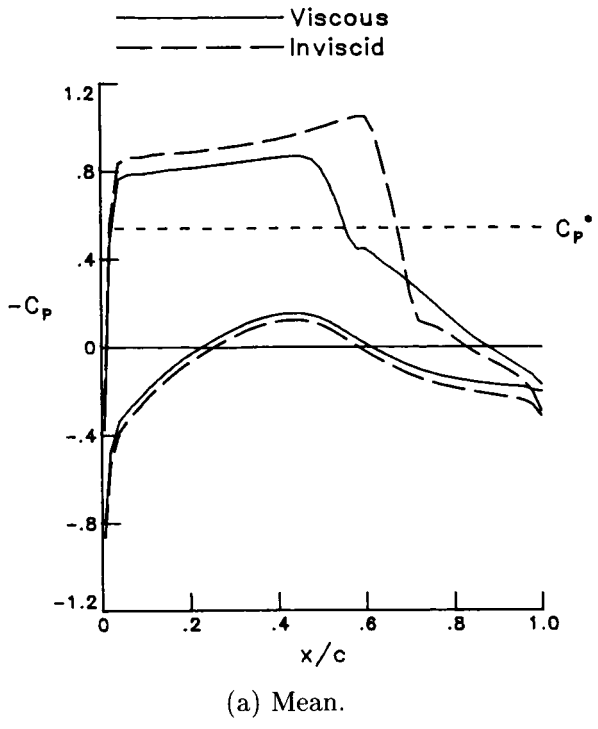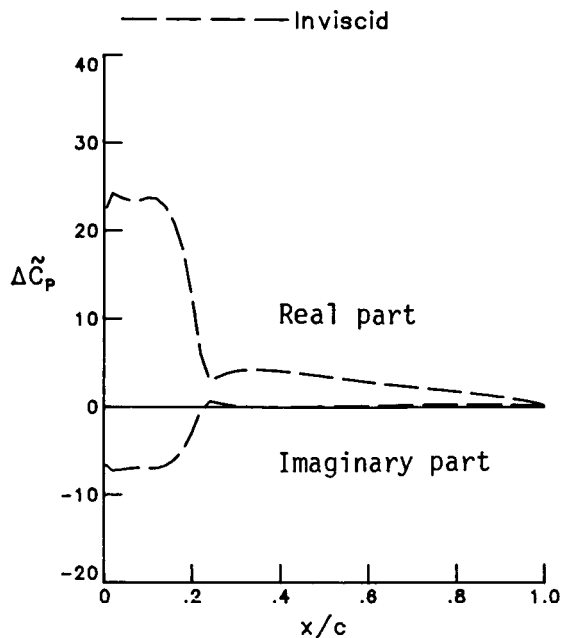
(d) Lower surface.

Figure 32. Unsteady pressure distribution for case 3 for MBB-A3 airfoil. $M = 0.765$; $\alpha_m = 1.5°$; $\alpha_o = 0.5°$; $k = 0.1$.
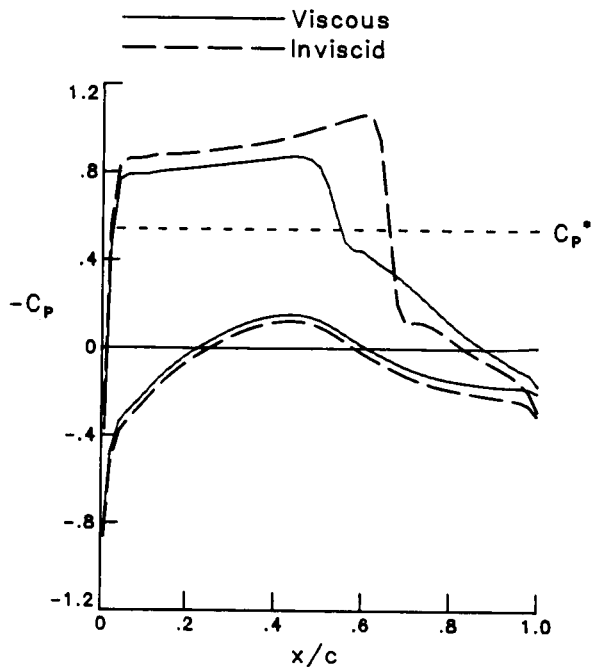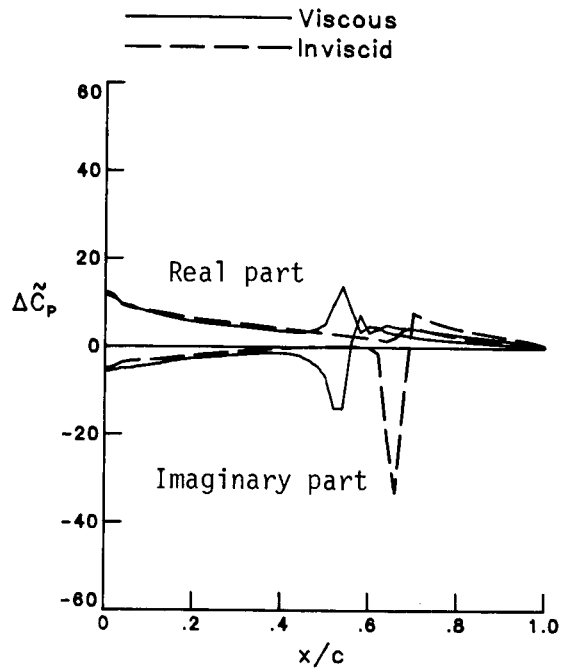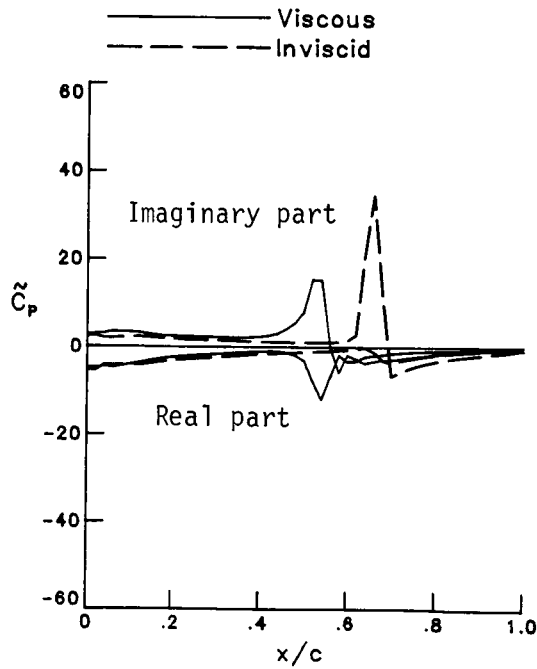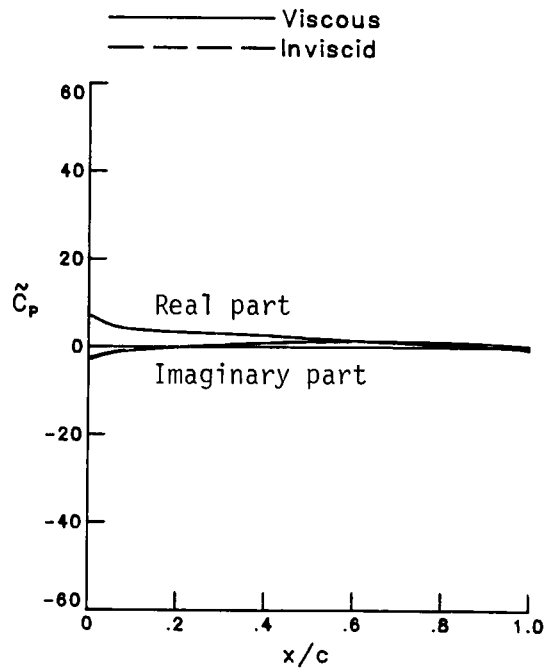
Figure 33. Unsteady pressure distribution for case 4 for MBB-A3 airfoil. $M = 0.765$; $\alpha_m = 1.5°$; $\alpha_o = 0.5°$; $k = 0.3$.
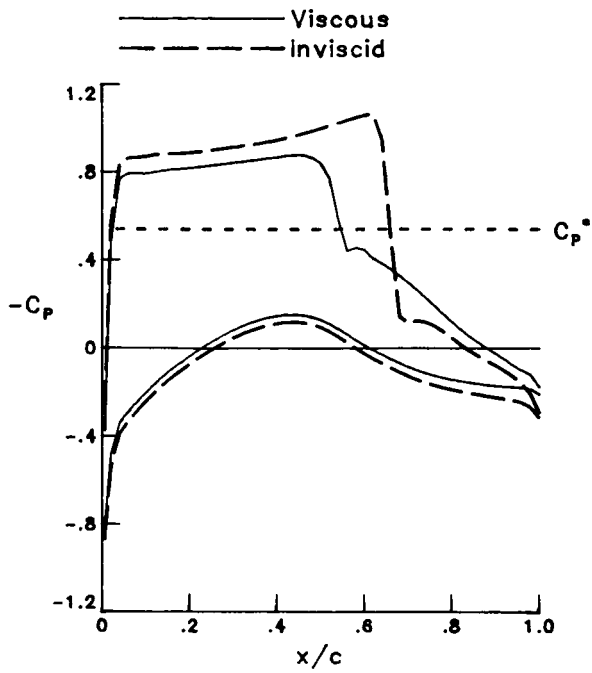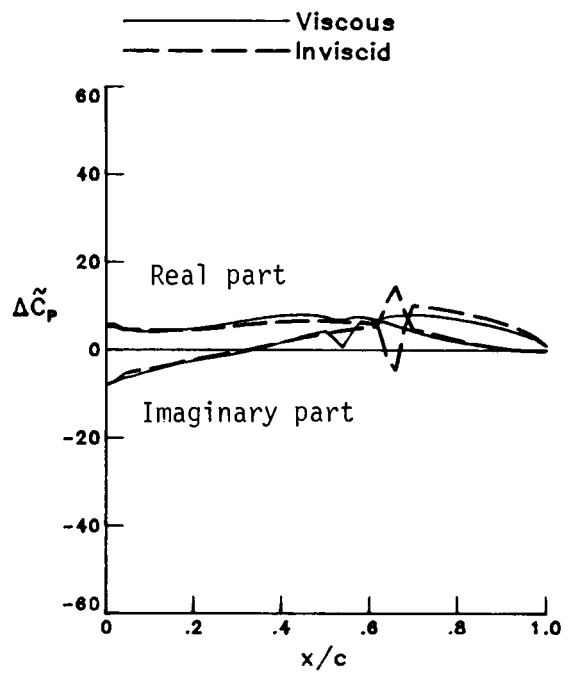
Figure 34. Unsteady pressure distribution for case 5 for MBB-A3 airfoil. $M = 0.765$; $\alpha_m = 1.5°$; $\alpha_o = 0.5°$; $k = 0.9$.
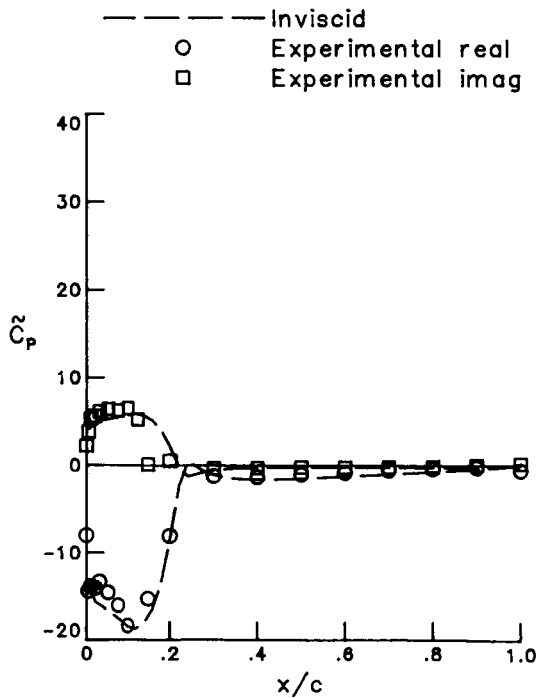
(a) Mean.

(b) Lifting.

(c) Upper surface.
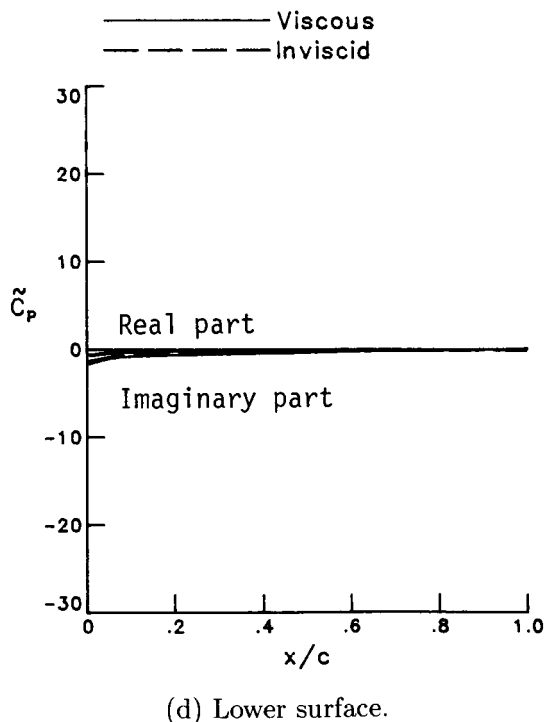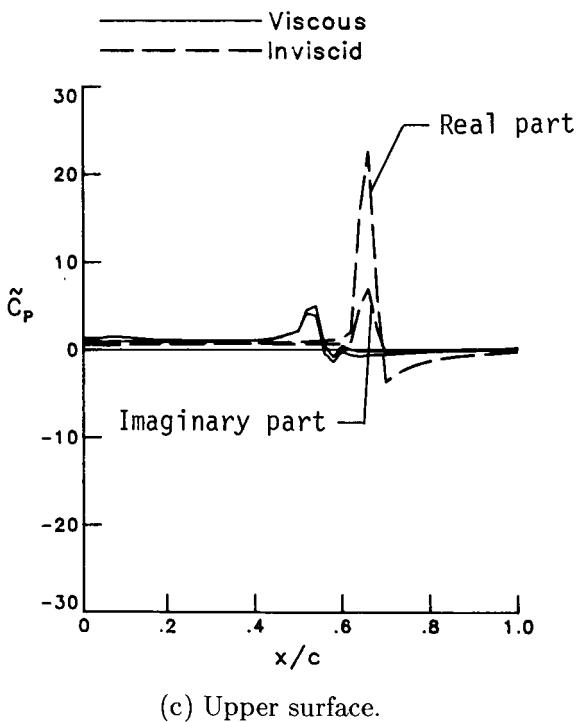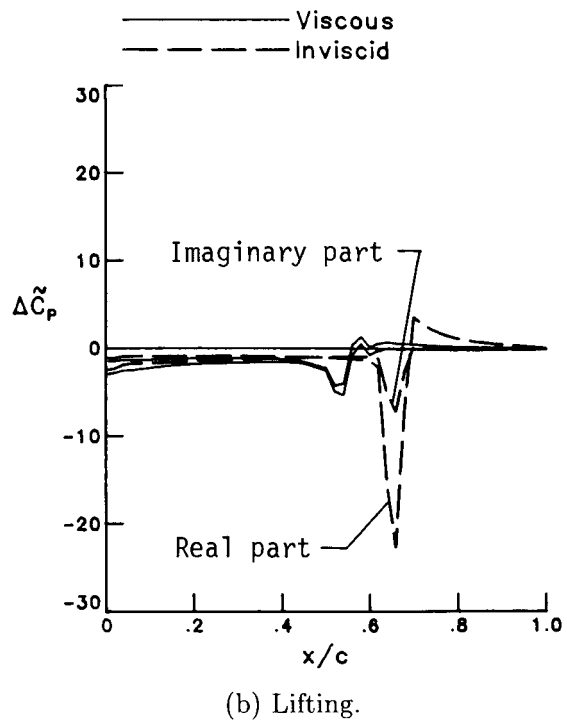
(d) Lower surface.

Figure 35.   Unsteady pressure distribution for case 11 for MBB-A3 airfoil. $M = 0.765$; $\alpha_m = 1.5°$; $h_o/c = 0.01$; $k = 0.1$.
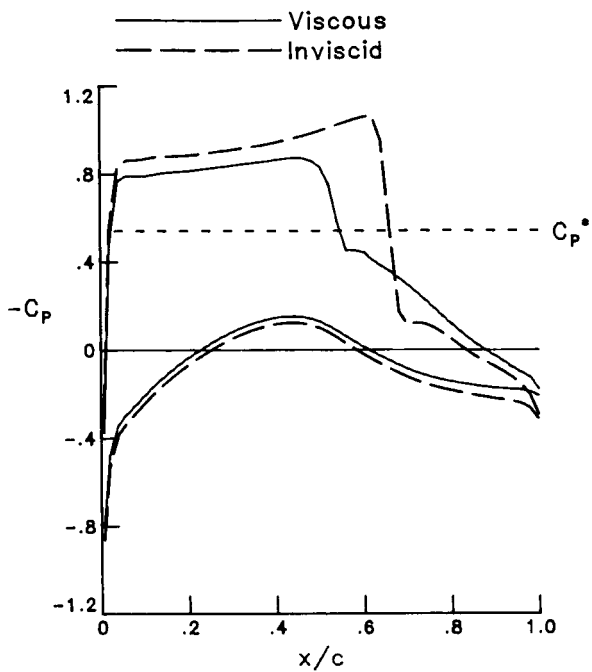
(a) Mean.
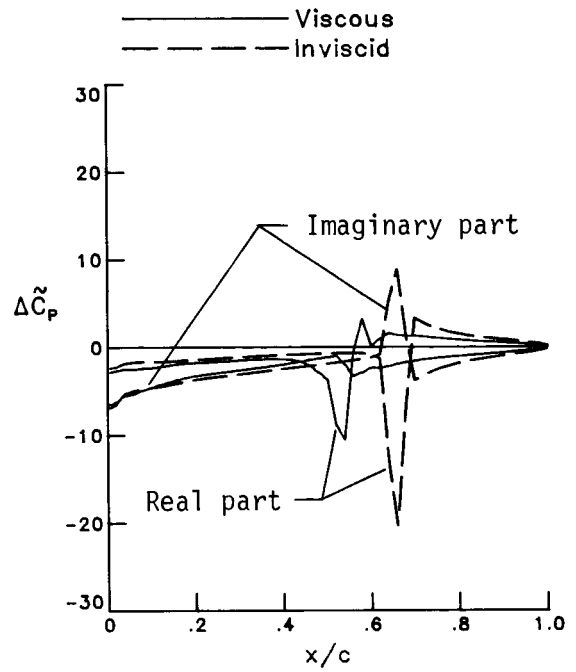
(b) Lifting.
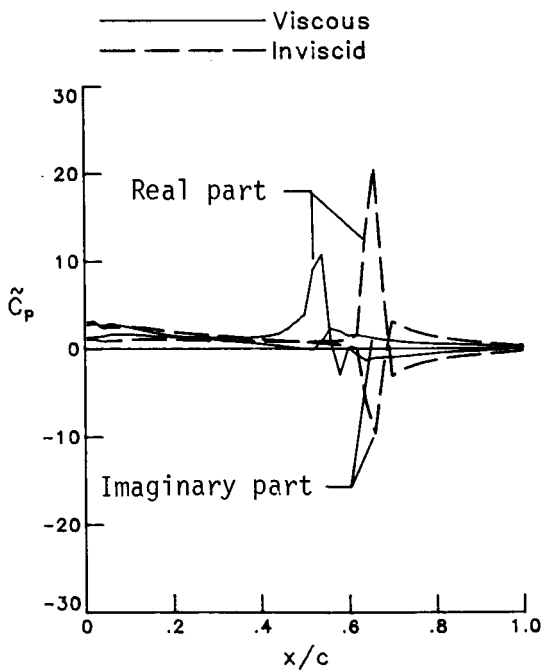
(c) Upper surface.

(d) Lower surface.

Figure 36. Unsteady pressure distribution for case 12 for MBB-Λ3 airfoil. $M = 0.765$; $\alpha_m = 1.5°$; $h_o/c = 0.01$; $k = 0.3$.
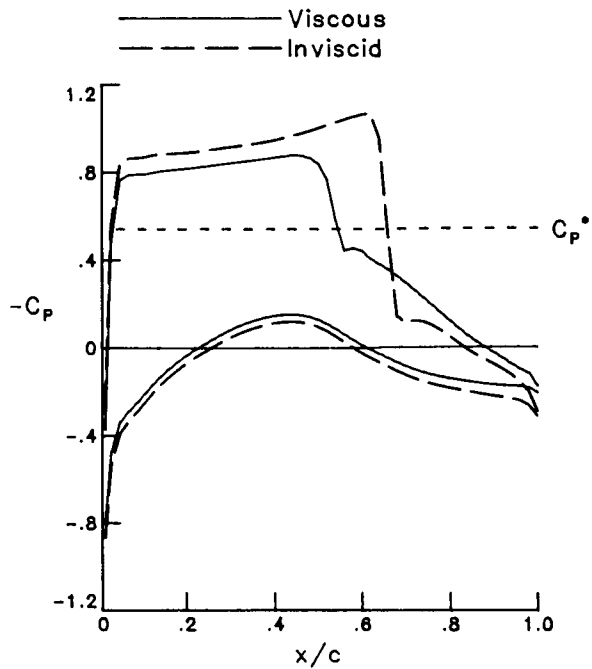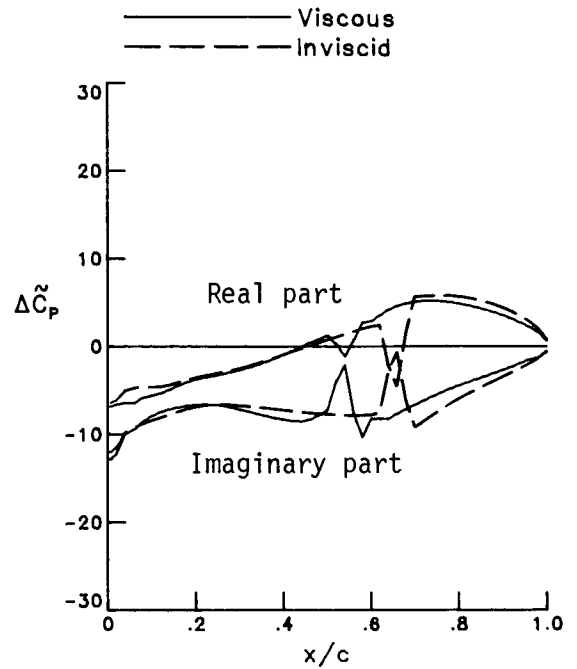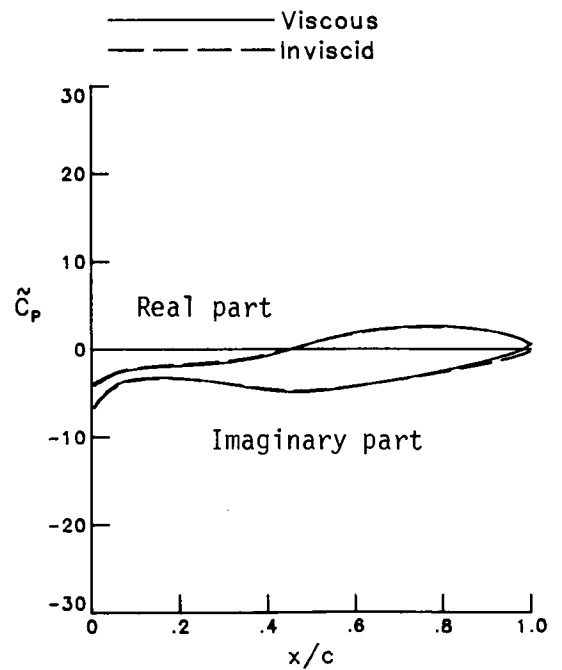
Figure 37. Unsteady pressure distribution for case 13 for MBB-A3 airfoil. $M = 0.765$; $\alpha_m = 1.5°$; $h_o/c = 0.01$; $k = 0.9$.
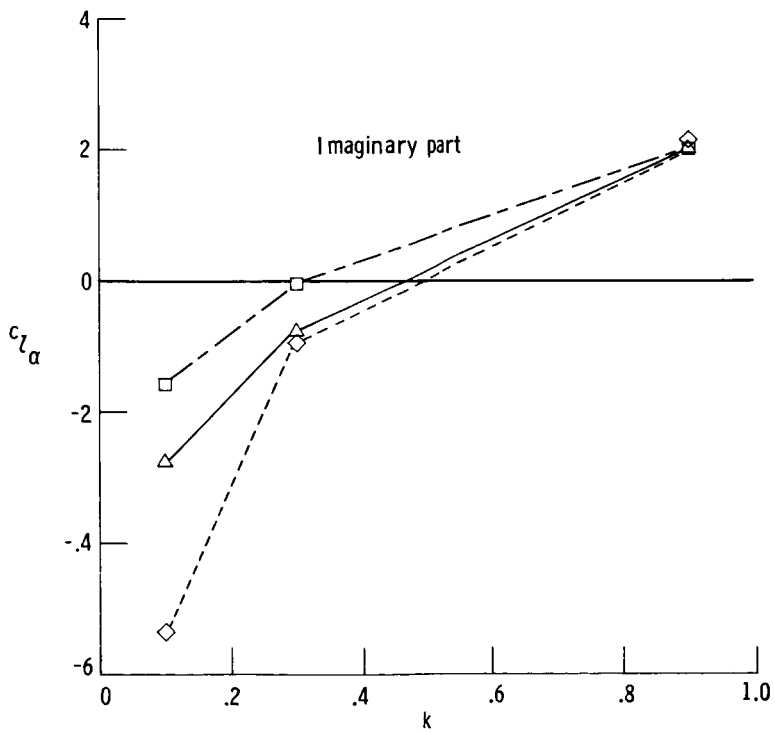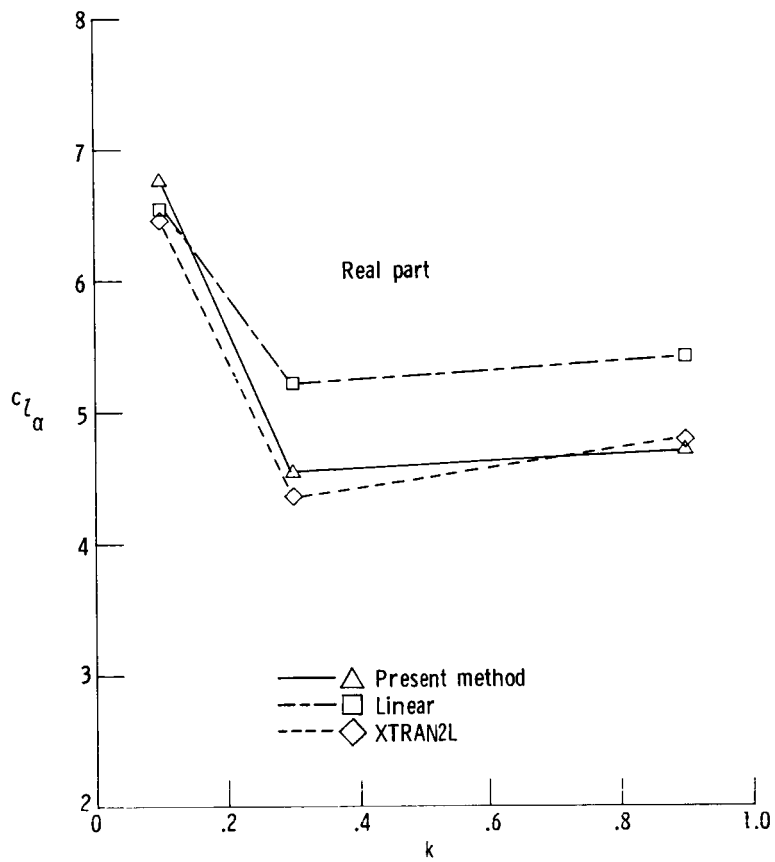
(a) Lift due to pitch oscillation.

Figure 38. Unsteady forces for MBB-A3 airfoil.
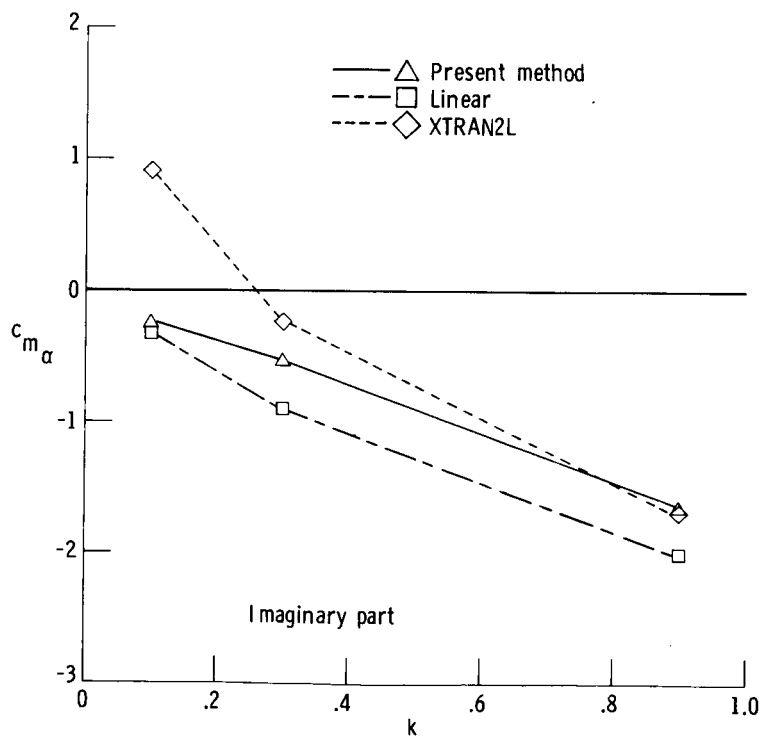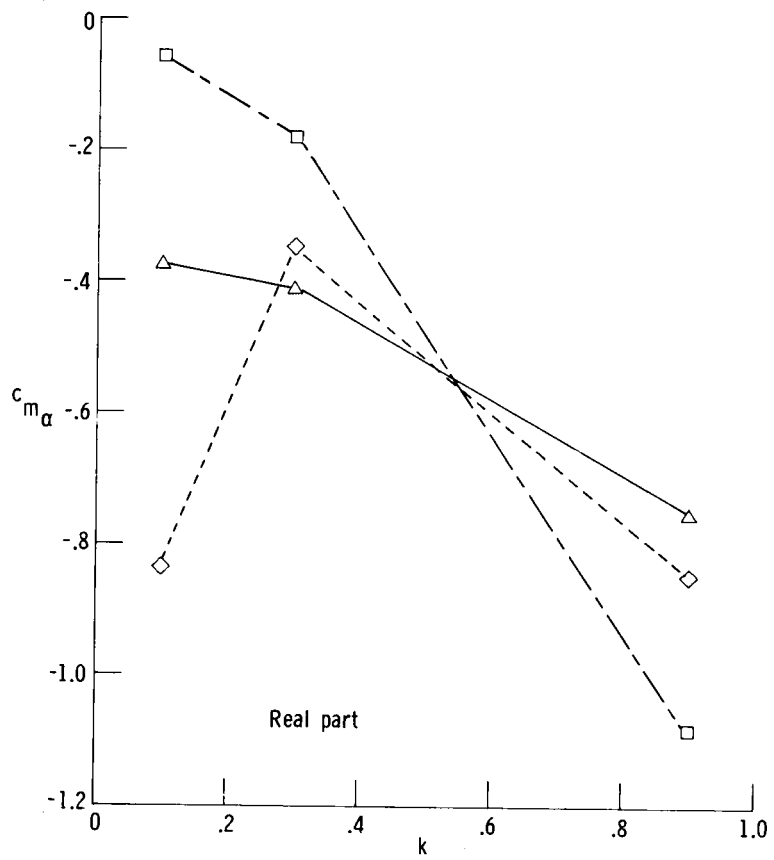
(b) Pitching moment due to pitch oscillation.

Figure 38. Continued.
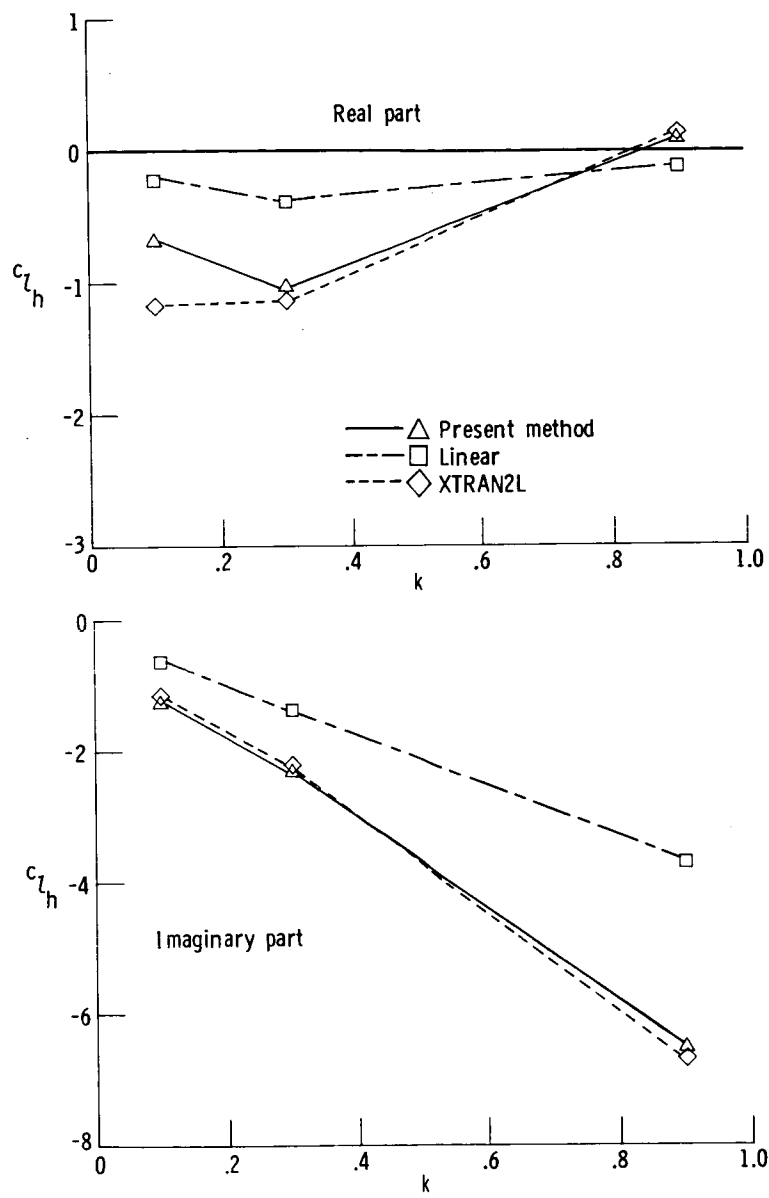
(c) Lift due to plunge oscillation.

Figure 38. Continued.
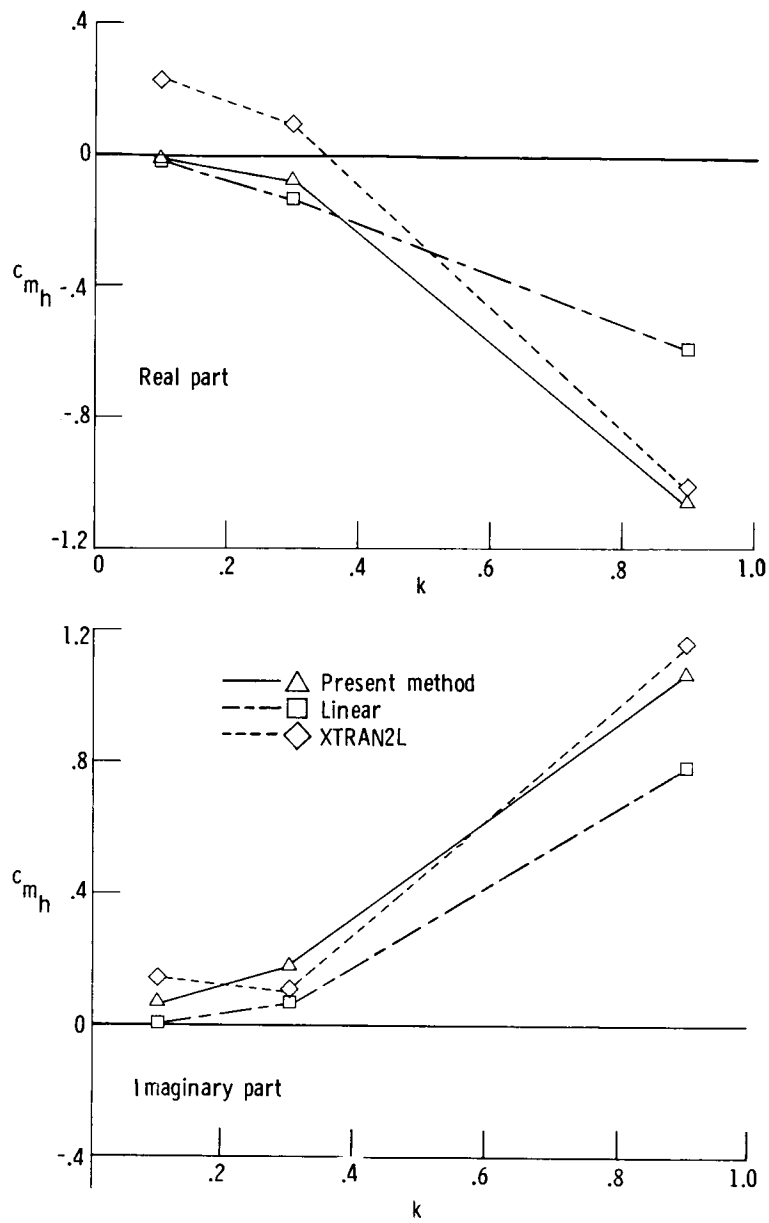
(d) Pitching moment due to plunge oscillation.

Figure 38. Concluded.

Figure 39. Steady pressure distribution for cases 1, 2, 3, and 5 for NACA 0012 airfoil.

(a) Mean.

(b) Lifting.

(c) Upper surface.

(d) Lower surface.

Figure 40. Unsteady pressure distribution for case 1 for NACA 0012 airfoil. $M = 0.601; \alpha_m = 2.89°;$ $\alpha_o = 2.41°; k = 0.081; N_{Re} = 4.8 \times 10^6$.
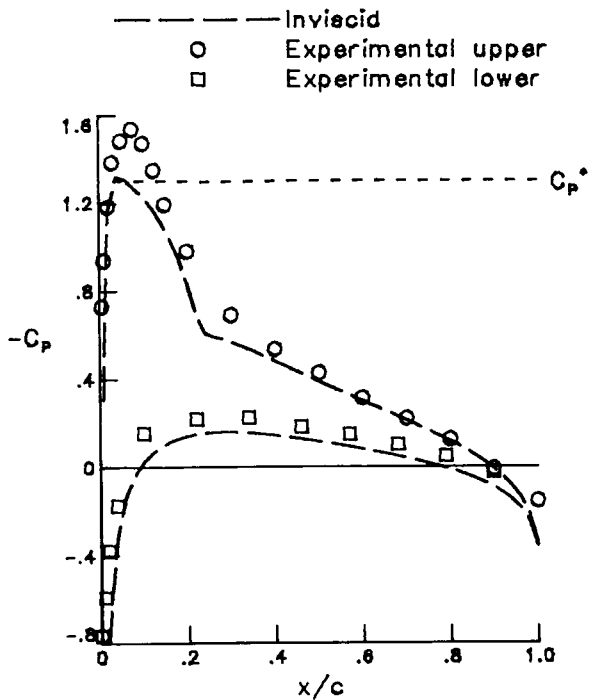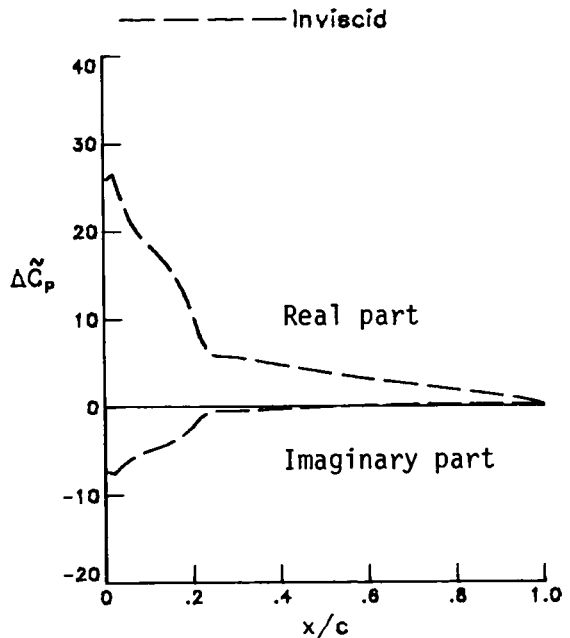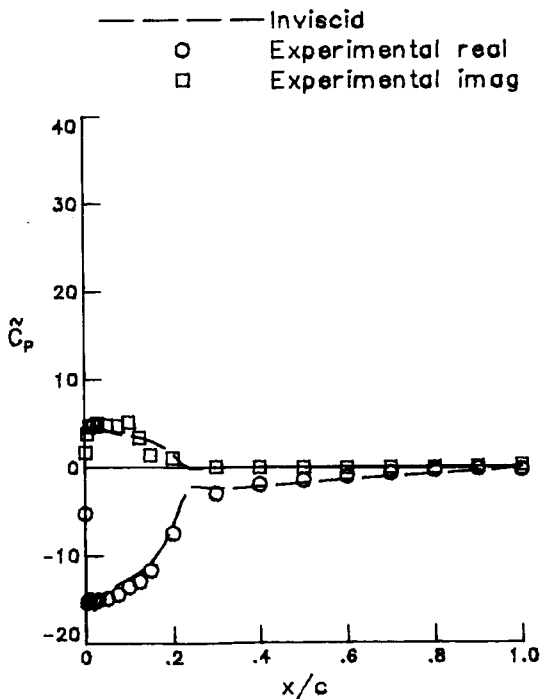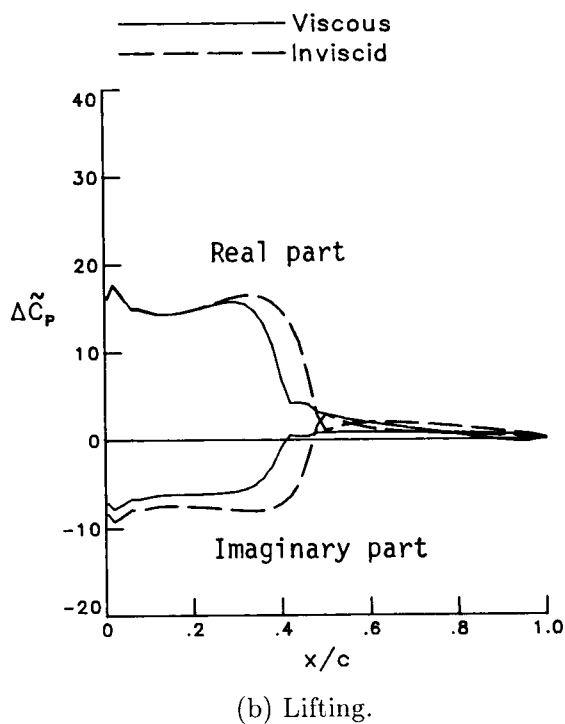
Figure 41. Unsteady pressure distribution for case 2 for NACA 0012 airfoil. $M = 0.599$; $\alpha_m = 3.16°$; $\alpha_o = 4.59°$; $k = 0.081$; $N_{Re} = 4.8 \times 10^6$.
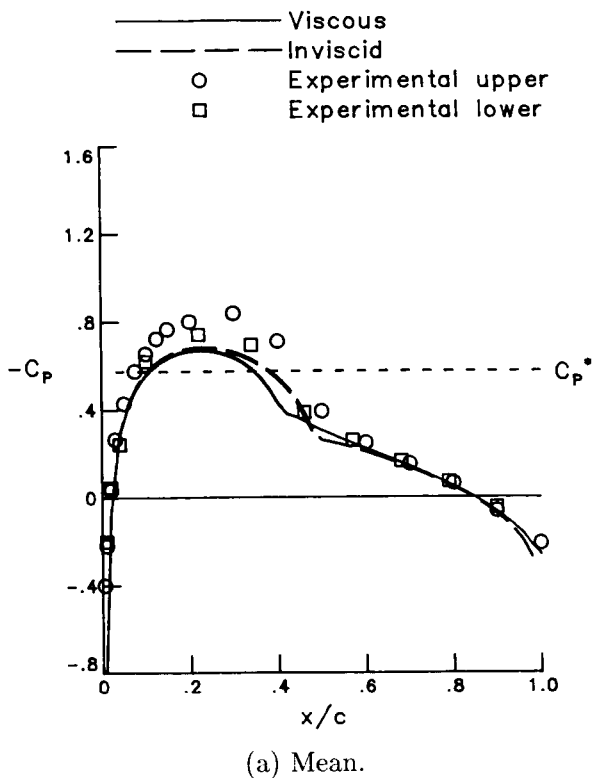
(a) Mean.

(b) Lifting.
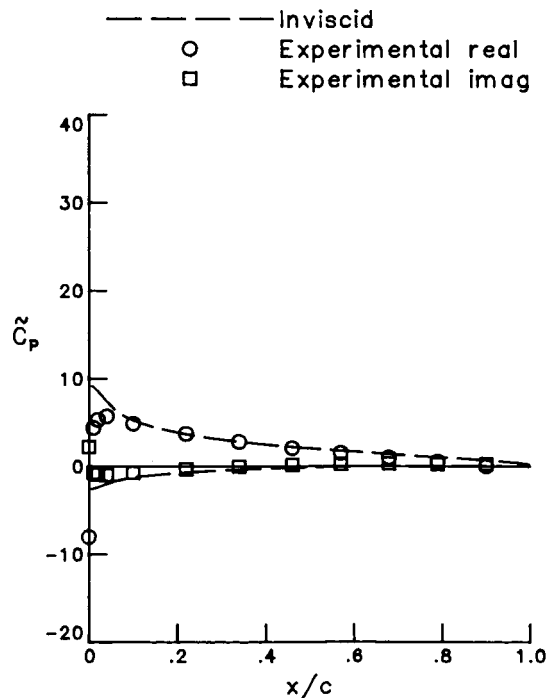
(c) Upper surface.

(d) Lower surface.

Figure 42. Unsteady pressure distribution for case 3 for NACA 0012 airfoil. $M = 0.599$; $\alpha_m = 4.86°$; $\alpha_o = 2.44°$; $k = 0.081$; $N_{\mathrm{Re}} = 4.8 \times 10^6$.

(a) Mean.

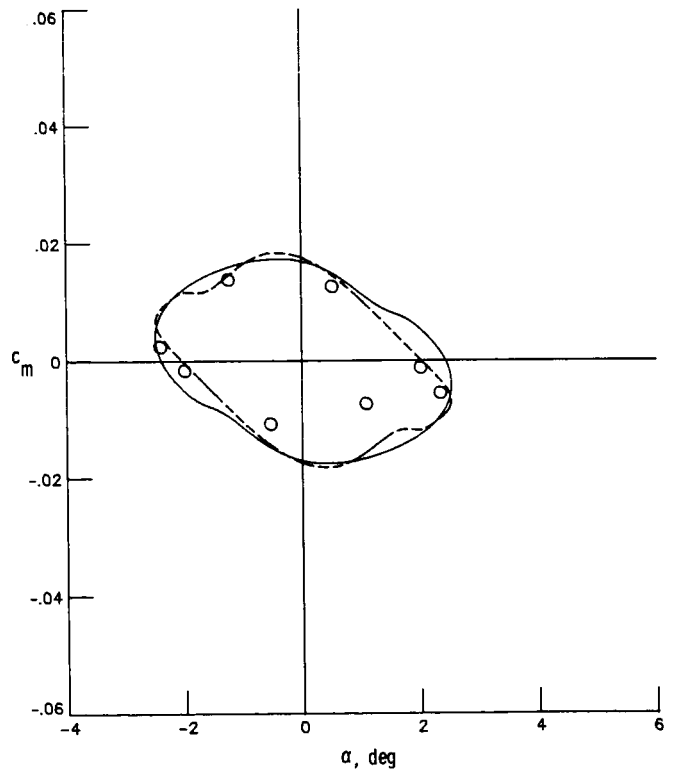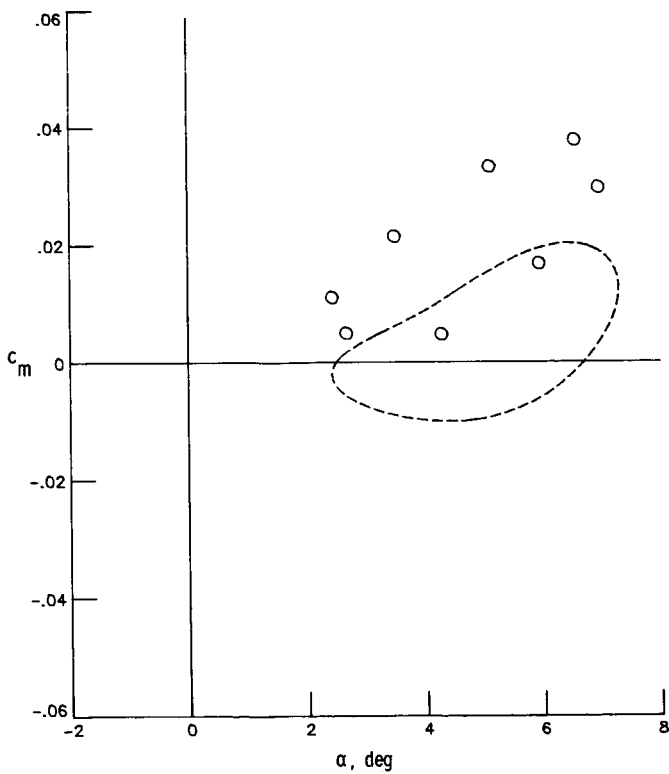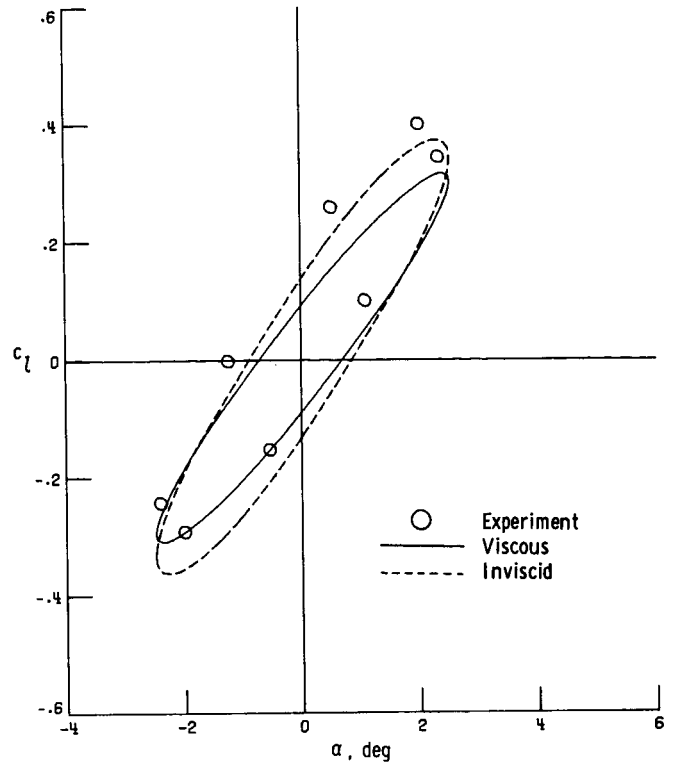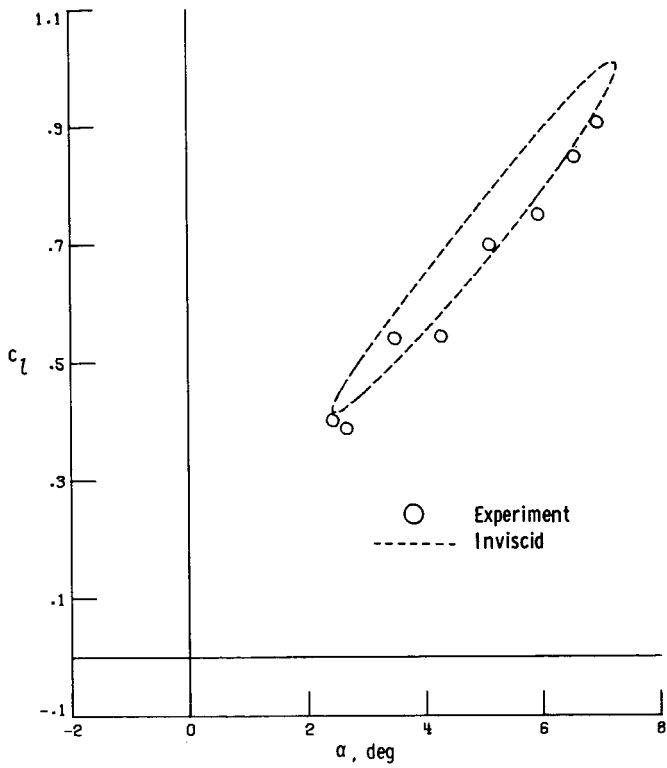(b) Lifting.

(c) Upper surface.

(d) Lower surface.
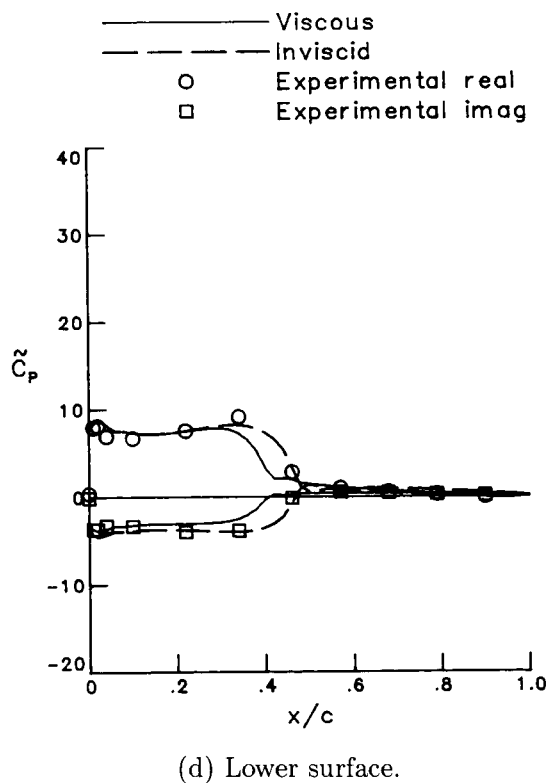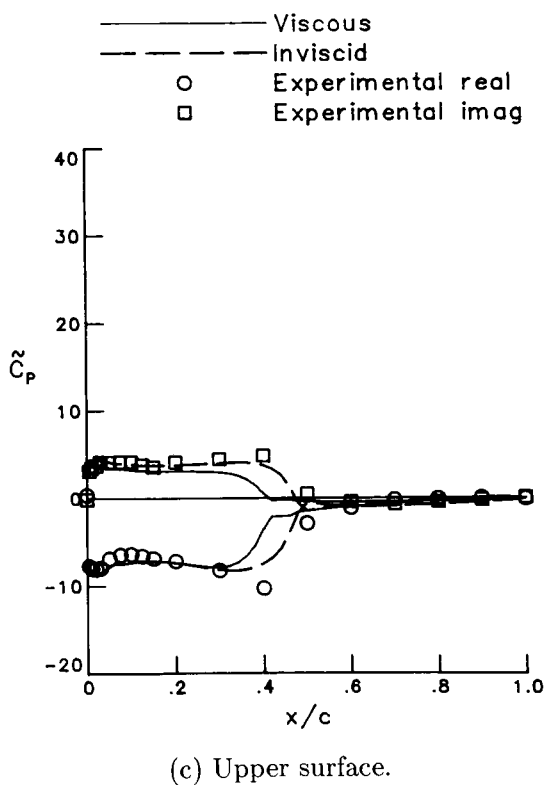
Figure 43. Unsteady pressure distribution for case 5 for NACA 0012 airfoil. $M = 0.755$; $\alpha_m = 0.02°$; $\alpha_o = 2.51°$; $k = 0.081$; $N_{\text{Re}} = 5.5 \times 10^6$.
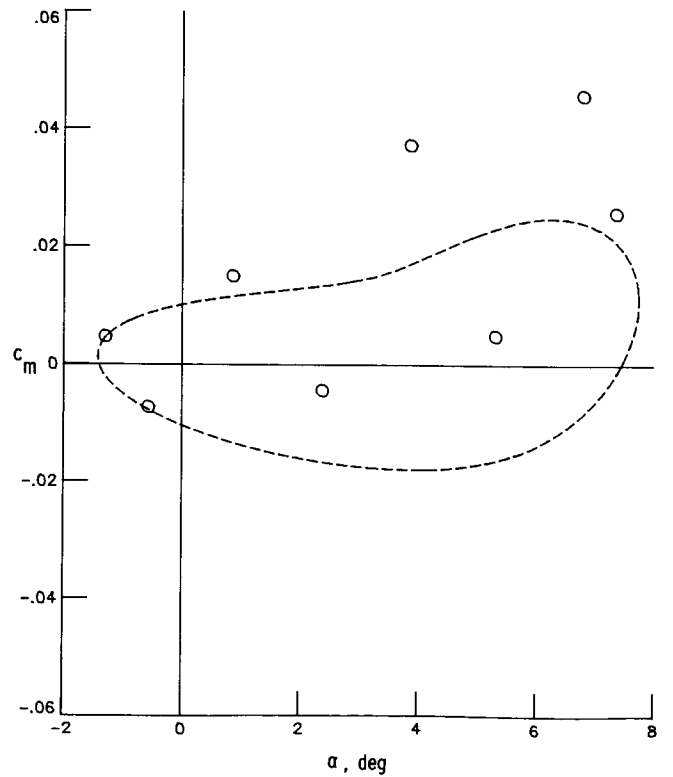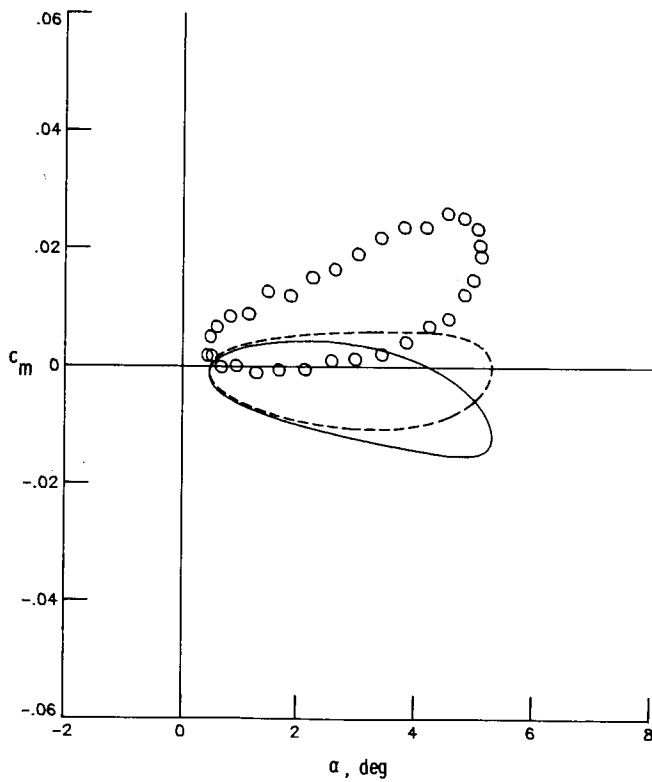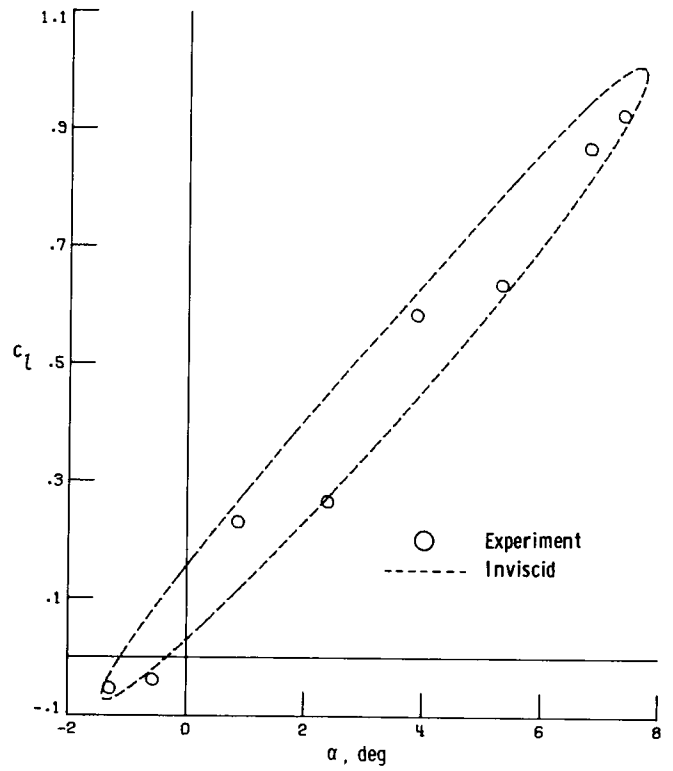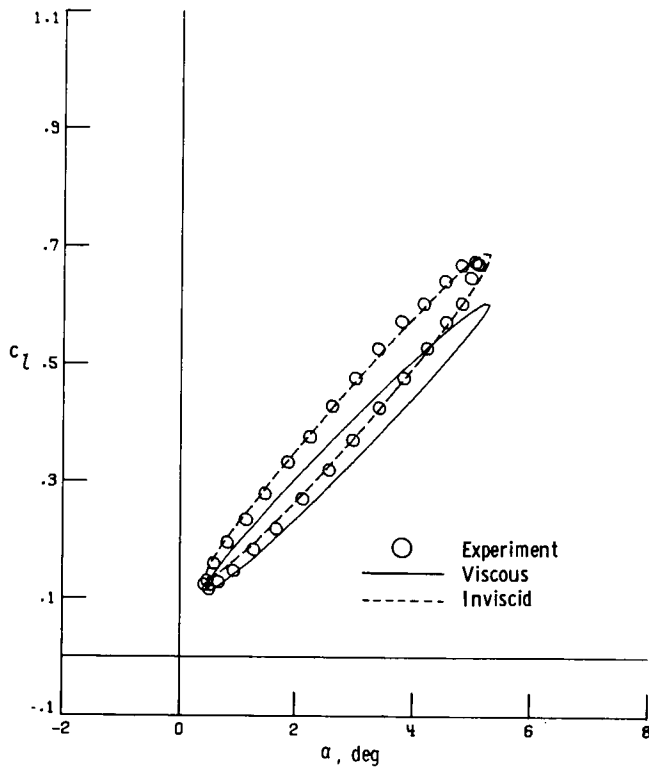
(a) Case 1. $M = 0.601$; $\alpha_m = 2.89°$; $\alpha_o = 2.41°$; $N_{Re} = 4.8 \times 10^6$.

(b) Case 2. $M = 0.599$; $\alpha_m = 3.16°$; $\alpha_o = 4.59°$; $N_{Re} = 4.8 \times 10^6$.

Figure 44. Comparison of unsteady forces versus angle of attack for cases 1, 2, 3, and 5 for the NACA 0012 airfoil at $k = 0.081$.

(c) Case 3. $M = 0.599$; $\alpha_m = 4.86°$; $\alpha_o = 2.44°$; $N_{Re} = 4.8 \times 10^6$.

(d) Case 5. $M = 0.755$; $\alpha_m = 0.02°$; $\alpha_o = 2.51°$; $N_{Re} = 5.5 \times 10^6$.
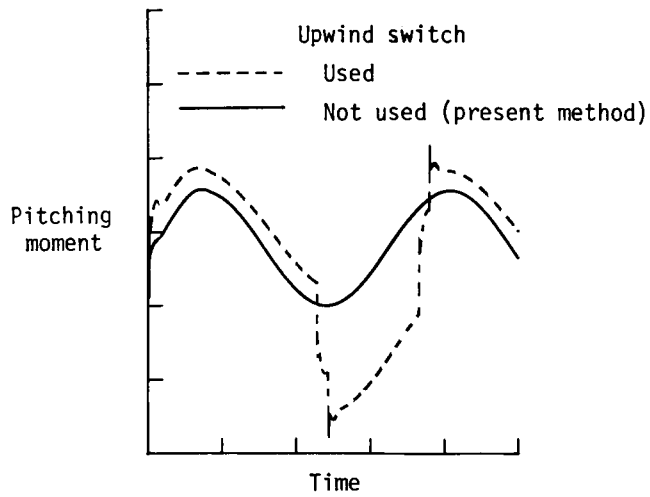
Figure 44. Concluded.

Figure 45. Pitching-moment time histories showing effect of upwind switch in boundary-layer calculation. NACA 64010A airfoil; $M = 0.796; \alpha_m = 0°$.
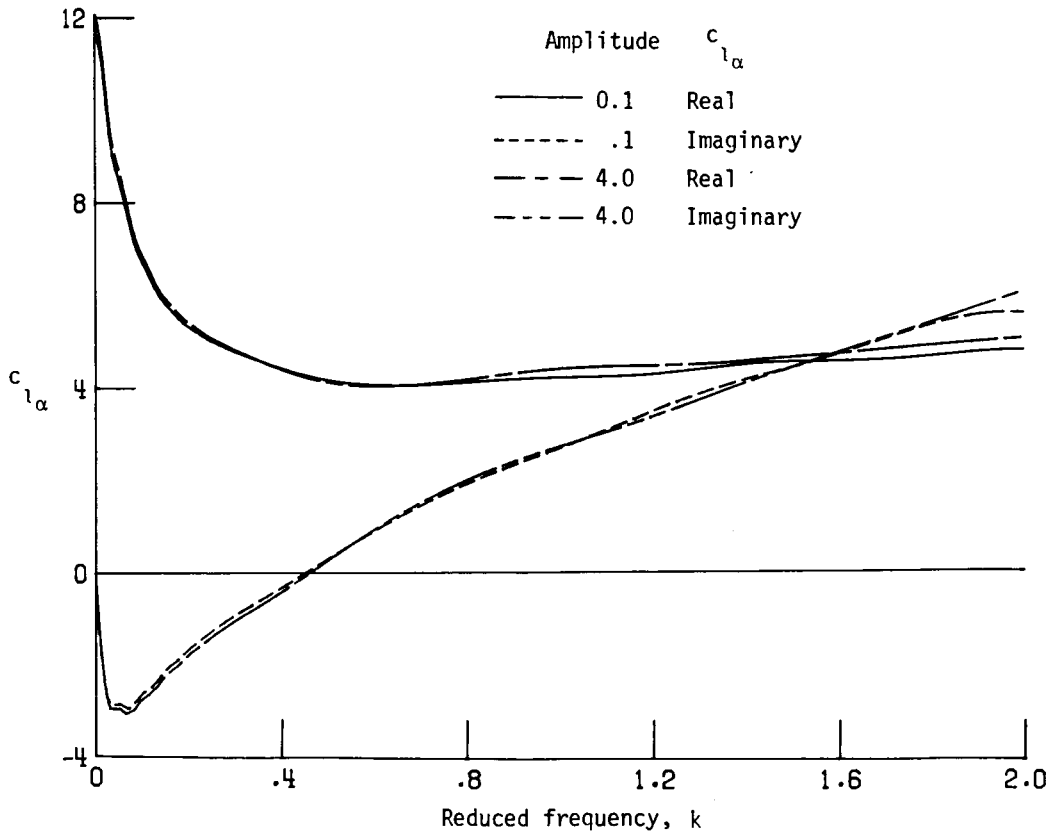

Figure 46. Effect of pulse amplitude on lift coefficient for NACA 64A010A airfoil. $M = 0.796; \alpha_m = -0.21°$.

1. Report No. NASA TP-2731	2. Government Accession No.	3. Recipient's Catalog No.
4. Title and Subtitle Calculation of Viscous Effects on Transonic Flow for Oscillating Airfoils and Comparisons With Experiment		5. Report Date September 1987
		6. Performing Organization Code
7. Author(s) James T. Howlett and Samuel R. Bland		8. Performing Organization Report No. L-16289
9. Performing Organization Name and Address NASA Langley Research Center Hampton, VA 23665-5225		10. Work Unit No. 505-63-21-01
		11. Contract or Grant No.
12. Sponsoring Agency Name and Address National Aeronautics and Space Administration Washington, DC 20546-0001		13. Type of Report and Period Covered Technical Paper
		14. Sponsoring Agency Code

15. Supplementary Notes

16. Abstract

A method is described for calculating unsteady transonic flow with viscous interaction by coupling a steady, integral boundary-layer code with an unsteady, transonic, inviscid small-disturbance computer code in a quasi-steady fashion. Explicit coupling of the equations together with viscous-inviscid iterations at each time step yield converged solutions with computer times about double those required to obtain inviscid solutions. The accuracy and range of applicability of the method are investigated by applying it to four AGARD standard airfoils. The first-harmonic components of both the unsteady pressure distributions and the lift and moment coefficients have been calculated. Comparisons with inviscid calculations and experimental data are presented. The results demonstrate that accurate solutions for transonic flows with viscous effects can be obtained for flows involving moderate-strength shock waves.

17. Key Words (Suggested by Authors(s)) Viscous-inviscid interaction Transonic unsteady aerodynamics Boundary layer AGARD configurations	18. Distribution Statement Unclassified—Unlimited Subject Category 02	
19. Security Classif.(of this report) Unclassified	20. Security Classif.(of this page) Unclassified	21. No. of Pages 75 22. Price A04